Astrophysikalisches Institut Potsdam
Star and Planet Formation

Properties of Turbulent Star-Forming Clusters: Models versus Observations

Dissertation
zur Erlangung des akademischen Grades
“doctor rerum naturalium” (Dr. rer. nat.)
in der Wissenschaftsdisziplin Astrophysik

eingereicht an der
Mathematisch-Naturwissenschaftlichen Fakultät
der Universität Potsdam

von

Stefan Schmeja

Potsdam, Januar 2006

La materia siguió dispersándose, dispersándose,
cada vez más fría y menos densa,
y un poco después – unos pocos centennares de miles de años –
se había enfriado lo suficiente para que electrones
unidos a núcleos engendraran átomos de hidrógeno y helio,
y este gas por la gravitación se fue juntando, juntando más,
y después apretándose más en forma de galaxias y estrellas
del presente universo.
...Las estrellas son mujeres
que por la noche encienden fuegos helados...

– Ernesto Cardenal, Cántico Cósmico, Cantiga 1

Abstract

Stars are born in turbulent molecular clouds that fragment and collapse under the influence of their own gravity, forming a cluster of hundred or more stars. The star formation process is controlled by the interplay between supersonic turbulence and gravity. In this work, the properties of stellar clusters created by numerical simulations of gravoturbulent fragmentation are compared to those from observations. This includes the analysis of properties of individual protostars as well as statistical properties of the entire cluster.

It is demonstrated that protostellar mass accretion is a highly dynamical and time-variant process. The peak accretion rate is reached shortly after the formation of the protostellar core. It is about one order of magnitude higher than the constant accretion rate predicted by the collapse of a classical singular isothermal sphere, in agreement with the observations.

For a more reasonable comparison, the model accretion rates are converted to the observables $T_{\rm bol}$, $L_{\rm bol}$, and $M_{\rm env}$. The accretion rates from the simulations are used as input for an evolutionary scheme. The resulting distribution in the $T_{\rm bol}$-$L_{\rm bol}$-$M_{\rm env}$ parameter space is then compared to observational data by means of a 3D Kolmogorov-Smirnov test. The highest probability found that the distributions of model tracks and observational data points are drawn from the same population is 70%.

The ratios of objects belonging to different evolutionary classes in observed star-forming clusters are compared to the temporal evolution of the gravoturbulent models in order to estimate the evolutionary stage of a cluster. While it is difficult to estimate absolute ages, the realtive numbers of young stars reveal the evolutionary status of a cluster with respect to other clusters. The sequence shows Serpens as the youngest and IC 348 as the most evolved of the investigated clusters.

Finally the structures of young star clusters are investigated by applying different statistical methods like the normalised mean correlation length and the minimum spanning tree technique and by a newly defined measure for the cluster elongation. The clustering parameters of the model clusters correspond in many cases well to those from observed ones. The temporal evolution of the clustering parameters shows that the star cluster builds up from several subclusters and evolves to a more centrally concentrated cluster, while the cluster expands slower than new stars are formed.

Zusammenfassung

Sterne entstehen im Inneren von turbulenten Molekülwolken, die unter dem Einfluss ihrer eigenen Gravitation fragmentieren und kollabieren. So entsteht ein Sternhaufen aus hundert oder mehr Objekten. Der Sternentstehungsprozess wird durch das Wechselspiel von Überschallturbulenz und Gravitation reguliert. In dieser Arbeit werden verschiedene Eigenschaften solcher Sternhaufen, die mit Hilfe von numerischen Simulationen modelliert wurden, untersucht und mit Beobachtungsdaten verglichen. Dabei handelt es sich sowohl um Eigenschaften einzelner Protosterne, als auch um statistische Parameter des Sternhaufens als Ganzes.

Es wird gezeigt, dass die Massenakkretion von Protosternen ein höchst dynamischer und zeitabhängiger Prozess ist. Die maximale Akkretionsrate wird kurz nach der Bildung des Protosterns erreicht, bevor sie annähernd exponentiell abfällt. Sie ist, in Übereinstimmung mit Beobachtungen, etwa um eine Größenordnung höher als die konstante Rate in den klassischen Modellen.

Um die Akkretionsraten der Modelle zuverlässiger vergleichen zu können, werden sie mit Hilfe eines Evolutionsschemas in besser beobachtbare Parameter wie bolometrische Temperatur und Leuchtkraft sowie Hüllenmasse umgewandelt. Die dreidimensionale Verteilung der Parameter wird anschließend mittels eines Kolmogorov-Smirnov-Tests mit Beobachtungsdaten verglichen.

Die relative Anzahl junger Sterne in verschiedenen Entwicklungsstadien wird mit der zeitlichen Entwicklung der Modelle verglichen, um so den Entwicklungsstand des Sternhaufens abschätzen zu können. Während eine genaue Altersbestimmung schwierig ist, kann der Entwicklungsstand eines Haufens relativ zu anderen gut ermittelt werden. Von den untersuchten Objekten stellt sich Serpens als der jüngste und IC 348 als der am weitesten entwickelte Sternhaufen heraus.

Zuletzt werden die Strukturen von jungen Sternhaufen an Hand verschiedener statistischer Methoden und eines neuen Maßes für die Elongation eines Haufens untersucht. Auch hier zeigen die Parameter der Modelle eine gute Übereinstimmung mit solchen von beobachteten Objekten, insbesondere, wenn beide eine ähnliche Elongation aufweisen. Die zeitliche Entwicklung der Parameter zeigt, dass sich ein Sternhaufen aus mehreren kleineren Gruppen bildet, die zusammenwachsen und einen zum Zentrum hin konzentrierten Haufen bilden. Dabei werden neue Sterne schneller gebildet als sich der Sternhaufen ausdehnt.

Contents

Chapter 1

Introduction

'The Answer?' said Deep Thought. 'The Answer to what?'
'Life!' urged Fook.
'The Universe!' said Lunkwill.
'Everything!' they said in chorus.
Deep Thought paused for a moment's reflection.
'Tricky,' he said finally.

– Douglas Adams, The Hitchhiker's Guide to the Galaxy

Stars do not exist forever. Stars are part of a cosmic cycle of matter, they are born, live for a while (between about 2×10^6 and 4×10^{10} years, depending on their mass) by burning hydrogen to helium, and they die, and in doing so they may give rise to the birth of a new generation of stars. Thus, star formation is not an event that took place once in a distant past, but it is observed today in many places throughout our Milky Way, as well as in other galaxies.

Early theories of star formation were obviously focussed on the origin of a single stellar system – our solar system. In the 18th century, Immanuel Kant and Pierre Simon Laplace developed nebular hypotheses, in which a rotating cloud of gas and dust cools and contracts under its own gravity. The matter flattens into a revolving disc, eventually leading to the formation of the Sun and the planets. At the beginning of the 20th century Sir James Jeans showed that there is a critical mass of the gas above which gravity supersedes the thermal pressure, resulting in the collapse of the cloud. This critical value is called the Jeans mass. The conclusion that stars are powered most of their lives by thermonuclear reactions transforming hydrogen into helium, and new observational techniques, in particular in the radio and infrared wavelength ranges, led to today's perception of star formation.

Stars form by the gravitational collapse of dense cores of interstellar gas and dust. All known star formation takes place in the interior of molecular clouds, cold and dense regions of interstellar matter, and almost all stars seem to form in clusters of a few dozens to thousands of objects.

The process of star formation itself cannot be observed directly, on the one hand due to the long timescale involved, and on the other hand, because the interior of

molecular clouds is almost opaque, at least in the visible light. Therefore, different theories of how stars form have been developed. They have to be able to explain the observed properties. With the advent of computers, it became possible to test the theories with numerical simulations. The observed properties of molecular clouds are used as input, and the outcome is compared to the observations of young stars, to draw a simplified picture. Early simulations dealt with the formation of a single, isolated star, while nowadays it is possible to simulate the collapse of a molecular cloud region forming a cluster of several dozens to hundreds of stars. The general picture of stars forming by the gravitational collapse of overdense molecular cloud cores is proven correct by simulations, however, many details of the star formation process are still unclear or subject to strong debate.

Many things can be learnt from simulations of star cluster formation. They can describe global (statistical) properties of stellar clusters like the initial mass function, the star formation timescale, the star formation efficiency, or the cluster structure, as well as local properties (i.e. of individual objects), like the accretion history, the angular momentum evolution, evolutionary tracks or spectral energy distributions of individual young stars. While it is obvious that only simulations of the formation of a stellar cluster can describe the global properties, it has to be kept in mind that individual properties are influenced by the cluster environment as well, e.g. by interactions between protostars. Therefore, differences to models of isolated star formation are expected.

The aim of this thesis is to investigate different properties of star-forming clusters obtained from numerical simulations of gravoturbulent fragmentation and to confront them with observational data. Basically this requires three steps: (1) a careful analysis of the results of the simulations, (2) the selection, analysis, and, if necessary, weighting of observational data, and (3) the development and application of adequate methods to compare the selected properties with each other. In particular, since we are interested not only in a qualitative comparison, but in a quantification of the agreement, sophisticated statistical methods are required. Finally this should permit the decision whether the assumptions of the considered models and the underlying paradigm of gravoturbulent fragmentation are a valid approach to describe stellar birth or not.

This thesis is structured as follows: In Chapter 2 our current knowledge of the star formation process is outlined. It discusses the observed properties of molecular clouds – the birth places of stars – and of the young stars as well as the relevant theories of star formation. Chapter 3 explains the basic concepts of numerical star formation simulations in general and describes in detail the simulations of gravoturbulent fragmentation used for this work. Chapter 4 gives an overview of observational methods relevant to star formation studies. In the subsequent Chapters the results are presented. While Chapters 5 and 6 deal with the properties of individual objects in a cluster, Chapters 7 and 8 consider a cluster as a whole. In Chapter 5 the mass accretion rates from the simulations are analysed and compared to obser-

vations. This analysis is extended in Chapter 6 by converting the mass accretion rates into easier observable parameters, which are then compared to observational data. In Chapter 7 the number ratios of young stars in different evolutionary classes are determined in observed star-forming regions and in the models and compared to each other, in order to constrain the models and to determine the evolutionary status of each observed cluster. Chapter 8 contains an analysis of the structures of young clusters using different statistical methods. Again, we investigate observed clusters as well as those from simulations and compare them. Finally, Chapter 9 summarises the results of this work and suggests some future prospects. Additional details of the methods used to analyse the cluster structures are given in the Appendix. The results discussed in Chapters 5, 6, 7, and 8 have been published or submitted as Schmeja & Klessen (2004), Froebrich et al. (2006), Schmeja et al. (2005), and Schmeja & Klessen (2006), respectively. However, they have been slightly revised and extended for this thesis. Smaller parts of this work have also been published in conference proceedings and abstracts, see the list of publications at the end of this thesis.

Chapter 2

Star Formation

Ellas [las estrellas] engendradas por la presión y el calor.
Como alegres bulevares iluminados
o poblaciones vistas de noche desde un avión.
El amor: que encendió las estrellas...

– Ernesto Cardenal, Cántico Cósmico, Cantiga 8

In this chapter, our present knowledge of star formation will be briefly outlined. Detailed descriptions can be found e.g. in Larson (2003), Smith (2004), or Stahler & Palla (2004).

2.1 Molecular Clouds

All known star formation takes place in molecular clouds (MCs). These are large condensations of cold interstellar gas, where most of the atoms (> 90%) are bound as molecules rather than existing as free atoms or ionized particles (see Blitz & Williams 1999, Williams et al. 2000, or Blitz 2001 for a review). With typical temperatures of $\sim 10\,\mathrm{K}$, molecular clouds are the coldest and densest form of the interstellar medium (ISM). While the mean particle density n averaged over an entire cloud is about $50\,\mathrm{cm}^{-3}$, it can be up to $10^6\,\mathrm{cm}^{-3}$ in regions of active star formation. Molecular clouds are observed throughout the entire Galaxy, as well as in most spiral galaxies, but they are preferably aligned with the spiral arms. However, they are not abundant in elliptical galaxies.

The overwhelming component (99.99% of the molecules) of MCs is molecular hydrogen gas (H_2), but more than 120 different molecules have been detected in interstellar MCs up to now.[1] Despite its abundance, H_2 cannot be detected directly since it is too cold to show emission or absorption. Usually it is detected by tracer molecules like CO (see § 4). The most abundant molecule after H_2 is carbon monoxide (CO), followed by water (H_2O), ammonia (NH_3), hydrogen

[1] An up-to-date list of detected interstellar molecules can be found e.g. at
`http://www.cv.nrao.edu/~awootten/allmols.html`

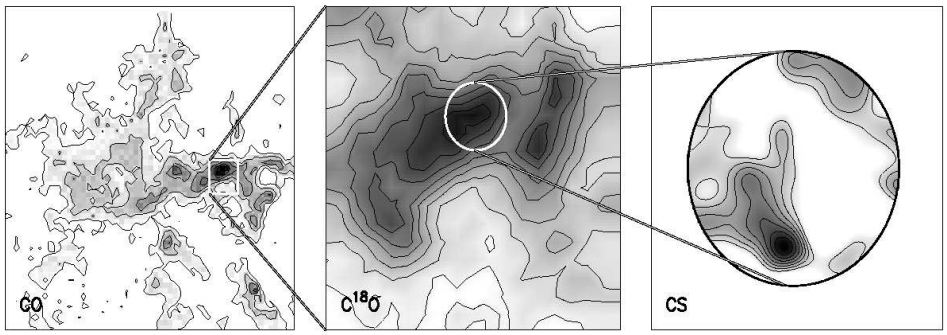

Figure 2.1: Hierarchical structure of a molecular cloud (the Rosette molecular cloud). The panels show, from left to right, the entire molecular cloud (H_2 gas traced by CO), a clump (mapped in $C^{18}O$) and a core (mapped in CS). Taken from Blitz & Williams (1999).

Table 2.1: Average properties of molecular clouds at different scales (adopted from Smith 2004 and Mac Low & Klessen 2004)

	GMCs	clumps	cores
Mass [$M_\odot$]	$10^4 - 10^6$	$10 - 10^3$	$1 - 10$
Size [pc]	$10 - 100$	$0.1 - 4$	~ 0.1
Temperature [K]	$10 - 100$	$7 - 15$	10
Density [cm^{-3}]	$100 - 300$	$10^3 - 10^4$	$10^4 - 10^5$
Lifetime [yrs]	3×10^6	10^6	6×10^5

sulfide (H_2S), hydrogen cyanide (HCN) and many other commonly known inorganic molecules. Molecular clouds even harbour organic molecules like formaldehyde (H_2CO), formic acid (HCOOH), or methanol (CH_3CO), and very complex molecules that do not exist at all on Earth, e.g. $HC_{11}N$. The ionisation level of MCs is low. In addition to the gaseous component, there is a small admixture of dust (~1% of the total mass).

Molecules can only form and survive inside dense clouds, where they are protected from ultraviolet radiation from massive stars, which otherwise would dissociate the molecules much faster than they could reform. Due to the low temperatures in molecular clouds, H_2 cannot form by direct collision and binding of two H atoms, since the excess energy cannot be radiated away. Hydrogen molecules rather form when H atoms attach themselves to the surface of dust grains. The atoms migrate on the surface of the dust grain and eventually bind together to form a molecule. The excess energy then heats the dust, which finally ejects the molecule. In the absence of dust, molecules may be formed by the collision of H atoms with available H^- in the reaction $H^- + H \rightarrow H_2 + e^-$.

Interstellar dust plays another crucial role: Molecules frequently collide with

dust grains, which are heated by the energy and emit radiation in the infrared (IR) part of the electromagnetic spectrum. Since molecular clouds are relatively transparent in the infrared, the energy is efficiently radiated away. Thus, the dust acts as a temperature regulator keeping the molecular clouds cold.

Molecular clouds have masses from a few solar masses ($M_\odot$) to about $10^6\,M_\odot$. Clouds with masses $M > 10^4\,M_\odot$ are called *giant molecular clouds* (GMCs), they have diameters of 50 pc or more. Molecular clouds are very inhomogeneous objects, they show large density gradients and contain dense clumps and filaments (see Fig. 2.1). The densest parts, which have typical densities of 10^5 to $10^6\,\mathrm{cm}^{-3}$ and sizes of less than a parsec, are called *cores*. They may eventually collapse and form stars. Table 2.1 lists typical parameters of molecular clouds at different scales. The structure of MCs may be described as fractal (e.g. Scalo 1990; Falgarone et al. 1991; Stutzki et al. 1998). In this picture, the clouds are scale-free and the hierarchy of clouds, clumps and cores reflects a self-similar structure. However, there are limits to a self-similar description of cloud structure. It is at least not universally appropriate, e.g. in Taurus self-similarity breaks down at a size scale of $\sim 0.2 - 0.3$ pc (Williams 1999). GMCs are self-gravitating, i.e. they are held together by the mass of the gas. However, their internal structure has to be maintained by some source of energy injection preventing them from immediate collapse under their own gravity. In the classical theories the clouds are stabilised by magnetic fields, today it is believed that supersonic turbulence, which is observed ubiquitously in molecular clouds, plays this role (see the discussion in § 2.4 to 2.6).

The process of how molecular clouds form is rather poorly understood and it is very likely that there is more than one mechanism (see e.g. Blitz & Williams 1999; Ballesteros-Paredes 2004). Earlier models of collisional agglomeration of smaller 'cloudlets' are in contradiction to observations and can probably be ruled out. Considering a turbulent ISM, clouds may form by the convergence of turbulent flows at large scales, which may be caused by some sort of instability, the passage of spiral density waves, or swept-up shells from supernova remnants.

In the classical picture the lifetime of a molecular cloud is in the order of 10^7 years (e.g. Palla & Stahler 2000; Tassis & Mouschovias 2004). However, there is now evidence that star formation takes place on relatively short timescales and that molecular clouds are rather transient objects that form and dissolve in the larger-scale turbulent flow of the Galactic disc (e.g. Bonnell et al. 2006). Most of the molecular clouds in the solar neighborhood contain young stars with typical ages between 1 and 3 Myr and a low age spread. This strongly suggests that molecular clouds generally form rapidly, produce stars rapidly, and disperse quickly within a timescale of only a few 10^6 years (Ballesteros-Paredes et al. 1999b; Elmegreen 2000; Hartmann et al. 2001; Hartmann 2003; Vázquez-Semadeni et al. 2005). Observations of self-similar structure in molecular clouds (e.g. Mac Low & Ossenkopf 2000; Ossenkopf & Mac Low 2002) indicate that interstellar turbulence is driven on scales substantially larger than the clouds themselves. These large-scale turbulent flows compress and cool the gas. At sufficiently high densities

atomic gas is then quickly converted into molecular form (Hollenbach et al. 1971). These same flows will continue to drive the turbulent motions observed within the newly formed cloud. Some combination of turbulent flow, free expansion at the sound speed of the cloud and dissociating radiation from internal star formation will then be responsible for the destruction of the cloud on a timescale of 5 to 10 Myr.

2.2 From Clouds to Stars

Stars form from gravitational collapse of gas and dust in dense molecular cloud cores. For this to happen, gravity has to overcome all dispersive or resistive forces. Small density fluctuations in an initially uniform medium are amplified by gravity in a process called gravitational instability. The perturbations become unstable against gravitational collapse once their wavelength λ exceeds a critical wavelength

$$\lambda_{\mathrm{J}} = \sqrt{\frac{\pi c_{\mathrm{s}}^2}{G\rho_0}}, \tag{2.1}$$

called the *Jeans length* after the work of Jeans (1902), where $c_{\mathrm{s}} = (kT/m)^{1/2}$ is the isothermal sound speed, G the gravitational constant, ρ_0 the initial mass density, and m the average particle mass. Under the assumption of a spherical perturbation, this corresponds to a critical mass *(Jeans mass)*

$$M_{\mathrm{J}} = \frac{4\pi}{3}\left(\frac{\lambda_{\mathrm{J}}}{2}\right)^3 \rho_0 = \frac{\pi}{6}\left(\frac{\pi}{G}\right)^{3/2} c_{\mathrm{s}}^3\, \rho_0^{-1/2}. \tag{2.2}$$

All perturbations with masses larger than M_{J} will collapse under their own weight. Provided the collapse remains isothermal, the Jeans mass falls as the density increases. Therefore, the cloud will fragment into smaller and smaller pieces as long as the process is isothermal. Once the released gravitational energy cannot escape the system anymore, the temperature rises, thus the Jeans mass increases, and the collapse is decelerated and eventually stopped. Since the critical density at which this occurs depends on the opacity (and the initial temperature) of the gas, it is called *opacity limit for fragmentation*. Although this classical picture of collapse and fragmentation has some inconsistencies, the Jeans criterion is still a central feature for the understanding of star formation.

The further evolution of the cloud fragments is as follows (see also Fig. 2.2): During the isothermal collapse, the released gravitational energy heats the molecules, which rapidly pass the energy on to dust grains via collisions. The dust grains re-radiate energy in the millimetre range, which can escape the core. Once the number density in the central part reaches about $10^{11}\,\mathrm{cm}^{-3}$ the gas becomes opaque to dust radiation, therefore the energy cannot be transported outwards anymore. Temperature, pressure, and opacity rise, the core changes from isothermal to adiabatic. The resulting higher thermal pressure counterbalances gravity, the

collapse is stopped and a temporary equilibrium is reached: The *first core* with a density of $10^{13} \lesssim n \lesssim 10^{14}\,\mathrm{cm}^{-3}$ and a temperature of $100 \lesssim T \lesssim 200\,\mathrm{K}$ is formed. Matter from the envelope keeps falling in onto the core making temperature and density increase further. At $T \approx 2000\,\mathrm{K}$ the hydrogen molecules dissociate. This is an endothermic process, i.e., it consumes energy. Therefore, the rise in temperature and pressure is slowed down, until gravity takes over again and the core goes into a *second collapse*. Once the molecules are exhausted, the energy consumption in the core is stopped. The thermal pressure decelerates and eventually stops the collapse, leading to a second, final protostellar core having a density of about $10^{23}\,\mathrm{cm}^{-3}$ and a temperature of about $10^4\,\mathrm{K}$. This core, which may only possess a few per cent of its final mass, is still surrounded by a massive envelope. Since the gas is rotating, it cannot fall directly onto the core because of angular momentum conservation. It forms an accretion disc around the core, in which the gas is transported inwards by viscous torques (Pringle 1981; Papaloizou & Lin 1995) before it is finally accreted by the protostar. If mass is accumulated by the disc faster than it is removed by viscous transport the disc will become too massive, generating spiral density waves. These gravitational torques support and increase the inward transport of disc material. If the density of the disc is high enough, it may become even more gravitationally unstable and fragment, possibly leading to the formation of brown dwarves or gas planets. A significant fraction of the infalling matter does not end up on the star at all, but is released again by bipolar outflows or jets, a phenomenon observed in many accreting protostars. Jets associated with young stellar objects (YSOs) can reach velocities up to $400\,\mathrm{km\,s}^{-1}$ (e.g. Königl & Pudritz 2000). The rapid collapse phase is followed by a much slower quasi-static contraction of the protostar. Temperature and pressure keep rising, until the hydrogen in the core ignites at a temperature of about $10^7\,\mathrm{K}$ and fusion sets in. This results in a new equilibrium and the star has finally reached the main sequence after about 10^7 years.

2.3 Embedded Clusters

Almost all stars form in clusters (see Elmegreen et al. 2000 or Lada & Lada 2003 for a review). The theory of star formation therefore has to describe the formation of a stellar cluster rather than that of isolated stars. Lada & Lada (2003) define a cluster as a group of 35 or more physically related stars with mass densities $\rho_* > 1.0\,\mathrm{M}_\odot\,\mathrm{pc}^{-3}$. Stellar clusters are born embedded within dense giant molecular clouds, making them visible only at infrared wavelengths. The extinction due to interstellar dust can be as high as $A_V \sim 100\,\mathrm{mag}$. The degree of embeddedness corresponds to the evolutionary stage of a cluster: while the least evolved clusters (e.g. Serpens, ρ Ophiuchi) are found in heavily obscured, massive dense molecular cloud cores, the most evolved clusters (e.g. Trapezium, IC 348) are located within HII regions or at the edges of molecular clouds. Embedded clusters are physically associated with the most massive and densest molecular cloud cores with masses

Table 2.2: Basic parameters of some embedded clusters

Name	RA (J2000)	Dec. (J2000)	n_*	m_* [$M_\odot$]	dist. [pc]	dia. [pc]	SFE [%]	Ref.[a]
ρ Ophiuchi	16:25:35	−23:26.8	291[b]	102	140	4		1
L1688[c]	16:28:06	−24:32.5	262[b]	92	140	0.8	6-14	1
Serpens	18:29:49	+01:14.8	80	25-40	260	2.4	9	2,3
Taurus	04:41:00	+25:52.0	197	140	140	45	2-25	4
Cha I	11:06:48	−77:18.0	182	120	150	7	13	5,6
IC 348	03:44:34	+32:09.8	288	160	315	2		7,8,9
NGC 7129	21:42:56	+66:06.2	122	76	1000	1.2		9,10
IC 1396A	21:36:00	+57:24.0	56	8-30	750	2.5	4-15	11

[a]References: (1) Bontemps et al. (2001); (2) Kaas et al. (2004); (3) Olmi & Testi (2002); (4) Hartmann (2002); (5) Mizuno et al. (1999); (6) Haikala et al. (2005); (7) Luhman et al. (2003); (8) Muench et al. (2003); (9) Lada & Lada (2003); (10) Gutermuth et al. (2005); (11) Reach et al. (2004)

[b]estimated values. The ratio of identified YSOs is about 75%.

[c]main cloud of the ρ Ophiuchi complex

up to 1000 $M_\odot$, densities up to $10^4\,M_\odot\,pc^{-3}$ and diameters of 0.5 to 1 pc. These gas densities lead to stellar mass densities of about 10^3 to $10^4\,M_\odot\,pc^{-3}$. However, not all massive dense MC cores are presently forming clusters. More than 90% of the stars that form in clusters form in large clusters with over 100 members and masses larger than 50 $M_\odot$. The embedded phase of a cluster lasts only 2 to 3 Myrs; clusters with ages > 5 Myrs are rarely associated with molecular gas. Most clusters will likely dissolve before reaching an age of 10 Myrs, only about 4 to 7% of embedded clusters may survive the emergence from the parental molecular cloud to become bound clusters like the Pleiades (Lada & Lada 2003).

Observations indicate a mass segregation in young clusters (e.g. Hillenbrand & Hartmann 1998), suggesting that the most massive stars are formed preferentially close to the cluster centre. Whether this is a primordial property of embedded clusters or caused by the subsequent dynamical evolution is still under debate.

While embedded clusters span a wide range in mass of about two orders in magnitude, they are all of roughly the same age (~ 2 Myr). This means that the star formation rate (SFR) varies significantly, maybe due to the effect of external triggering. The star formation efficiency (SFE), i.e., the ratio of the mass in stars to the total mass of the cloud, is an important parameter describing the evolution of a young cluster. While the global SFE for GMCs are only a few percent, it can reach values of about 30% in dense MC cores. The SFE increases with time, the maximum value by the time the cluster emerges from the molecular cloud is estimated to be around 30% (Lada & Lada 2003).

Embedded clusters contain a statistically significant sample of young stars that have been formed more or less at the same time from the same progenitor cloud and span a wide range of masses. This makes them ideal laboratories to study various

aspects of the star formation process, like the initial mass function (IMF; see § 2.8) or stellar dynamics due to complex interactions.

Table 2.2 lists the basic parameters of the embedded clusters that will be discussed in detail in this work. Columns 1 to 3 contain the name and average position (right ascension and declination) of the clusters taken from the Simbad data base. Columns 4 to 9 give the number of YSOs, total mass of YSOs, distance, linear diameter, and star formation efficiency (SFE) of the cluster according to the references listed in the last column. If no information on the linear diameter of the cluster was found in the literature, it was computed from the angular diameter and the distance. Note that most of the parameters cannot be measured directly, but have to be inferred by indirect methods or estimated, therefore they may contain significant uncertainties. The numbers of YSOs are given for illustrative purposes, for a detailed discussion on that subject see § 7.1. An extensive catalogue of Galactic embedded clusters within ∼2 kpc of the Sun can be found in Lada & Lada (2003), another catalogue, focussing on the positions and dimensions of infrared (i.e. mostly embedded) clusters, was compiled by Bica et al. (2003).

2.4 The "Standard Theory" of Star Formation

Es gibt also keinen klar formulierbaren Unterschied zwischen Mythen und wissenschaftlichen Theorien.

– Paul Feyerabend, Wider den Methodenzwang

In the so-called "standard theory" of star formation (Shu 1977; Shu et al. 1987) stars are formed by the inside-out collapse of gas clumps, whose initial conditions are a singular isothermal sphere (SIS), i.e. a hydrostatic equilibrium density distribution

$$\rho(r) \sim \frac{c_s^2}{2\pi G r^2} \tag{2.3}$$

(for $0 < r < R_{\rm core}$), where $c_s = (kT/m)^{1/2}$ is the isothermal sound speed, G the gravitational constant, m the average particle mass, and $R_{\rm core}$ the outer radius of the core.

In this scenario, molecular cloud clumps are initially in quasistatic equilibrium and supported against gravitational collapse by magnetic pressure (Mestel & Spitzer 1956). Material diffuses slowly through the magnetic field towards the centre by ambipolar diffusion (ion-neutral drift), resulting in a steadily growing central core approximating a SIS. Once the critical density is exceeded, the SIS undergoes an inside-out collapse while the gas stays isothermal. This collapse is initiated by a spherical expansion wave which propagates outward at a speed of about c_s. The gas outside the expansion wave stays more or less stationary, while the gas inside the expansion wave approaches the central protostar almost in free fall. The protostar grows roughly linearly with time with a mass accretion rate that only depends

on the isothermal sound speed:

$$\dot{M} = 0.975\frac{c_s^3}{G} \tag{2.4}$$

(Shu 1977). Since the gas is expected to possess significant angular momentum, only a fraction of the infalling mass is accreted directly by the central protostar, while the remainder forms a circumstellar accretion disc. In the last stage, angular momentum is removed from the disc and most of the mass will eventually be accreted by the young star. The remainder of the disc may form a planetary system or is dispersed.

This theory, however, experiences several problems and is challenged by both observational and theoretical results (see e.g. Mac Low & Klessen 2004). Theoretical considerations show that SIS are very unlikely as initial conditions for collapse (Whitworth et al. 1996), and at the same time observations suggest that the central density profiles of cores are flatter than those expected for isothermal spheres (Bacmann et al. 2000). The SIS paradigm is only applicable to isolated stars, whereas it is now known that the majority of stars form in small aggregates or large clusters (Adams & Myers 2001; Lada & Lada 2003, see also § 2.3). Furthermore, there is both observational evidence (Crutcher 1999; André et al. 2000; Bourke et al. 2001) and theoretical reasoning (e.g. Nakano 1998) showing that most observed cloud cores do not have magnetic fields strong enough to support them against gravitational collapse. Similarly, the long lifetimes implied by the quasi-static phase of evolution in the model are difficult to reconcile, e.g. with observational statistics of cloud cores (Taylor et al. 1996; Lee & Myers 1999; Visser et al. 2002) and with chemical age considerations (van Dishoeck & Blake 1998; Langer et al. 2000). The "standard theory" predicts constant mass accretion rates, while both observations and numerical simulations lead to the conclusion that protostellar mass accretion is a highly dynamical and time-variant process (see the detailed discussion in § 5).

These inconsistencies have led to the suggestion that star formation is moderated by interstellar turbulence and its interplay with gravity rather than by magnetic fields. This approach will be outlined in the following two sections.

2.5 Turbulence

According to an apocryphal story, Werner Heisenberg was asked what he would ask God, given the opportunity. His reply was: "When I meet God, I am going to ask him two questions: Why relativity? And why turbulence? I really believe he will have an answer for the first."

– found on the web[2]

The internal velocity dispersions of molecular clouds are supersonic with Mach numbers (the ratio of the speed of the flow to the speed of sound: $\mathcal{M} = v/c_s$) of

[2] e.g. `http://en.wikipedia.org/wiki/Turbulence`

$\mathcal{M} \approx 10$ and larger (Larson 1981; Blitz 1993; Williams et al. 2000). The observed broadening of spectral lines is usually interpreted as the signature of interstellar turbulence. Turbulence means a nonlinear state of fluid motion that is characterised by random and chaotic motions at many scales. When present, turbulence usually dominates all other flow phenomena like mixing, heat transfer, or drag. Detailed descriptions of observations and theory of interstellar turbulence can be found in the reviews by Franco & Carramiñana (1999), Elmegreen & Scalo (2004), Scalo & Elmegreen (2004), and Mac Low & Klessen (2004).

The first theory to describe turbulence was developed by Kolmogorov (1941). In this picture, turbulence is incompressible and driven by energy injected on a large scale. The turbulent kinetic energy is then dissipated by interacting with smaller vortices and thus transferred to smaller and smaller scales (i.e. larger wave numbers k), until the energy has cascaded all the way down to the dissipation scale λ_{visc}, where viscous dissipation turns the kinetic energy into heat. This cascade leads to an energy spectrum

$$E(k) \propto k^{-5/3}, \tag{2.5}$$

where $k = 2\pi/\lambda$ is the wave number.

The motion of the interstellar gas, however, differs from this picture. The interstellar medium is highly compressible and supersonic, and the turbulent driving is not uniform, but caused by shock waves and other inhomogeneous processes. Supersonic flows in highly compressible gas lead to strong density fluctuations. In supersonic turbulence, shock waves also account for the dissipation of kinetic energy by transferring energy between widely separated scales, unlike the cascading nature of incompressible turbulence.

Under molecular cloud conditions, supersonic turbulence likely decays in less than one free-fall time (Stone et al. 1998; Mac Low et al. 1998; Mac Low 1999; Padoan & Nordlund 1999). Since it is observed ubiquitously in molecular clouds of all ages, it has to be driven on large scales. This driving is neither uniform nor homogeneous. Possible driving mechanisms of interstellar turbulence include magnetorotational instabilities (Dziourkevitch et al. 2004; Piontek & Ostriker 2004, 2005), gravitational instabilities (Wada et al. 2002), protostellar outflows (Mac Low 2000; Reipurth & Bally 2001; Quillen et al. 2005), and supernovae (e.g. Dib et al. 2006). There is an ongoing debate on which of those is the most important energy source. The most likely source of large-scale interstellar turbulence in the Milky Way is the combined energy and momentum input from supernovae explosions (Mac Low & Klessen 2004). They appear to overwhelm all other possibilities. In the outer reaches of the Galaxy and in low surface brightness galaxies, on the other hand, the situation is not so clear. In low-density regions of the interstellar medium, like the far outer Galaxy, the magnetorotational instability might play an important role (Piontek & Ostriker 2005).

2.6 Gravoturbulent Fragmentation

In contrast to the "standard theory" of star formation described in § 2.4, it is now believed that star formation in molecular clouds is controlled by the complex interplay between interstellar turbulence and self-gravity (Vázquez-Semadeni et al. 2000; Klessen 2003; Mac Low & Klessen 2004). The supersonic turbulence ubiquitously observed in Galactic molecular gas carries sufficient energy to counterbalance gravity on global scales. On small scales, however, it may actually provoke localised collapse: Interstellar turbulence generates strong density fluctuations with gravity taking over in the densest and most massive regions (e.g. Sasao 1973; Hunter & Fleck 1982; Elmegreen 1993; Padoan 1995; Ballesteros-Paredes et al. 1999a; Klessen et al. 2000; Klessen 2001b; Padoan & Nordlund 1999, 2002). We call this process *gravoturbulent fragmentation*. In a cloud core where gravitational attraction overwhelms all opposing forces from pressure gradients or magnetic fields, localised collapse will set in. The density increases until a protostellar object forms in the centre and grows in mass via accretion from the infalling envelope.

In this picture, turbulence plays a dual role: While it counterbalances gravity on global scales, preventing the cloud as a whole from collapsing, it can on the other hand produce density enhancements that lead to local collapse. This is only an apparent paradox: Supersonic turbulence causes a complex network of interacting shocks and converging flows, leading to regions of high density. The gas in these density enhancements may eventually become gravitationally unstable and collapse. The system becomes highly filamentary, with elongated structures caused either by shear motions or by compression at the intersection of shocked layers of gas. At some locations the density enhancement can be sufficiently strong for gravitational instability to set in. The stability criteria for filaments and sheets have been derived and discussed in the context of star formation, e.g. by Larson (1985), Lubow & Pringle (1993), and Clarke (1999). However, the random flows responsible for the local density enhancements may also disperse them again. Thus, for a local density enhancement to actually go into collapse and produce stars, the collapse has to be fast enough to 'decouple' from the flow, i.e. its duration must be shorter than the typical time interval between two successive shock passages. The shorter this interval, the less likely a contracting region is going to survive and eventually end up in the formation of stars.

Thus, the efficiency of protostellar core formation, the growth rates and final masses of the protostars and essentially all other properties of nascent star clusters then depend on the intricate interplay between gravity on the one hand and the turbulent velocity field in the cloud on the other. The star formation rate is regulated not just at the scale of individual star-forming cores through ambipolar diffusion balancing magnetostatic support, but rather at all scales (Elmegreen 2002), via the dynamical processes that determine whether regions of gas become unstable to prompt gravitational collapse. The presence of magnetic fields does not alter that picture significantly (Mac Low et al. 1998; Stone et al. 1998; Padoan & Nordlund

1999; Heitsch et al. 2001b). In particular, it cannot prevent the decay of interstellar turbulence.

Clusters of stars build up in molecular cloud regions where self-gravity overwhelms turbulence, either because such regions are compressed by a large-scale shock, or because interstellar turbulence is not replenished and decays on short timescales. Then, many gas clumps become gravitationally unstable and synchronously go into collapse. If the number density is high, contracting protostellar cores interact and may merge to produce new cores which now contain multiple protostars. Close encounters drastically alter the trajectories of the protostars, thus changing their mass accretion rates. This has important consequences for the final stellar mass spectrum (Bonnell et al. 1997; Klessen & Burkert 2000, 2001; Bonnell et al. 2001a,b; Klessen 2001b; Bate et al. 2002).

Inefficient, isolated star formation will occur in regions that are supported by turbulence carrying most of its energy on very small scales. This requires an unrealistically large number of driving sources and appears at odds with the measured velocity structure in molecular clouds which in almost all cases is dominated by large-scale modes (Mac Low & Ossenkopf 2000; Ossenkopf & Mac Low 2002).

Numerical simulations (e.g. Klessen et al. 2000; Klessen & Burkert 2000, 2001; Klessen 2001a,b; Heitsch et al. 2001a; Padoan & Nordlund 2002) have shown that gravoturbulent fragmentation can successfully explain the observational properties of star-forming clouds and young stars. It provides a consistent picture of the entire process of star formation. Some new aspects will be discussed in this work.

2.7 Classification of Young Stellar Objects

Young stellar objects are usually divided into four classes on basis of the properties of their spectral energy distribution (SED) in the infrared, indicating an evolutionary sequence. Classes 1, 2, and 3[3] have been introduced by Lada & Wilking (1984) and Lada (1987); later Class 0 has been added to describe an even younger evolutionary stage (André et al. 1993). The observational properties of the different classes are described in detail in André et al. (2000), Lada (2001), or Smith (2004). The basic properties are summarised in Table 2.3, the SEDs typical for each class are shown in Fig. 2.3. A characteristic feature is the slope of the infrared SED, or spectral index, determined in the wavelength range between 2 and 20 μm:

$$\alpha_{\rm IR} = \frac{d(\log \lambda S_\lambda)}{d(\log \lambda)} \tag{2.6}$$

where S_λ denotes the luminosity within each wavelength interval.

[3] originally, the classes have been denoted with Roman numbers: Class I, II, III, but it has been pointed out that the later introduced zero is unknown to the Roman system, so, to be consistent, Arabic numbers will be used for all the YSO classes from 0 to 3.

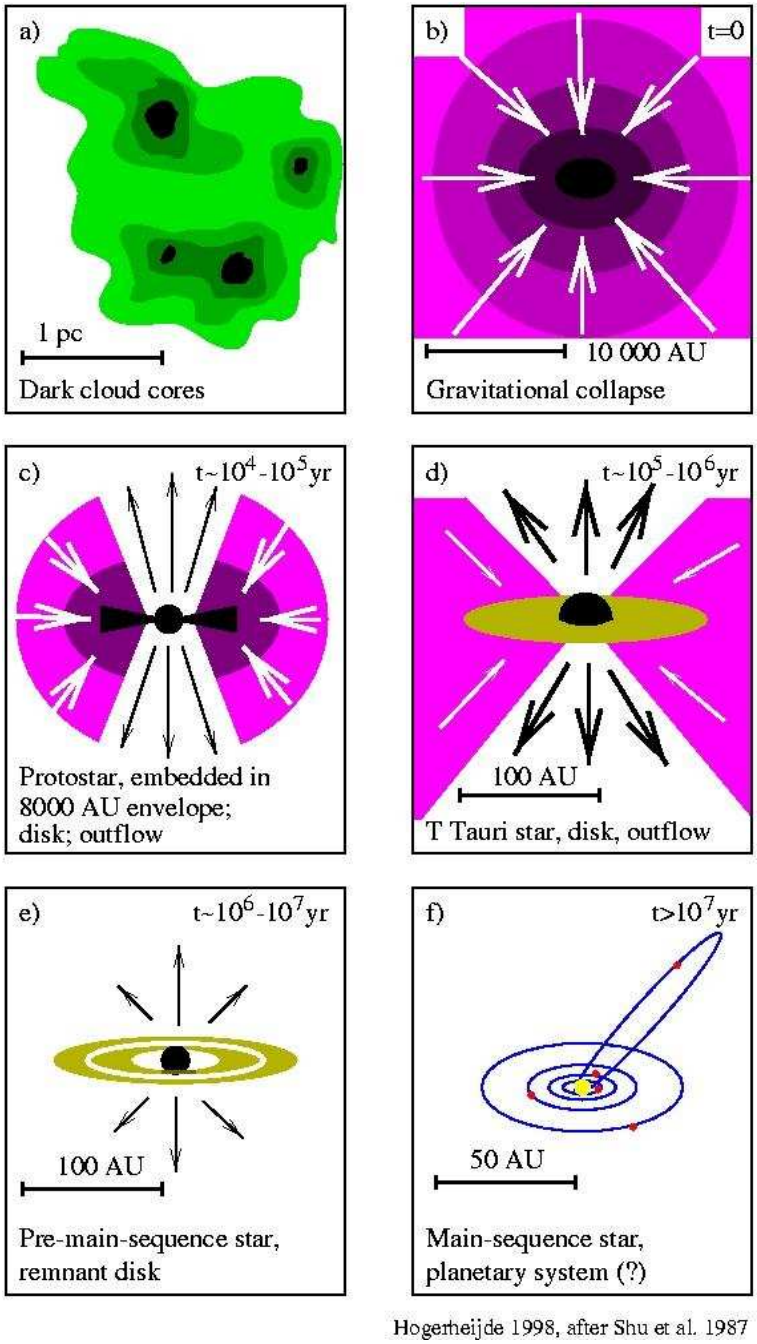

Figure 2.2: The birth of a star. Schematic overview of the different phases: (a) prestellar cores, (b) infalling protostar (Class 0), (c) embedded protostar (Class 1), (d) classical T Tauri star surrounded by an optically thick disc (Class 2), (e) weak-line T Tauri star with an optically thin disc (Class 3), (f) main-sequence star with possible planetary system. (from Hogerheijde 1998).

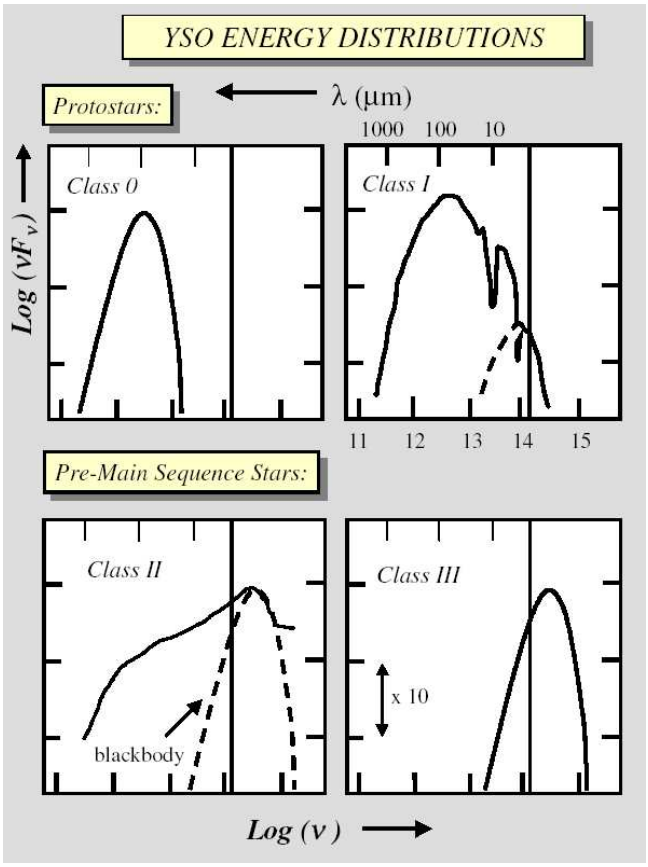

Figure 2.3: The classification scheme of YSOs according to their SEDs. The vertical line is at the wavelength of 2.2 μm (from Lada 2001).

Class 0 and 1 objects are characterised by SEDs that rise with wavelength ($\alpha_{\rm IR} > 0$) and peak in the submillimetre or far infrared (FIR) range. This indicates that these objects are surrounded by a massive infalling envelope of gas and dust, which absorbs the radiation of the protostar and re-radiates it at much longer wavelengths. Class 0 sources are deeply embedded protostars that show a large sub-mm ($\lambda > 350$ μm) to bolometric luminosity ratio ($L_{\rm smm}/L_{\rm bol} > 0.005$). Most of the Class 0 sources are not detected at wavelengths $\lambda < 20$ μm. The Class 0 stage is the main accretion phase and lasts only a few 10^4 years. Class 1 objects are relatively evolved protostars with ages around $1 - 5 \times 10^5$ years surrounded by an accretion disc and a circumstellar envelope of substellar mass ($M_{\rm env} \lesssim 0.3\,{\rm M}_\odot$). The transition phase between Class 0 and 1 is believed to take place when the envelope mass is about equal to the mass of the protostar. Another indicator for the class division is the bolometric temperature $T_{\rm bol}$: Class 0 corresponds to protostars with $T_{\rm bol} < 70\,{\rm K}$ and Class 1 to objects with $70\,{\rm K} < T_{\rm bol} < 650\,{\rm K}$.

Pre-main-sequence stars in Class 2 and 3 correspond to classical T Tauri stars

Table 2.3: Evolutionary classes: basic properties

Class	SED peak	$\alpha_{\rm IR}$	type	disc	lifetime [yrs]
0	FIR/submm	> 0	infalling protostar, deeply embedded	building up	10^4
1	FIR	> 0	embedded protostar	opt. thick	10^5
2	optical/NIR	$-1.5...0$	CTTS	opt. thick	$10^6...10^7$
3	optical/NIR	< -1.5	WTTS	opt. thin	$10^6...10^7$

(CTTSs) and weak-line T Tauri stars (WTTSs), respectively. They are characterised by a circumstellar disc (optically thick in Class 2, optically thin in Class 3) and the lack of a dense circumstellar envelope. The SED of Class 2 objects peaks at visible or near infrared (NIR) wavelengths and shows excess infrared as well as excess ultraviolet radiation. Class 3 objects have their maximum emission in the optical or NIR as well, and they are strong X-ray sources. The spectral index of Class 2 objects is in the range $-1.5 < \alpha_{\rm IR} < 0$, while Class 3 objects have $\alpha_{\rm IR} < -1.5$. Pre-main sequence stars are sometimes also classified by their Hα equivalent width, which is > 10 Å for Class 2 and < 10 Å for Class 3. T Tauri stars still accrete mass from their envelope, however at a much lower rate than protostars. Their lifetimes are estimated to be in the range between 10^6 to 10^7 years.

The four classes of YSOs are usually interpreted as an evolutionary sequence: Class 0 → Class 1 → Class 2 → Class 3 (e.g. Adams et al. 1987; André et al. 2000; see also Fig. 2.2). However, there are concerns that some Class 0 sources might be mimicked by Class 1 objects seen edge on (Men'shchikov & Henning 1997). Furthermore there is evidence suggesting that Class 2 and Class 3 objects are of the same age (Walter 1986; Gras-Velázquez & Ray 2005).

The progenitors of young stellar objects are prestellar cores (also called starless cores or prestellar condensations). These are gravitationally bound, dense molecular cloud cores with typical stellar masses that may already be in a state of collapse, but have not formed a central protostellar object yet. However, some cores considered so far as "starless" seem to harbour embedded sources (Young et al. 2004).

There seems to be some inconsistency concerning the nomenclature in the literature. Throughout this work, the term *protostars* refers to Class 0 and 1 sources, while the term *pre-main sequence (PMS) stars* designates Class 2 and 3 objects. *Young stellar objects* is the generic term for objects from the formation of the protostellar core until the arrival on the main sequence, thus it encompasses both, protostars and PMS stars.

2.8 The Mass of a Star

The mass of a star is certainly its most important property. Although the Russell-Vogt theorem (Vogt 1926; Russell et al. 1927), which states that the evolution of stars is fixed at their birth by two inherent fundamental parameters, mass and chemical composition, has turned out to be slightly incorrect, it is nevertheless the star's mass at birth, which determines most of its essential parameters like lifetime, luminosity, temperature, radius, or density profile (Massey & Meyer 2001). The mass-luminosity relation is considered one of the most fundamental descriptions of stellar properties. This relation, as well as the lifetime as a function of time, show a different behaviour for high-mass stars than for solar-mass stars.

Stellar masses span a wide range between 0.08 and about 150 $M_\odot$. Below 0.08 $M_\odot$, the temperature in the stellar core is not high enough to ignite hydrogen. Objects with masses below this limit and over 0.01 $M_\odot$ (about 10 Jupiter masses) may only burn deuterium in their cores. These are Brown Dwarves. While there is a natural lower limit to the mass of a star, it is not clear, if there exists an upper limit, and if yes, what causes it. Observations indicate that no stars with masses larger than 150 $M_\odot$ exist (Figer 2005). Stellar masses can either be determined in binary systems using Kepler's laws or be inferred from theoretical models using observational estimates on age, luminosity and temperature.

The stellar initial mass function (IMF) describes the distribution of masses with which stars are formed. The IMF is the most fundamental output function of the star formation process (see Larson 1999, Meyer et al. 2000, Pudritz 2002, or Kroupa 2002 for reviews). It can be written as

$$\xi(M) = cM^{-(1+x)}, \tag{2.7}$$

with the original value of $x = 1.35$ (Salpeter 1955). Observations of different star-forming regions reveal an apparently universal form of the IMF: It has a characteristic stellar mass of the order of 1 $M_\odot$, and a power-law decline similar to or somewhat steeper than the original Salpeter (1955) slope at masses $M > 1\,M_\odot$. It flattens over lower masses and peaks at a few tenths of a solar mass, declining again toward the lowest masses.

The apparent universality of the IMF is still a challenge for star formation theory, since variations according to the different initial conditions in different star-forming regions are expected. It is suspected that the characteristic stellar mass is caused by a characteristic scale of fragmentation in star-forming clouds which is essentially the Jeans scale as given by the typical temperature and pressure in molecular clouds. The power-law decline of the IMF at large masses suggests that the most massive stars are built up by scale-free accretion or accumulation processes, with interactions between dense prestellar clumps or protostars playing a role as well. The thermal properties of star-forming clouds seem to have an important influence on the fragmentation behaviour. At least for low-mass stars the IMF probably depends on the detailed thermal physics of the cloud (Larson 2005). This is supported by numerical simulations of cloud collapse and fragmentation

showing that the equation of state plays an important role in the fragmentation of clouds and the determination of the IMF (Li et al. 2003; Jappsen et al. 2005).

Chapter 3

Numerical Simulations

Computers are useless. They can only give you answers.
– Pablo Picasso

As outlined in the previous chapter, star formation is a highly complex and chaotic process involving many different physical processes and a wide range of scales. Observations of molecular clouds and nascent stars are the base of all star formation theories, however, it requires models to obtain a self-consistent picture of the entire process. Analytical models are restricted to describe the collapse of isolated, idealised objects. Therefore, numerical simulations play a central role in understanding the process of star formation. The first numerical collapse calculations have been performed by Bodenheimer & Sweigart (1968), Larson (1969) and Hunter (1977). While these early works were restricted to a single sphere, numerical simulations are meanwhile able to follow the entire evolution from the fragmentation and collapse of a molecular cloud to the build-up of a stellar cluster. Before we describe the simulations used for this study, the basics of hydrodynamics and the concept of Smoothed Particle Hydrodynamics will be briefly outlined. A detailed description of hydrodynamical concepts, and especially their application to astrophysical problems is given e.g. by Shu (1992).

3.1 Some Basics of Hydrodynamics

The common approach to study the motion of fluids and gases is by *hydrodynamics*. In this picture, gases and fluids are large ensembles of interacting particles (atoms, molecules, electrons, dust particles, etc.). The state of the system is described by its location in the $6N$-dimensional phase space, where N is the number of particles. The temporal evolution is governed by the equation of motion in phase space. Since an exact solution is almost impossible for a large number of particles, in analogy to quantum mechanics a probabilistic approach is used. The exact location of the system in phase space is then described by the N-body probability distribution

$$f^{(N)}(\vec{q_1}...\vec{q_N}, \vec{p_1}...\vec{p_N})\, d\vec{q_1}...d\vec{q_N}, d\vec{p_1}...d\vec{p_N}. \tag{3.1}$$

Since observables are usually associated with a one- or two-body probability density $f^{(1)}$ or $f^{(2)}$, the probability distribution can be reduced from $f^{(N)}$ to $f^{(n)}$ by integrating over all but n variables. This leads to the so-called BBGKY-hierarchy (named after Born, Bogoliubov, Green, Kirkwood, and Yvon) of equations of motion. To solve this system of equations, a specific approximation to terminate it is required. The lowest level of the hierarchy is represented by the one-body distribution function $f^{(1)}(\vec{q}, \vec{p}, t)$. It describes the probability of finding a particle at time t in the volume element $d^3\vec{q}$ at the location $\vec{q}$ with momenta in the range $d^3\vec{p}$ at $\vec{p}$. The equation of motion for $f^{(1)}$ is called Boltzmann equation:

$$\frac{df}{dt} \equiv \frac{\partial f}{\partial t} + \dot{\vec{q}}\vec{\nabla}_q f + \dot{\vec{p}}\vec{\nabla}_p f = \frac{\partial f}{\partial t} + \vec{v}\vec{\nabla}_q f + \vec{F}\vec{\nabla}_p f = f_c. \tag{3.2}$$

The first part corresponds to the transformation from a comoving to a spatially fixed coordinate system. The second part gives the velocity as $\vec{v} = \dot{\vec{q}}$ and the force as $\vec{F} = \dot{\vec{p}}$. All higher order terms from the BBGKY-hierarchy are contained in the collision term f_c. Since the observable quantities are typically moments of the Boltzmann equation, this allows a further simplification of the description of the system. If the expansion of the Boltzmann equation into moments yields well-defined quantities, the thermodynamic approximation is valid. This is the case, if the distribution function is a smoothly varying function on the scales of interest, i.e., if the averaging scale is larger than the mean free path of individual particles. However, there are some limitations to this approximation. It does not work e.g. in the case of shocks or phase transitions, and it cannot be applied to fully fractal systems.

A problem in hydrodynamics is book-keeping, i.e. keeping track of the changes in quantities such as mass, momentum or energy of a fluid element according to the physical processes acting on it. There are two methods to achieve this. The *Eulerian* approach needs a three-dimensional grid of fixed points. The book-keeping is done by determining the changes (e.g. fluxes through the cell surfaces defined by the grid) over a huge number of tiny time intervals. The *Lagrangian* approach, on the other hand, does not require a grid. The fluid is represented by a large number of moving interpolation points which follow the motion of the fluid. Each point carries a fixed mass and can be considered as a particle.

The hydrodynamic equations are a set of equations for the conserved quantities (ρ, $\rho\vec{v}$, ϵ) plus a closure equation (the equation of state). The hydrodynamic equations needed to describe a self-gravitating compressible fluid are:

$$\frac{d\rho}{dt} = \frac{\partial \rho}{\partial t} + \vec{v} \cdot \vec{\nabla}\rho = -\rho\vec{\nabla} \cdot \vec{v} \tag{3.3}$$

(continuity equation)

$$\frac{d\vec{v}}{dt} = \frac{\partial \vec{v}}{\partial t} + (\vec{v} \cdot \vec{\nabla})\vec{v} = -\frac{1}{\rho}\vec{\nabla}p - \vec{\nabla}\phi + \eta\vec{\nabla}^2\vec{v} + (\zeta + \frac{\eta}{3})\vec{\nabla}(\vec{\nabla} \cdot \vec{v}) \tag{3.4}$$

(Navier-Stokes equation)

$$\frac{d\epsilon}{dt} = \frac{\partial\epsilon}{\partial t} + \vec{v}\cdot\vec{\nabla}\epsilon = T\frac{ds}{dt} - \frac{p}{\rho}\vec{\nabla}\cdot\vec{v} \tag{3.5}$$

(energy equation)

$$\vec{\nabla}^2\phi = 4\pi G\rho \tag{3.6}$$

(Poisson's equation)

$$p = \mathcal{R}\rho T \tag{3.7}$$

(equation of state)

where ρ denotes the density, $\vec{v}$ the velocity, p the pressure, and ϕ the gravitational potential, ζ and η are viscosity coefficients, $\epsilon = \rho\vec{v}^2/2$ is the kinetic energy density, T the temperature, s the entropy, and $\mathcal{R}$ the gas constant. If external forces (e.g. gravity or a magnetic field) are present, additional evolution equations for the sources that generate these forces are needed.

3.2 Smoothed Particle Hydrodynamics

The concept of Smoothed Particle Hydrodynamics (SPH) was introduced independently by Lucy (1977) and Gingold & Monaghan (1977). Detailed reviews can be found in Monaghan (1985, 1992), Benz (1990), or Price (2004), the code basics are given in Monaghan (2001). SPH is a Lagrangian method where the fluid is represented by an ensemble of particles i, each having mass m_i, momentum $m_i\vec{v}_i$ and hydrodynamic properties such as pressure, temperature, internal energy or entropy. The temporal evolution is governed by the equation of motion plus additional equations to modify the hydrodynamic properties of the particles. Hydrodynamic observables are obtained by a local averaging process. Representing a Lagrangian approach, SPH does not need a grid to calculate spatial derivatives, instead, they are found by analytical differentiation of interpolation formulae.

In SPH each particle is associated with a smoothing length h, representing the finite spatial extent of the particle, which can differ in value for separate particles, as well as vary in time. Only those particles lying within the smoothing length of another can interact with that one, apart from gravity. Mass is conserved automatically, so there is no need to solve a continuity equation. Local averages for any quantity $f(\vec{r})$ at a position $\vec{r}$ can be obtained by summing contributions from all those particles j whose smoothing volume overlaps with $\vec{r}$, weighted by an appropriate smoothing function (*smoothing kernel*) $W(\vec{r}, \vec{h})$:

$$\langle f(\vec{r})\rangle = \int f(\vec{r})W(|\vec{r} - \vec{r_j}|, h_j)d^3r'. \tag{3.8}$$

The optimum value of h is such that every particle has about 50 neighbours within the smoothing volume.

SPH is able to resolve large density contrasts as particles are free to move and so naturally the particle concentration increases in high-density regions. This makes SPH an obvious and very powerful tool to simulate the star formation process. Consequently, it has been used extensively for this purpose (e.g. Klessen & Burkert 2000, 2001; Bate et al. 2003; Bonnell et al. 2003, 2004; Hennebelle et al. 2003; Delgado-Donate et al. 2003, 2004; Goodwin et al. 2004a,b; Bate & Bonnell 2005).

Bate & Burkert (1997) have shown that gravitational fragmentation is reproduced properly by SPH (i.e., no artificial fragmentation occurs, while true fragmentation is captured) provided (1) gravity and pressure are smoothed in the same way, and (2) the minimum resolvable mass is always less than the local Jeans mass. Proper resolution requires about twice the number of neighbours, i.e. ∼100 particles. It has been criticised that this criterion may not be sufficient and may produce artificial fragmentation leading to false multiple fragmentation (Klein et al. 2004). However, Hubber et al. (2006) show that SPH indeed simulates gravitational fragmentation properly, even at low resolution. Unlike other claims it is very likely that (given the same input physics and initial conditions) grid- and particle-based codes behave in a similar way concerning fragmentation (Gawryszczak et al. 2005).

3.3 The Models

To adequately describe the fragmentation of turbulent, self-gravitating gas clouds and the resulting formation and mass growth of protostars, we need to resolve the dynamical evolution of collapsing cores over several orders of magnitude in density. Due to the stochastic nature of supersonic turbulence, it is not known in advance where and when this local collapse occurs. As discussed in the previous section, we resort to SPH to solve the equations of hydrodynamics. We use the same smoothing procedure for gravity and pressure forces. This is needed to prevent artificial fragmentation (Bate & Burkert 1997). Because it is computationally prohibitive to treat the cloud as a whole, we concentrate on subregions within the cloud and adopt periodic boundary conditions (Klessen 1997). Once the central region of a collapsing protostellar core exceeds a density contrast of $\sim 10^5$, it is replaced by a so-called *sink particle* (Bate et al. 1995), which has the ability to accrete gas from its surrounding while at the same time keeping track of mass as well as linear and angular momentum. By adequately replacing high-density cores with sink particles we can follow the dynamical evolution of the system over many free-fall times.

We determine the resolution limit of our SPH calculations using the Bate & Burkert (1997) criterion. This is sufficient for the highly nonlinear density fluctuations created by supersonic turbulence as confirmed by convergence studies with up to 10^7 SPH particles (Jappsen et al. 2005; Li et al. 2005).

The suite of models studied here consists of two globally unstable models that contract from Gaussian initial conditions without turbulence (for details see

Table 3.1: Overview of all models.

Name	$\mathcal{M}$	k	n_p	M_min [$\mathrm{M}_\odot$]	M_accr [%]	n_*	t_grav
G1	–	–	50 000	0.44	93.1	56	0.0
G2	–	–	500 000	0.044	84.9	56	0.0
M01k2	0.1	1..2	205 379	0.058	74.9	95	200.0
M01k4	0.1	3..4	205 379	0.058	27.2	3	200.0
M01k8	0.1	7..8	205 379	0.058	85.9	3	200.0
M05k2	0.5	1..2	205 379	0.058	37.2	23	100.0
M05k4	0.5	3..4	205 379	0.058	77.9	48	100.0
M05k8	0.5	7..8	205 379	0.058	59.5	48	100.0
M2k2	2	1..2	205 379	0.058	75.1	68	25.0
M2k4	2	3..4	205 379	0.058	47.9	62	25.0
M2k8	2	7..8	205 379	0.058	66.2	42	25.0
M3k2	3.2	1..2	205 379	0.058	79.7	65	4.0
M3k4	3.2	3..4	205 379	0.058	82.1	37	3.0
M3k8	3.2	7..8	205 379	0.058	60.2	17	4.0
M6k2a	6	1..2	205 379	0.058	85.4	100	15.0
M6k4a	6	3..4	205 379	0.058	62.4	98	15.0
M6k2b	6	1..2	195 112	0.058	34.5	50	2.0
M6k4b	6	3..4	50 653	0.058	29.7	50	2.0
M6k8b	6	7..8	50 653	0.058	35.7	25	2.0
M6k2c	6	1..2	205 379	0.058	75.8	110	1.5
M6k4c	6	3..4	205 379	0.058	61.9	53	1.5
M6k8c	6	7..8	205 379	0.058	6.4	12	2.0
M10k2	10	1..2	205 379	0.058	56.5	150	6.1
M10k8	10	7..8	205 379	0.058	32.4	54	6.1

Klessen & Burkert 2000, 2001) and of 22 models where turbulence is maintained with constant rms Mach numbers $\mathcal{M}$, in the range $0.1 \leq \mathcal{M} \leq 10$. We distinguish between turbulence that carries its energy mostly on large scales, at wave numbers $1 \leq k \leq 2$, on intermediate scales, i.e. $3 \leq k \leq 4$, and on small scales with $7 \leq k \leq 8$. The corresponding wavelengths are $\lambda = L/k$, where L is the total size of the computed volume. The models are labelled mnemonically as M$\mathcal{M}$kk, with rms Mach number $\mathcal{M}$ and wave number k, while G1 and G2 denote the two Gaussian runs. Table 3.1 lists all the relevant details of the models: Mach number $\mathcal{M}$, driving wave number k, the number of particles in the simulation n_p, the SPH resolution limit M_min (requiring that the local Jeans mass is always resolved by at least 100 gas particles; Bate & Burkert 1997), the fraction of the total mass that has been accreted by the end of the simulation M_accr, the number of formed protostars n_*, and the time t_grav when gravity is "switched on".

To have well defined environmental conditions given by $\mathcal{M}$ and k, $\mathcal{M}$ is required to be constant throughout the evolution. However, turbulent energy dissipates rapidly, roughly on a free-fall timescale (Mac Low et al. 1998; Stone et al. 1998; Padoan & Nordlund 1999). We therefore apply a non-local driving scheme that inserts energy at a given rate and at a given scale k. We use Gaussian random fluctuations in velocity. This is appealing because Gaussian fields are fully determined by their power distribution in Fourier space. We define a Cartesian mesh with 64^3 cells, and for each three-dimensional wave number $\vec{k}$ we randomly select an amplitude from a Gaussian distribution around unity and a phase between zero and 2π. We then transform the resulting field back into real space to get a "kick-velocity" in each cell. Its amplitude is determined by solving a quadratic equation to keep $\mathcal{M}$ constant (Mac Low 1999; Klessen et al. 2000). The "kick-velocity" is then simply added to the speed of each SPH particle located in the cell. We adopted this method for mathematical simplicity. In reality, the situation is far more complex. Still, our models of large-scale driven clouds contain many features of molecular clouds in supernovae-driven turbulence (e.g. Ballesteros-Paredes & Mac Low 2002; Mac Low et al. 2004). Conversely, our models of small-scale turbulence bear certain resemblance to energy input on small scales provided by protostellar feedback via outflows and winds.

Our models neglect the influence of magnetic fields, because their presence cannot halt the decay of turbulence (Mac Low et al. 1998; Stone et al. 1998; Padoan & Nordlund 1999) and does not significantly alter the efficiency of local collapse for driven turbulence (Heitsch et al. 2001a). More importantly, we do not consider feedback effects from the star formation process itself (like bipolar outflows, stellar winds, or ionising radiation from new-born O or B stars). Our analysis of protostellar mass accretion rates focuses solely on the interplay between turbulence and self-gravity. This is also the case in the Shu (1977) theory of isothermal collapse. Hence, our findings can be directly compared to the "standard theory of star formation" (§ 2.4).

3.4 Physical Scaling

The dynamical behaviour of isothermal self-gravitating gas is scale free and depends only on the ratio α between internal energy and potential energy:

$$\alpha = \frac{E_{\rm int}}{|E_{\rm pot}|}. \tag{3.9}$$

This scaling factor can be interpreted as a dimensionless temperature. We convert to physical units by adopting a physical temperature of 11.3 K corresponding to an isothermal sound speed $c_{\rm s} = 0.2\,{\rm km\,s^{-1}}$, and a mean molecular weight $\mu = 2.36$, corresponding to a typical value in solar-metallicity Galactic molecular clouds. With an average number density $n = 10^3\,{\rm cm^{-3}}$, which is consistent with the typical density in the considered star-forming regions, the total mass in the two Gaussian

models is 2311 $M_\odot$, and the size of the cube is 3.4 pc. The turbulent models have a mass of 1275 $M_\odot$ within a volume of $(2.8\,\mathrm{pc})^3$. The global free-fall timescale is $\tau_{\mathrm{ff}} = 10^6$ yr. If we instead focus on individual dense cores like in ρ Ophiuchi with $n \approx 10^5\,\mathrm{cm}^{-3}$ (Motte et al. 1998), the total masses in the Gaussian and in the turbulent models are 231 $M_\odot$ and 128 $M_\odot$, respectively, and the volumes are $(0.34\,\mathrm{pc})^3$ and $(0.28\,\mathrm{pc})^3$, respectively. This corresponds to 220 thermal Jeans masses. The turbulent models have a mass of 120 $M_\odot$ within a volume of $(0.28\,\mathrm{pc})^3$, equivalent to 120 thermal Jeans masses[1]. The mean thermal Jeans mass in all models is thus $\langle M_{\mathrm{J}} \rangle = 1\,M_\odot$, the global free-fall timescale is $\bar{\tau}_{\mathrm{ff}} = 10^5$ yr, and the simulations cover a density range from $n(\mathrm{H}_2) \approx 100\,\mathrm{cm}^{-3}$ in the lowest density regions to $n(\mathrm{H}_2) \approx 10^9\,\mathrm{cm}^{-3}$ where collapsing protostellar cores are identified and converted into sink particles in the code. This coincides in time with the formation of the central protostar to within $\sim 10^3$ yr (Wuchterl & Klessen 2001).

Note that only the derived numerical values of physical parameters (mass...) are influenced by the adopted physical scaling, but neither the dynamical evolution or the number of stars. For further details on the scaling behaviour of the models see Klessen & Burkert (2000) and Klessen et al. (2000).

3.5 Determination of the YSO Classes

The evolutionary classes of YSOs are defined on the basis of observational properties, in particular their SED in the millimetre and infrared range (§ 2.7). Thus, we have to 'translate' those criteria such that they can be conveniently applied to the simulations. The basic parameter indicating the evolutionary stage of a YSO is its mass, or rather the ratio of the current to the final mass (M/M_{end}). The beginning of Class 0 is identified with the formation of the first hydrostatic core. This happens when the central object has a mass of about 0.01 $M_\odot$ (Larson 2003). The transition from Class 0 to Class 1 is reached when the envelope mass is equal to the mass of the central protostar (André et al. 2000). The determination of the end of the Class 1 stage is more difficult, since this is usually done via spectral indices in the near-infrared part of the SED. Generally, after the Class 1 stage the objects are considered classical T Tauri stars that become visible in the optical. Hence we determine the transition from Class 1 to Class 2 when the optical depth of the remaining envelope becomes unity at 2.2 μm (K-band). Using the evolutionary scheme of Smith (2000) and the standard parameters as described in Froebrich et al. (2006) the end of Class 0 corresponds to a mass of $M_* \approx 0.43\ M_{\mathrm{end}}$, where M_{end} denotes the final mass of the star. The end of Class 1 is reached when $M_* \approx 0.85\ M_{\mathrm{end}}$. Note that the exact value of the mass at the transition from one phase to the next does not influence our results significantly. Even a change of the opacity value by a factor of four results in a deviation of the corresponding mass of a few per cent

[1] We use a spherical definition of the Jeans mass, $M_{\mathrm{J}} \equiv 4/3\,\pi\rho(\lambda_{\mathrm{J}}/2)^3$ (Equation 2.2), with density ρ and Jeans length $\lambda_{\mathrm{J}} \equiv \left(\frac{\pi \mathcal{R} T}{G\rho}\right)^{1/2}$ and where G and $\mathcal{R}$ are the gravitational and the gas constant. The mean Jeans mass $\langle M_{\mathrm{J}} \rangle$ is then determined from the average density in the system $\langle \rho \rangle$.

only. Lacking a feasible criterion to distinguish Class 2 from Class 3 objects, we consider both classes combined. The same is done for the observational data.

Finding and defining prestellar cores is a more difficult task. Usually one considers roughly spherical symmetrical density enhancements containing no visible traces of protostars (e.g. Motte et al. 1998; Johnstone et al. 2000). We attempt to follow this procedure and define prestellar cores from the Jeans-unstable subset of all molecular cloud cores identified in our models. We use a three-dimensional clump-finding algorithm to determine the cloud structure, similar to the method of Williams et al. (1994). Further detail is given in Appendix A of Klessen & Burkert (2000). This procedure matches many of the observed structures and kinematic properties of nearby starless molecular cloud cores (see the discussions in Ballesteros-Paredes et al. 2003 and Klessen et al. 2005).

Chapter 4

Observations

Hard to see, the dark side is.
– Yoda in Star Wars Episode I: The Phantom Menace

Since stars are born in dark clouds of gas and dust, their formation process is hard to observe, at least in the optical wavelength range. Therefore, other wavelengths, where extinction by interstellar dust plays a less dominant role, like radio, (sub)millimetre or infrared bands are preferred. Nevertheless, almost the entire electromagnetic spectrum can be used to study different aspects of star formation (see Table 4.1). Especially the combination of observations in different wavelengths is very helpful in identifying and classifying young stars.

The results of the numerical simulations described in the previous chapter are going to be compared with observational data, therefore some of the most important observational methods, their application and their limitations will be discussed below. This description is by no means exhaustive, for more details the reader is referred to Smith (2004), van Dishoeck (2004), or Myers et al. (2000), a detailed description of the physical processes responsible for the observed radiation can be found e.g. in Stahler & Palla (2004).

4.1 Radio and Millimetre

Most of our knowledge about molecular clouds comes from radio astronomy. The 21 cm (1420 MHz) line of neutral atomic hydrogen (HI) is used to study the large-scale structure of the atomic interstellar medium. The gas in molecular clouds (mainly H_2 and He) is much too cold to radiate, but it may be detected due to collisions with heavier tracer molecules such as CO, NH_3, HCN, or H_2O. Those molecules are visible by emission in spectral lines due to rotational transitions. The most abundant tracer of the gas is CO (10^{-4} times the abundance of H_2). It is observed not only in the line of ^{12}CO at 2.6 mm, but also in the lines of other isotopes like ^{13}CO or C^{18}O.

Table 4.1: The electromagnetic spectral bands and their relevance for star formation studies. (Note that there is no strict definition of the wavelength ranges, therefore the given boundaries may differ slightly in the literature.)

Range	Wavelength	Extinction	objects traced (examples)
Radio/mm	$> 1\,\mathrm{mm}$	low	large-scale distribution of clouds
submm	$0.1 - 1\,\mathrm{mm}$	low	embedded protostars
far IR	$20 - 100\,\mu\mathrm{m}$	low	embedded protostars
mid IR	$5 - 20\,\mu\mathrm{m}$	low	protostars
near IR	$0.8 - 5\,\mu\mathrm{m}$	low	protostars
optical	$400-800\,\mathrm{nm}$	high	nebulosities of molecular clouds
UV	$10-400\,\mathrm{nm}$	high	T Tauri stars, outflows
X-rays	$0.01-10\,\mathrm{nm}$	moderate	T Tauri stars, jets, outflows
γ-rays	$< 0.01\,\mathrm{nm}$	moderate	large-scale structure of ISM

4.2 Infrared and Submillimetre

Since infrared radiation suffers much less from extinction than the visible light, and since YSOs show strong emission in this wavelength range, the IR is ideally suited to study young stars. As described in § 2.7 the evolutionary classification of YSOs is based on their submm- and IR emission. The SED of embedded protostars (Class 0 and 1) peaks in the FIR or submm range, that of T Tauri stars in the NIR or optical. While the NIR bands *J*, *H*, *K* can be observed from the ground, the mid- and far-IR wavelengths are absorbed by the Earth's atmosphere and can only be observed from space. The most important spaceborne telescopes are the European *Infrared Space Observatory* (ISO, operational from 1995 to 1998) and NASA's *Spitzer Space Telescope* (launched in 2003). Both devices led to numerous important discoveries in the field of star formation (e.g. Bacmann et al. 2000; Bontemps et al. 2001; Kaas & Bontemps 2001; Kaas et al. 2004).

4.3 X-rays

Young stellar objects in all evolutionary stages from Class 1 until the approach of the main sequence, T Tauri stars in particular, show increased X-ray emission (on a much higher level than main sequence stars). The X-ray radiation is believed to be thermal emission from gas rapidly heated to temperatures around $10^7\,\mathrm{K}$ by violent magnetohydrodynamic reconnection events (see Feigelson & Montmerle 1999 for a detailed review). Since X-rays with energies above $\sim 1\,\mathrm{keV}$ are much less affected by extinction than the optical wavelength range, they permit a deep look into dense molecular cloud cores. Like the infrared, the X-ray regime has

to be observed from outside the Earth's atmosphere. The X-ray satellites *ROSAT*, *XMM-Newton* and *Chandra* have been frequently used to carry out surveys of star formation regions and have successfully discovered or confirmed a large number of embedded YSOs (e.g. Neuhäuser & Sterzik 1997; Preibisch 2003; Preibisch & Zinnecker 2002, 2004).

4.4 Other Wavelengths

The optical wavelength range suffers from strong dust extinction and is therefore less suited for star formation studies. However, cold interstellar gas can be detected by atomic hydrogen absorption lines in the visible, if the cloud is back-lit by a star. Pre-main sequence stars also radiate significantly in the optical, however, their emission may be extincted by the molecular cloud.

T Tauri stars show a weak continuum and several strong emission lines in the ultraviolet (UV). The observed continuum emission can be significantly stronger than in comparable main sequence stars. This UV excess is stronger in CTTSs than in WTTSs. The reason for the UV excess is not entirely clear, probably it is caused by several components, in particular the dissipation of gravitational energy at the boundary layer between the accretion disc and the star (see Gómez de Castro 1998 for a review).

Gamma rays do not play an important role in the context of star formation. However, the radioactive isotope ^{26}Al emitting γ-rays may be used to probe the large-scale distribution of the interstellar medium (Strong et al. 1982) and to estimate the Galactic star formation rate (Diehl et al. 2006). Furthermore, γ-ray production from accelerators within star-formation regions (e.g. Wolf-Rayet stars or supernova remnants) is expected from theoretical models (Paul 2001).

4.5 Uncertainties and Caveats

Despite the advanced observational methods, the data used is far from being complete. Due to the high level of obscuration in star-forming regions and due to the different techniques involved, uncertainties in the observations are almost unavoidable: Samples of clusters may be incomplete and the cluster membership of individual objects questionable. The classification of YSOs may suffer from insufficient data for the SED as well as from different classification criteria. To address this, Froebrich (2005) compiled a complete list of known Class 0 sources from the literature and used these data to determine the physical properties ($T_{\rm bol}$, $L_{\rm bol}$, $L_{\rm smm}/L_{\rm bol}$, $M_{\rm env}$) in order to provide a uniform classification.

For this work, different observational data from a large number of various literature sources will be used. For the analysis and comparison of protostellar mass accretion rates (§ 5) and evolutionary tracks (§ 6) data of individual objects in various star-forming regions are used, whereas the investigation of YSO number ratios

and structures of young star clusters (§ 7 and 8, respectively) requires a sample of entire YSO cluster contents as complete as possible.

Chapter 5

Protostellar Mass Accretion Rates*

Gravity, no escaping gravity...
– Placebo: Special K

Almost the entire mass of a star is accumulated during a relatively short phase (in Class 0 and 1 stage). Since the mass of a star is one of the most important parameters, which determines many of its properties, it is essential to understand the process how a protostar gains its mass. In the so-called "standard theory" of star formation (Shu 1977; Shu et al. 1987) the mass accretion rate has a constant value. Observations, as well as more advanced models, however, indicate that protostellar mass accretion is a highly time-variant process. In this chapter the analysis of protostellar mass accretion rates is extended from a single case (Klessen 2001a) to the entire series of numerical models of turbulent molecular cloud fragmentation that covers the entire spectrum of observed star-forming regions, ranging from inefficient and isolated star formation to the fast and efficient build-up of stellar clusters.

5.1 First Approximation

The entire process of molecular cloud collapse and build-up of the stellar cluster lasts several global free-fall times ($\bar{\tau}_{\rm ff} = 10^5$ yr). Likewise, the accretion process of a protostellar core takes place on a timescale of a few $\bar{\tau}_{\rm ff}$, comparable to most other models of star formation.

A simple approximation of the accretion rate can be achieved by dividing the local Jeans mass by the local dynamical timescale:

$$\dot{M} \approx M_{\rm J}/\tau_{\rm ff} \tag{5.1}$$

*This chapter is based on Schmeja, S., & Klessen, R. S. 2004, A&A, 419, 405

By substituting

$$M_{\rm J} = \frac{\pi^{5/2}}{6}\rho_0^{-1/2}\left(\frac{\mathcal{R}T}{G}\right)^{3/2} = \frac{\pi^{5/2}}{6}\rho_0^{-1/2}G^{-3/2}c_{\rm s}^3, \tag{5.2}$$

where ρ_0 denotes the initial density, T the temperature, $c_{\rm s}$ the isothermal sound speed, G the gravitational constant, and $\mathcal{R}$ the gas constant, and

$$\tau_{\rm ff} = \sqrt{\frac{3\pi}{32\,G\rho_0}}, \tag{5.3}$$

Eq. (5.1) can be written as

$$\dot{M} \approx \frac{M_{\rm J}}{\tau_{\rm ff}} = \sqrt{\frac{32}{3}}\frac{\pi^2}{6}\frac{c_{\rm s}^3}{G} = 5.4\,\frac{c_{\rm s}^3}{G}, \tag{5.4}$$

depending only on the isothermal sound speed (or temperature). For a sound speed $c_{\rm s} = 0.2$ km s^{-1} we obtain $\dot{M} = 10^{-5}$ M$_\odot$ yr^{-1}. This is higher than the accretion rate for the collapse of a singular isothermal sphere: $\dot{M} = 0.975\,c_{\rm s}^3/G$ (Shu 1977). However, the accretion rates in our models vary with time. Typical peak accretion rates are roughly in the range $(3-50)\,c_{\rm s}^3/G$ or 5×10^{-6} to 10^{-4} M$_\odot$ yr^{-1}. The values exceed the approximated value $M_{\rm J}/\tau_{\rm ff}$ due to external compression in the turbulent flow.

5.2 Determination of Mass Accretion Rates

In the protostellar phase of evolution, we determine accretion rates $\dot{M}$ by measuring the amount of mass as a function of time that falls into a control volume defined by each sink particle. Its radius is fixed to 280 AU. Infalling gas particles undergo several tests to check if they remain bound to the sink particle before they are considered accreted (see e.g. Appendix A of Jappsen et al. 2005). As all gas particles have the same mass and as accretion events occur at random times, the resulting accretion rates are mass-binned and we smooth over a few consecutive accretion events to get a meaningful description of the temporal evolution of $\dot{M}$. We cannot resolve the evolution in the interior of the control volume. Because of angular momentum conservation most of the matter that falls in will assemble in a protostellar disc. There it is transported inwards by viscous and possibly gravitational torques (Pringle 1981; Papaloizou & Lin 1995; see also Jappsen & Klessen 2004 for the models discussed here). The latter will be provided by spiral density waves that develop when the disc becomes too massive, which happens when mass is loaded onto the disc faster than it is removed by viscous transport. Altogether, the disc will not prevent or delay material from accreting onto the protostar for long. It acts as a buffer and smoothes eventual accretion spikes.

For the mass range considered here feedback effects are too weak to halt or delay accretion (Wuchterl & Klessen 2001; Wuchterl & Tscharnuter 2003). With

typical disc sizes of the order of several hundred AU, the control volume therefore fully encloses both star and disc, and the measured core accretion rates are good estimates of the actual stellar accretion rates. Deviations may be expected only if the protostellar core forms a binary star, where the infalling mass must then be distributed over two stars, or if very high-angular momentum material is accreted, where a certain mass fraction may end up in a circumbinary disc and not accrete onto a star at all.

In the prestellar phase, i.e. before the central protostar forms, we determine the accretion history by computing the change of mass inside the control volume centered on the SPH particle that turns into a sink particle during the later evolution. Turbulent compression leads to mass growth, i.e. $\dot{M} > 0$, while expansion will result in mass loss and $\dot{M} < 0$. Appreciable mass growth, however, is only achieved when gravity takes over and the region goes into collapse.

5.3 Time-varying Mass Accretion Rates

We analyse the full mass growth history of all protostellar cores in our models and we find that mass accretion rates from gravoturbulent fragmentation are highly time-variable. Several examples of the accretion rate $\dot{M}$ are shown, plotted versus time (Fig. 5.1) and the ratio of accreted to final mass (Fig. 5.2), respectively. The maximum accretion rate is reached rather rapidly and is then followed by a somewhat slower decline. In some cases this decline is interrupted by one or more secondary peaks. As shown above, the maximum accretion rate is significantly higher than the constant rate predicted by the classical isothermal collapse model (plotted as dotted line in Fig. 5.1 and 5.2), but it falls below that value in later stages. Due to the dynamical interaction and competition between protostellar cores, the mass accretion rates of cores in a dense cluster are different from those of isolated cores. In the first stage a core accretes local gas from its immediate vicinity. Once the local reservoir is depleted, the core may accrete fresh gas streaming in from further away or by encounters with non-collapsed gas clumps (see discussion in Klessen & Burkert 2000). This results in secondary accretion peaks that are also visible in Fig. 5.2, where one would expect a single bump in the case of an isolated core. For example, the central graph of Fig. 5.2 clearly shows that this particular protostar accretes only about half of the final mass from its direct environment (first bump), while the rest comes from later accretion events.

The transition phase between Class 0 and Class 1 protostars is believed to take place when about half of the final mass has been accumulated (André et al. 2000). This time is indicated by the dashed line in Fig. 5.1. Typically it takes place during or at the end of the peak accretion phase. It determines the lifetime of Class 0 objects, which will be discussed below.

We define a mean accretion rate $\langle \dot{M} \rangle$ by averaging $\dot{M}$ in the mass range $0.1 \leq M/M_{\rm end} \leq 0.8$, with $M_{\rm end}$ being the final mass of the protostar. This phase typically lasts only a few 10^4 years. This is short compared to the full accretion history. The

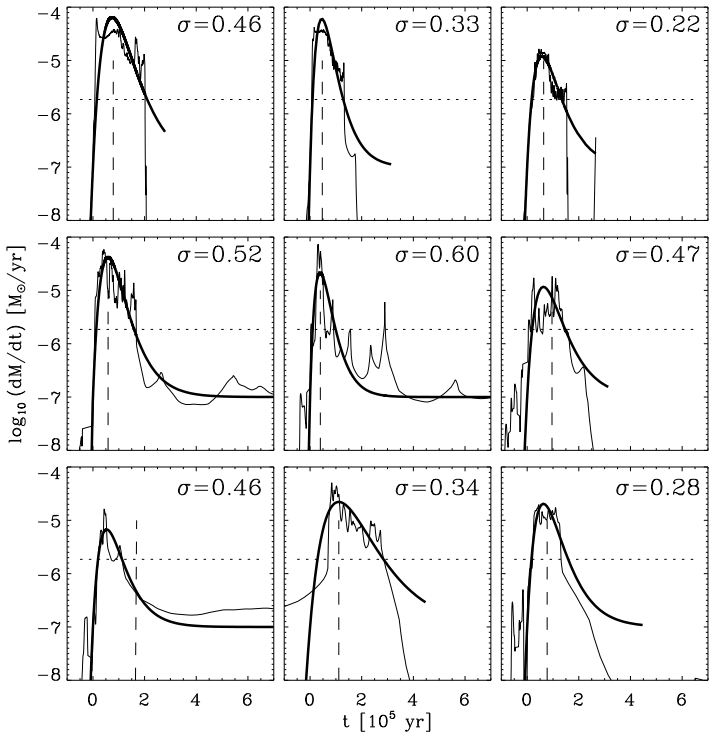

Figure 5.1: Mass accretion rates of nine randomly selected protostellar cores of three different models: $\dot{M}$ versus time for a Gaussian collapse (G2; upper row), a turbulent model driven on a large scale (M6k2a; middle row), and a turbulent model driven on a small scale (M6k8b; lower row). The thin line represents the actual simulation, the thick line the fit as described in the text. The deviation σ as given by Eq. (5.6) is indicated for each object. The dotted line shows the constant accretion rate that would be expected from the classical Shu (1977) scenario. The dashed line stands for the assumed transition from Class 0 to Class 1.

bulk of stellar material is therefore accumulated in the short time interval while the system is close to maximum accretion.

In Fig. 5.3, we plot the mean accretion rates versus final star mass $M_{\rm end}$ and versus time of core formation $t_{\rm form}$, respectively, for the same models as in Fig. 5.1. Not surprisingly, $\langle\dot{M}\rangle$ increases with increasing stellar mass, and decreases when the core forms later, although this second correlation is not as clear. In other words, more massive stars have higher mass accretion rates and start to form first. They can grow large, because on average they form in the high-density regions of the cluster centre where they are able to maintain relatively high accretion rates over a long time as more and more gas falls in from the cluster outskirts.

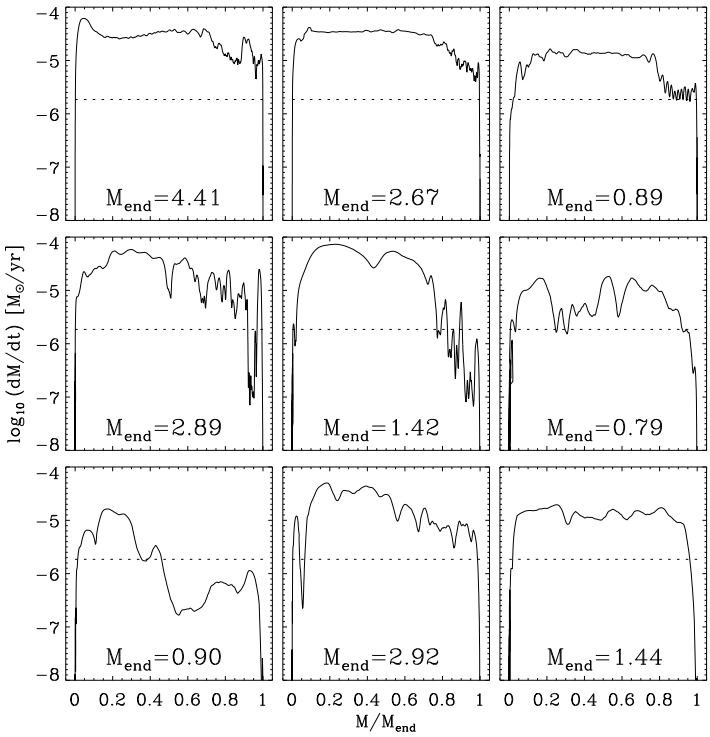

Figure 5.2: Mass accretion rates of nine randomly selected protostellar cores of three different models: The same protostellar cores as in Fig. 5.1 are plotted versus the ratio of accreted to final mass. The final masses (in $M_\odot$) are also given.

5.4 An Empirical Fit Formula for $\dot{M}$

One of our aims is to find a simple-to-use fit formula to approximate the accretion process. The protostellar mass growth history in our models can be fitted empirically in the lin-log diagram by the function

$$\log \dot{M}(t) = \log \dot{M}_0 \, \frac{\mathrm{e}}{\tau} \, t \, \mathrm{e}^{-t/\tau} \tag{5.5}$$

with time t and the fit parameters $\log \dot{M}_0$ and τ. This holds for the following conditions: We shift the ordinate by $\Delta \log \dot{M}/(\mathrm{M}_\odot\,\mathrm{yr}^{-1}) = +7$ and we consider accretion when $\log \dot{M} \geq -7$. The zero point of the timescale is determined once the accretion rate exceeds $\log \dot{M} = -7$. The fitted curves are plotted as thick lines in Fig. 5.1. Note that the ordinate displays the original values without the applied shift. If there are secondary accretion peaks, they are typically ignored and levelled out by the routine. The overall quality of the fit can be estimated by the standard deviation

$$\sigma = \sqrt{\frac{1}{n-1} \sum_{t=0}^{n} \left[\dot{M}_{\mathrm{fit}}(t) - \dot{M}(t) \right]^2} \tag{5.6}$$

Table 5.1: Parameters of the models

Model	n_* [a]	n_* [b]	σ_{mean} [c]	$\dot{M}_{\mathrm{mean}}$ [$10^5 \mathrm{M}_\odot \mathrm{yr}^{-1}$]			
		fitted		bin1	bin2	bin3	bin4
G1	56	31	0.49	1.18	1.30	1.70	2.93
G2	56	52	0.43	0.94	1.40	2.09	3.51
M01k2	95	91	0.43	0.77	1.76	3.04	–
M01k4	3	3	0.81	2.83	–	–	57.98
M01k8	3	3	0.47	–	1.37	13.25	59.16
M05k2	23	22	0.49	1.63	5.05	4.88	12.95
M05k4	48	48	0.39	1.31	2.49	2.56	6.30
M05k8	48	48	0.40	1.34	2.22	3.79	7.77
M2k2	68	62	0.41	0.86	1.38	2.54	4.32
M2k4	62	62	0.44	1.35	1.92	2.43	3.84
M2k8	42	40	0.42	0.87	1.29	1.72	3.38
M3k2	65	65	0.46	1.31	1.86	2.98	3.78
M3k4	37	35	0.55	1.01	1.13	1.15	1.86
M3k8	17	17	0.41	0.51	1.09	1.74	5.84
M6k2a	100	97	0.49	0.79	1.69	1.96	3.39
M6k4a	98	93	0.44	0.38	0.83	0.89	1.10
M6k2b	50	50	0.42	1.02	1.81	2.50	–
M6k4b	50	47	0.43	0.72	1.66	1.87	–
M6k8b	25	25	0.44	0.35	0.61	1.38	2.47
M6k2c	110	97	0.43	0.83	1.32	1.50	1.23
M6k4c	53	46	0.54	1.31	1.46	2.05	1.97
M6k8c	12	10	0.43	0.50	0.62	0.58	–
M10k2	150	146	0.44	1.08	2.62	2.09	–
M10k8	54	44	0.53	0.26	0.64	–	–

[a] total number of formed protostars
[b] number of protostars that can be fitted by Eq. (5.5)
[c] mean deviation of the fits, calculated from Eq. (5.6)

where $\dot{M}(t)$ is the actual value of $\dot{M}$ at the time t from our simulation, while $\dot{M}_{\mathrm{fit}}(t)$ denotes $\dot{M}$ calculated using Eq. (5.5) for the same time. The mean value of σ for each model is given in Col. 4 of Table 5.1. Prestellar cores where the fit routine fails or where $\sigma > 1$ are not taken into account in our subsequent analysis. This concerns a wide variety of cores; there is no correlation with the final mass or the time of formation. However, they represent only a small fraction of the total number of objects. The actual numbers of fitted cores are listed in Col. 3 of Table 5.1.

When interpreting the fit parameter $\log \dot{M}_0$, the applied shift has to be taken into account. Thus, $\log \dot{M}_{\mathrm{max}}^{\mathrm{fit}} = \log \dot{M}_0 - 7$ gives the real value of the peak accretion. This parameter is plotted for all protostellar cores and all models versus the respective final mass (Fig. 5.4). A correlation with M_{end} is obvious. We apply a

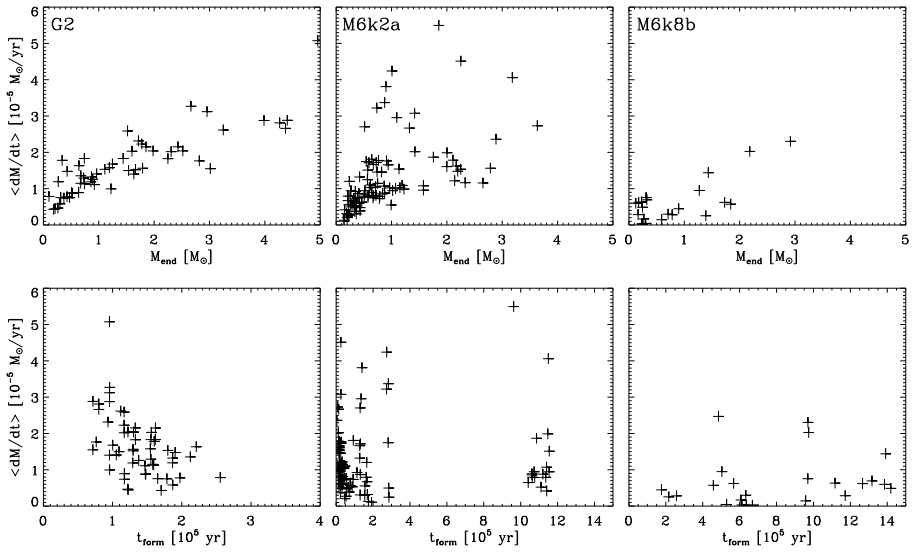

Figure 5.3: Mean accretion rates $\langle \dot{M} \rangle$ versus final mass (upper panel) and versus time of core formation (lower panel) for the same models as in Fig. 5.1. The zero point of the timescale corresponds to the time when gravity is "switched on". Note the different timescales on which the formation of the cluster takes place.

linear fit in the log-log diagram, which is indicated by the straight line. The fitted peak accretion rates show the same behaviour as the mean accretion rates $\langle \dot{M} \rangle$.

The parameter τ indicates the time of the maximum of the accretion curve. It is plotted for all protostellar cores in Fig. 5.5. In almost all models τ shows a correlation with the final mass. The parameter indicates how fast the gas falls in onto the core, therefore we expect it to be related to the local free-fall time and, thus, to the local density at the onset of collapse. It lies in the range $10^4 \lesssim \tau \lesssim 10^5$ yr, which is less than the global free-fall time $\overline{\tau}_{\rm ff}$. If we take an average value $\langle \tau \rangle \approx \overline{\tau}_{\rm ff}/3$, this suggests an initial overdensity of almost a factor of ten in the collapsing regions.

5.5 Class 0 Lifetimes and the Influence of the Turbulent Medium

We calculate the transition times from Class 0 to Class 1, assumed as described above. This gives the duration of the Class 0 phase for each protostar; the values are plotted versus the corresponding final masses in Fig. 5.6. The duration of the Class 0 phase increases with increasing final mass. Thus, a massive star is marked not only by a higher peak accretion rate but also by a longer time spent in Class 0 phase. A more sophisticated analysis of Class 0 lifetimes is presented in § 6.2.5.

The mean accretion rates $\langle \dot{M} \rangle$ of all individual protostellar cores of one model

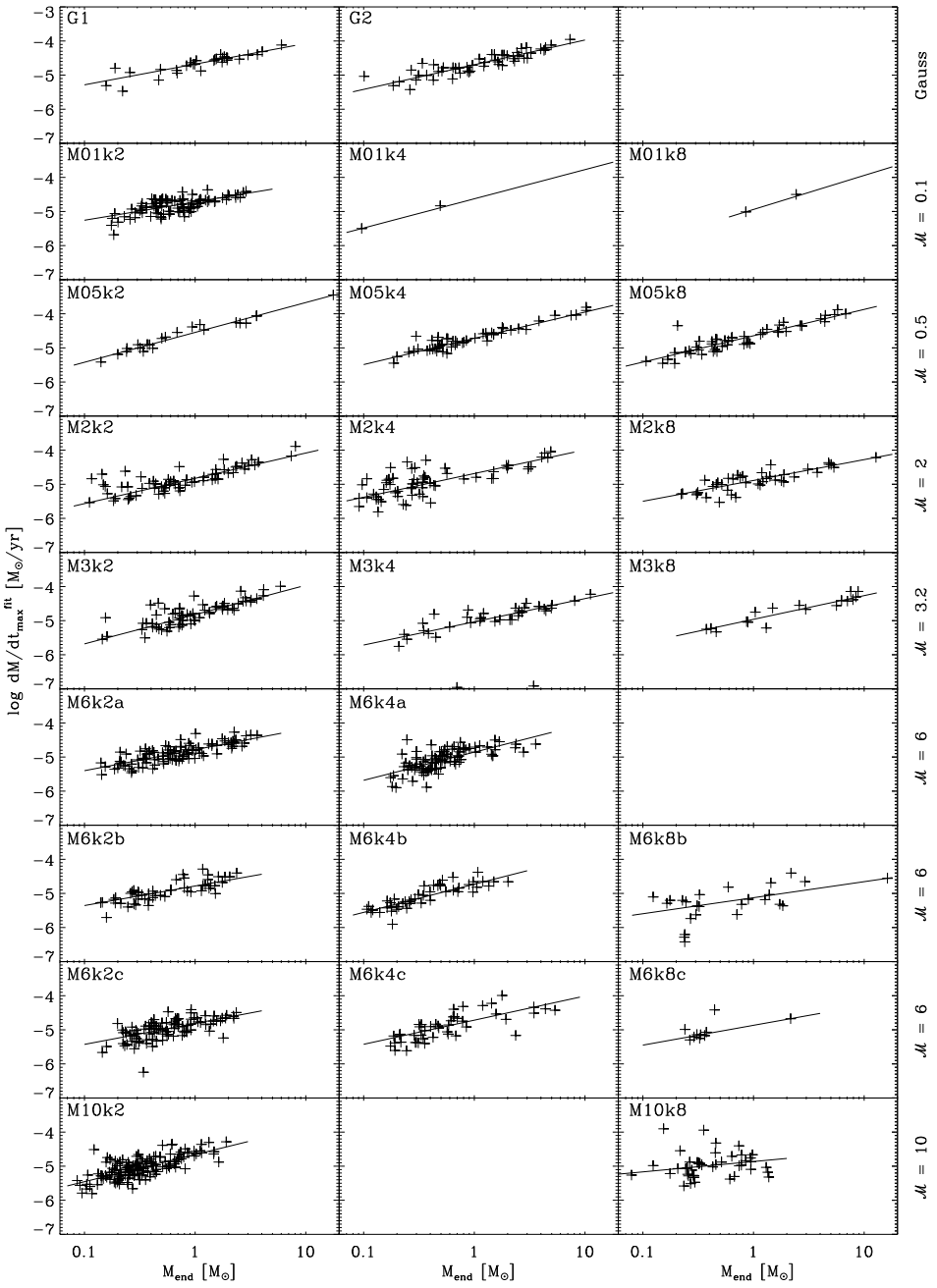

Figure 5.4: Peak accretion rates (log $\dot{M}_{\rm max}^{\rm fit}$) versus $M_{\rm end}$ for all our models, sorted by Mach number $\mathcal{M}$ (top to bottom) and wave number k (left to right). The straight line shows the applied linear fit.

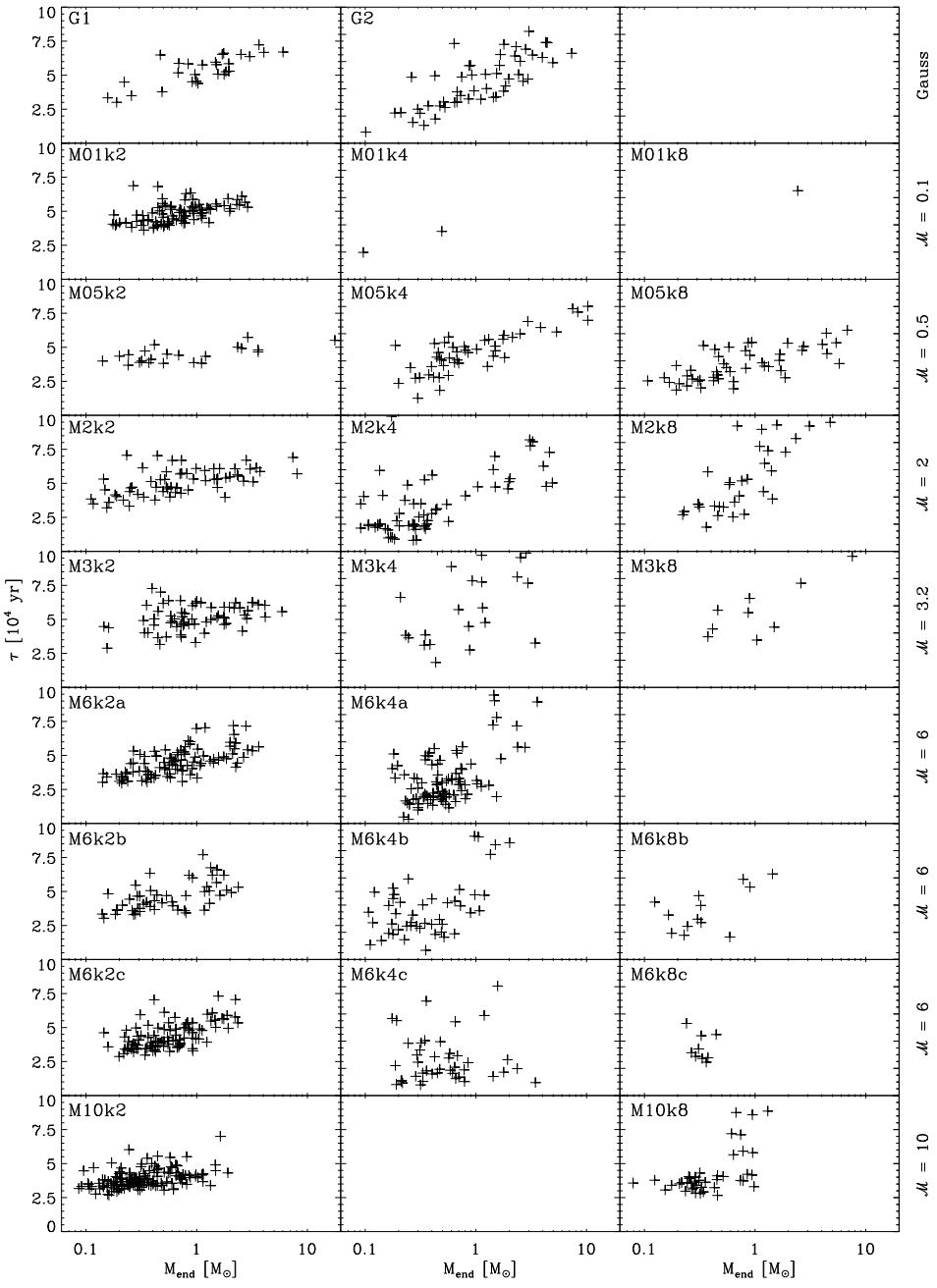

Figure 5.5: The time of maximum accretion τ for all models, arranged analogous to Fig. 5.4.

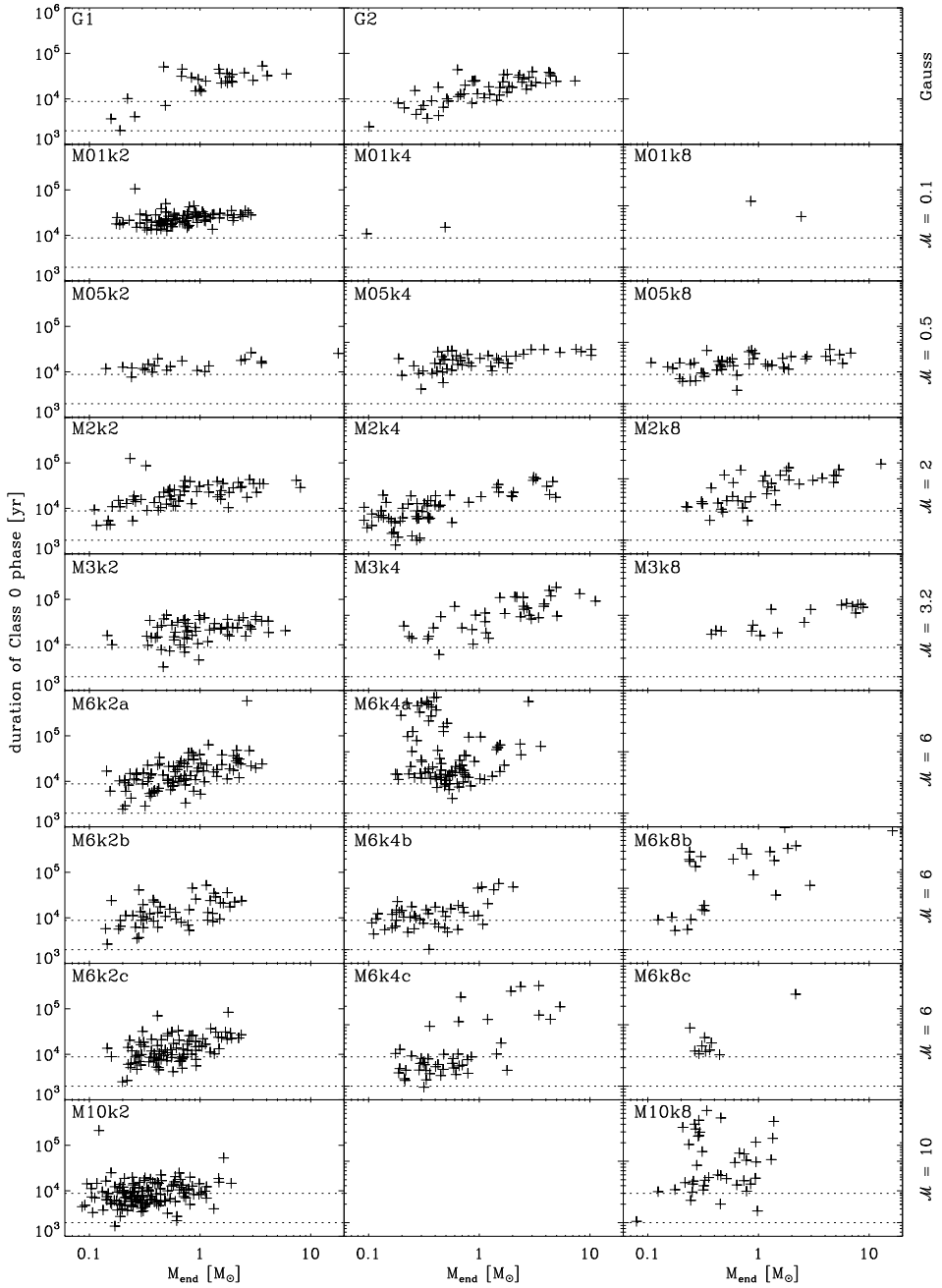

Figure 5.6: The assumed duration of Class 0 phase versus $M_{\rm end}$ for all models, arranged analogous to Fig. 5.4. The dotted lines confine the range of this parameter according to observations (André et al. 2000).

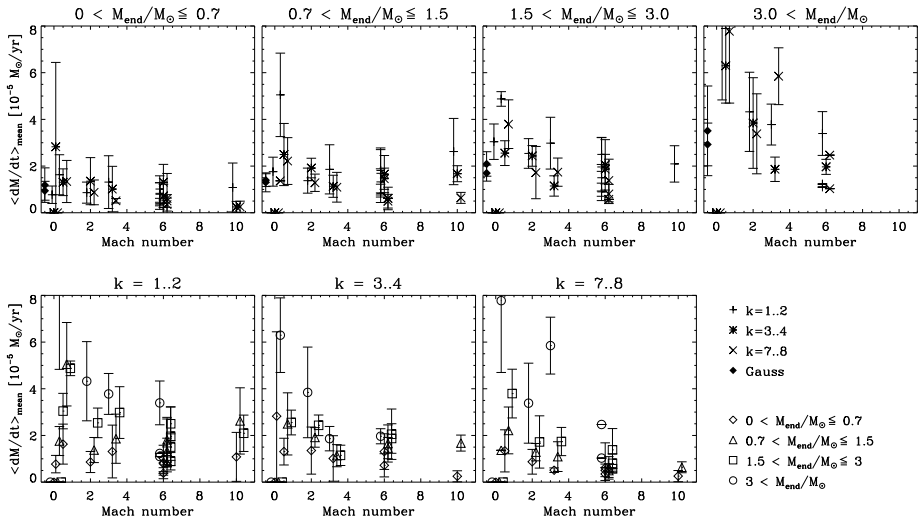

Figure 5.7: Averaged mean accretion rates $\langle \dot{M} \rangle_{\mathrm{mean}}$ of all models versus Mach number. For the sake of clarity the upper panel is split into mass bins, while the lower panel shows the same, separated according to the wave numbers.

are averaged in four mass bins: $0 < M_{\mathrm{end}}/\mathrm{M}_\odot \leq 0.7$ (bin1), $0.7 < M_{\mathrm{end}}/\mathrm{M}_\odot \leq 1.5$ (bin2), $1.5 < M_{\mathrm{end}}/\mathrm{M}_\odot \leq 3$ (bin3), and $M_{\mathrm{end}}/\mathrm{M}_\odot > 3$ (bin4). The values are given in Cols. 5 to 8 of Table 5.1. Figure 5.7 shows the relation of the averaged mean mass accretion rate $\langle \dot{M} \rangle_{\mathrm{mean}}$ to the Mach number for all models, split into mass bins and wave numbers, respectively. Three conclusions can be drawn from the figure: There is a trend that $\langle \dot{M} \rangle_{\mathrm{mean}}$ decreases with increasing Mach number. This means that the mean accretion rate is lower, when the rms velocity dispersion (i.e. the turbulent Mach number) of the medium is increased. The stronger support of the turbulent medium against gravitational collapse typically results in a lower mass accretion rate. Secondly, $\langle \dot{M} \rangle_{\mathrm{mean}}$ is higher for higher mass bins. This is consistent with the findings for the individual mean and maximum accretion rates ($\langle \dot{M} \rangle$ and $\dot{M}_{\mathrm{max}}^{\mathrm{fit}}$) discussed above. Finally, though, there is no correlation of $\langle \dot{M} \rangle_{\mathrm{mean}}$ with the wave number. Apparently the scale of the driving energy has no influence on the accretion rate.

5.6 Comparison to Other Models

In the standard theory of isolated star formation (Shu 1977), which takes a singular isothermal sphere as initial condition, the mass accretion rate is constant in time: $\dot{M} = 0.975\, c_{\mathrm{s}}^3/G$. Also the Larson-Penston solution (Larson 1969; Penston 1969), considering constant-density initial perturbations, gives a time-independent accretion rate, however, at a higher level of $47\, c_{\mathrm{s}}^3/G$. The first numerical collapse calculations were reported by Bodenheimer & Sweigart (1968), Larson (1969) and

Hunter (1977). Models with more realistic initial density profiles generally predict accretion rates that decline with time: The models of Hunter (1977; $\dot{M}_{\rm max} \approx 36\,c_{\rm s}^3/G$ from numerical integrations of isothermal collapses), Foster & Chevalier (1993; $\dot{M}_{\rm max} \approx 47\,c_{\rm s}^3/G$ from numerical hydrodynamic simulations), Tomisaka (1996; $\dot{M}_{\rm max} = (4-40)\,c_{\rm s}^3/G$ from numerical MHD models), Basu (1997; $\dot{M}_{\rm max} = 13\,c_{\rm s}^3/G$ from a semi-analytical model), Ogino et al. (1999; $\dot{M}_{\rm max} \approx (30-230)\,c_{\rm s}^3/G$ from numerical hydrodynamic simulations), Masunaga & Inutsuka (2000; radiation hydrodynamic numerical codes), Whitworth & Ward-Thompson (2001) and Motoyama & Yoshida (2003; $\dot{M}_{\rm max} \gtrsim 42\,c_{\rm s}^3/G$) predict mass accretion rates that peak shortly after the formation of the protostar and decrease with time. This shows better agreement with observational data than constant accretion rates (see § 5.7). Our results display the same behaviour and our values of $\dot{M}_{\rm max} \approx (3-50)\,c_{\rm s}^3/G$ coincide quite well with those findings. In contrast, some models yield mass accretion rates that increase with time (McLaughlin & Pudritz 1997; Bonnell et al. 2001a; Behrend & Maeder 2001).

Theoretical models of star formation usually are scale-free. Thus, the results strongly depend on the adopted physical scaling, e.g. the choice of the initial density or temperature. The comparison of numerical values of accretion rates therefore requires some care. Again, in most cases the maximum accretion rates scale approximately as a few times $M_{\rm J}/\tau_{\rm ff}$.

Whitworth & Ward-Thompson (2001) presented an analytical model for protostellar collapse using a Plummer-like density profile as initial condition. They successfully modelled the prestellar core L1544 in good agreement with observations. Their $\dot{M}_{\rm max} \approx 8.1 \times 10^{-5}$ M$_\odot$ yr^{-1} corresponds quite well to our Gaussian collapse cases for the same stellar mass (G1, G2). However, the accretion history of the collapsing Plummer sphere cannot be matched with our fit formula (5.5). The increase is steeper, while the decrease is slower compared to any of our models. The slow decline might be due to the fact that Whitworth & Ward-Thompson (2001) use a non-truncated, infinite density profile, while our models have finite sizes. A similar model was used by Motoyama & Yoshida (2003) who examined the hypothesis that very high mass accretion rates exceeding 10^{-4} M$_\odot$ yr^{-1} require external triggering, as inferred from some observations. They find that the maximum accretion rate is proportional to the momentum given to the cloud core in their perturbed collapse model. A momentum of $\gtrsim 0.1$ M$_\odot$ km s^{-1} causes an accretion rate of $\gtrsim 10^{-4}$ M$_\odot$ yr^{-1}.

Smith (1998, 2000, 2002) presented a formula for the mass accretion rate with a sharp exponential rise and a power law decrease in time. This model provides an early peak in which $\dot{M} \approx 10^{-4}$ M$_\odot$ yr^{-1} for 10^4 years, and eventually becoming $\dot{M} \approx 10^{-7}$ M$_\odot$ yr^{-1} for 10^6 years. However, his formula (Eq. 6 in Smith 2000) applies to our models only when choosing parameters completely different to those suggested, otherwise his accretion curve has a more rapid increase but a slower decline than our models.

Bonnell et al. (2001a) analysed competitive accretion in embedded stellar clusters by means of SPH simulations. They find that accretion in a cluster is highly

non-uniform and that the accretion rate is higher for stars near the cluster centre. We do not see this in our results, likely because the protostars in our model are at different stages of evolution at a certain time, so this effect, if existent, is covered by the strongly time-dependent variation in the accretion rate. Also the evolution of $\dot{M}$ with time in their models differs from our results: The mean accretion rate reported by Bonnell et al. (2001a), determined from all protostars in the cluster, increases with time until near the end of the simulation when the gas is significantly depleted. The difference is probably caused by the different assumptions (e.g. lack of turbulence, clustered potential). Indeed, the recent models of Bonnell et al. (2003) produce nearly constant accretion rates onto the most massive stars in the cluster. The difference might be due to the fact that the accretion rates in the latter models are determined by the accretion onto the cluster from outside, while in the models of Bonnell et al. (2001a) all the mass was already in the cluster.

Reid et al. (2002) used a logatropic equation of state as the basis for their hydrodynamical simulations of isolated star formation. Their accretion rate depends on the size of the core. It increases cubically and reaches maximum when the expansion wave leaves the core, then it falls steadily. With the adopted scaling, $\dot{M}_{\rm max}$ is one to two orders of magnitude smaller than in our models. Consequently the whole accretion process lasts much longer, several 10^6 years, which is in contradiction to estimates of rapid star formation (Elmegreen 2000; Hartmann et al. 2001; Hartmann 2003; Mac Low & Klessen 2004).

The work of Reid et al. (2002) is extended by Sigalotti et al. (2002) performing calculations of spherical gravitational collapse and accretion of nonsingular logatropes. In all their models the accretion rate rises steeply after the formation of the core, reaching its maximum when the protostar has accreted ∼40% of its final mass, followed by a monotonic decrease. Peak values are $\sim 5-6\times10^{-5}$ $\mathrm{M_\odot\,yr^{-1}}$ for cores close to the critical mass and one to two orders of magnitude lower for subcritical cores. At the transition from Class 0 to 1 the accretion rate is $\sim 0.07-5.5\times10^{-5}$ $\mathrm{M_\odot\,yr^{-1}}$, at the Class 1/2 border it is $\sim 0.02-1.4\times10^{-6}$ $\mathrm{M_\odot\,yr^{-1}}$. Class 0 lifetimes are predicted as $\sim 0.1-1.6\times10^6$ yr and Class 1 lifetimes as $\sim 0.4-5\times10^6$ yr. For Class 0 objects this is about an order of magnitude larger than estimated from observations (André et al. 2000) and the same objections as to the models of Reid et al. (2002) have to be raised.

Wuchterl & Tscharnuter (2003) find, from models based on radiation hydrodynamics, time-varying accretion rates of a few 10^{-6} $\mathrm{M_\odot\,yr^{-1}}$ for the phase $< 0.8\,M_{\rm end}$, which is about an order of magnitude lower than our values, especially for Gaussian collapse or large-scale turbulence. The reason may be that protostellar cores in our models form by external compression before gravity takes over. This results in enhanced accretion rates relative to cores that begin contraction close to hydrostatic equilibrium.

Hennebelle et al. (2003) performed numerical simulations where the collapse is triggered by a steady increase in the external pressure. $\dot{M}_{\rm max}$ is reached immediately after the formation of the central protostar (i.e. during the Class 0 phase), followed by a steady decrease of $\dot{M}$ to the Class 1 phase. The more rapid and

the more prolonged the increase in external pressure, the higher is $\dot{M}_{\rm max}$, ranging from 6.5×10^{-6} $\mathrm{M_\odot\,yr^{-1}}$ to 2.6×10^{-5} $\mathrm{M_\odot\,yr^{-1}}$, corresponding to $\sim (4-16)\, c_{\rm s}^3/G$. The qualitative behaviour of the accretion process does not differ much from our models, but the peak accretion rates are slightly smaller than ours except in their models with the most rapid compression.

Shu et al. (2004) discuss numerical simulations for a singular isothermal sphere with a uniform magnetic field. The maximum accretion rate of $\dot{M} \approx 1.1\ c_{\rm s}^3/G$ is close to the unmagnetised SIS value of 0.975 (Shu 1977), but unlike the latter it declines steadily.

Table 5.2 summarises the mass accretion rates from all the models discussed.

5.7 Comparison to Observations

It is very difficult to measure mass accretion rates directly from observations (e.g. from inverse P Cygni profiles), instead they often have to be inferred indirectly based on the SEDs of protostars or using outflow characteristics (Hartigan et al. 1995; Bontemps et al. 1996). The correlation between accretion rates and outflow strength, however, is still subject of strong debate (Wolf-Chase et al. 2003). For Class 0 objects typical mass accretion rates are estimated in the range $10^{-5} \lesssim \dot{M}/\mathrm{M_\odot\,yr^{-1}} \lesssim 10^{-4}$ (Hartmann 1998; Narayanan et al. 1998; André et al. 1999; Ceccarelli et al. 2000; Jayawardhana et al. 2001; Di Francesco et al. 2001; Maret et al. 2002; Beuther et al. 2002a,b). The growth rate of Class 1 objects is believed to be about an order of magnitude smaller (Henriksen et al. 1997; André et al. 2000), with observational values between $\sim 10^{-7}$ and $\sim 5 \times 10^{-6}$ $\mathrm{M_\odot\,yr^{-1}}$ (Brown & Chandler 1999; Greene & Lada 2002; Boogert et al. 2002; Yokogawa et al. 2003; Young et al. 2003).

Bontemps et al. (1996) studied the outflow activities in a sample of 45 low-mass embedded young stellar objects. They estimate that the observed decline of CO outflow momentum fluxes with time results from a decrease of the mass accretion rate from $\sim 10^{-5}$ $\mathrm{M_\odot\,yr^{-1}}$ for the youngest Class 0 protostars to $\sim 10^{-7}$ $\mathrm{M_\odot\,yr^{-1}}$ for the most evolved Class 1 objects. Furthermore, they propose a simple exponential dependency of the accretion rate with time: $\dot{M} = (M_{\rm env}^0/\tau)\mathrm{e}^{-t/\tau}$ with initial mass of the dense clump $M_{\rm env}^0$ and a characteristic time $\tau \approx 9 \times 10^4$ yr. This is comparable to our Eq. (5.5). A similar exponential equation is also used by Myers et al. (1998), while Henriksen et al. (1997) describe the accretion rate by an equation that asymptotically approaches a power-law dependence at late times.

Brown & Chandler (1999), who determined an upper limit of $\dot{M} \lesssim (2-4) \times 10^{-7}$ $\mathrm{M_\odot\,yr^{-1}}$ for two Class 1 protostars in Taurus, also conclude that the accretion rate is not constant in time and likely is much higher in the early phase. On the other hand, Hirano et al. (2003) observed a dozen of deeply embedded young stellar objects of both Class 0 and 1 and derived the same mass accretion rates of $(1-5) \times 10^{-6}\,\mathrm{M_\odot\,yr^{-1}}$ for all of them. Unlike other authors, they argue that there is no significant difference in $\dot{M}$ between Class 0 and Class 1 sources. White &

Hillenbrand (2004) infer mass accretion rates of Class 1 protostars that are indistinguishable from Class 2 objects. They find a median accretion rate of Class 1 and 2 objects of only $4\times10^{-8}\,\mathrm{M_\odot\,yr^{-1}}$, within a large range of two orders of magnitude.

Pre-main sequence stars (Class 2 and 3) have accretion rates still lower than Class 1 (note, however, the contradicting findings of White & Hillenbrand 2004 discussed above), they are estimated to be in the range $\lesssim 10^{-7}\,\mathrm{M_\odot\,yr^{-1}}$ (Muzerolle et al. 2003; Calvet et al. 2004; Furlan et al. 2005). Muzerolle et al. (2003) present a study of accretion in a sample of 45 young, low-mass objects in a variety of star-forming regions and young associations, most of them classical T Tauri stars (i.e. Class 2). They estimate accretion rates in the range $10^{-12}\,\mathrm{M_\odot\,yr^{-1}} < \dot{M} < 10^{-9}\,\mathrm{M_\odot\,yr^{-1}}$. They also note a clear trend of decreasing accretion rate with stellar mass, with mean accretion rates declining by 3 to 4 orders of magnitude over 1 – 0.05 $\mathrm{M_\odot}$. For intermediate-mass T Tauri stars (1.5 – 4 $\mathrm{M_\odot}$), Calvet et al. (2004) determine accretion rates between 4×10^{-9} and $3\times10^{-7}\,\mathrm{M_\odot\,yr^{-1}}$. In consistency with Muzerolle et al. (2003) they find a clear correlation between mass accretion rate and stellar mass. Furlan et al. (2005) investigated a sample of CTTSs in the Taurus star-forming region. From the literature they compile mass accretion rates in the range $3.5\times10^{-10}\,\mathrm{M_\odot\,yr^{-1}} < \dot{M} < 6.8\times10^{-8}\,\mathrm{M_\odot\,yr^{-1}}$.

The values from observations given above are summarised in Table 5.3. They correspond to the accretion rates derived for the models of gravoturbulent star formation discussed here. They also decrease from 10^{-5} to 10^{-4} $\mathrm{M_\odot\,yr^{-1}}$ during the Class 0 phase to less than 10^{-7} $\mathrm{M_\odot\,yr^{-1}}$ in later stages. However, the supposed transition between Class 0 and Class 1 still takes place during the peak accretion phase. The accretion rates in our models typically do not decline significantly until about 80% of the final mass has been accreted (Fig. 5.1). This is unlike e.g. the model of Reid et al. (2002), where $\dot{M}$ begins to fall off when about half of the mass of the core has been accreted. Given the uncertainties of the mass estimate for the Class 0/1 transition we do not consider this a large discrepancy.

According to observations, Class 0 objects have an estimated lifetime of $\sim (1-3)\times10^4$ yr (André et al. 2000). In our models this parameter is widely spread, ranging from $\sim 10^4$ to $> 10^5$ yr, but for a 1 $\mathrm{M_\odot}$ star it lies roughly in the range deduced from observations (see Fig. 5.6). A more sophisticated analysis of Class 0 lifetimes is presented in § 6.2.5.

5.8 Summary

We have studied protostellar mass accretion rates from numerical models of star formation based on gravoturbulent fragmentation. Twenty-four models covering a wide range of environmental conditions from low to high turbulent velocities and different driving scales have been investigated. Our main results may be summarised as follows:

1. An order-of-magnitude estimate for mass accretion rates resulting from gravoturbulent fragmentation is given by $\dot{M} \approx M_\mathrm{J}/\tau_\mathrm{ff}$ with M_J being the mean

thermal Jeans mass and $\tau_{\rm ff}$ the corresponding free-fall time.

2. However, protostellar mass accretion is a highly time-variant process. It can be approximated by the empirical function $\log \dot{M}(t) = \log \dot{M}_0 \, (\mathrm{e}/\tau) \, t \, \mathrm{e}^{-t/\tau}$. The peak accretion rate is reached during the Class 0 stage, shortly after the formation of the core; its value ranges between about 5×10^{-6} and 10^{-4} $\mathrm{M}_\odot \, \mathrm{yr}^{-1}$. The maximum accretion rate is approximately one order of magnitude higher than the constant rate predicted by the collapse of a classical singular isothermal sphere.

3. Around the peak accretion phase the mass accretion rates are roughly constant. The mean accretion rates increase with increasing final mass. More massive stars have higher mass accretion rates and tend to form first.

4. The same applies to the fitted peak accretion rates, which are also proportional to the final stellar mass.

5. There is a similar correlation between the duration of Class 0 phase (assuming that half of the final mass is accreted in this phase) and the final mass.

6. $\langle \dot{M} \rangle_{\rm mean}$ decreases with increasing Mach number of the turbulent environment, but is not correlated with the driving wave number.

Our results agree well with many other models treating the time evolution of the mass accretion process and the value of the peak accretion rate. In particular, the accretion rates from our models show an exponential decline, as also proposed by Bontemps et al. (1996), Myers et al. (1998) and Smith (1998, 2000). They also match observational findings like the supposed decline of the mass accretion rate from the Class 0 to Class 1 phase. We conclude that a theory of star formation based on gravoturbulent fragmentation of molecular clouds is an adequate approach to describe stellar birth in the Milky Way.

Table 5.2: Protostellar mass accretion rates from models

Reference	Form of accretion curve	$\dot{M}_{\rm max}$ $[c_{\rm s}^3/G]$	$\dot{M}_{\rm max}$ $[10^{-5}\ {\rm M}_\odot {\rm yr}^{-1}]$
Shu 1977	constant	0.975	0.16
Larson 1969/Penston 1969	constant	47	8.9
Hunter 1977	steady decrease	36	5.9
Foster & Chevalier 1993	peak, sharp decrease	47	7.6
Tomisaka 1996	exponential decline	40	6.5
Basu 1997	declining	13	2.5
McLaughlin & Pudritz 1997	increasing with time		
Ogino 1999	declining	30 - 230	5 - 37
Smith 1998, 2000, 2002	sharp exp. rise, power-law decline		3.2
Masunaga & Inutsuka 2000	declining		1.3
Whitworth & Ward-Thompson 2001	sharp increase, exponential decline		8
Bonnell et al. 2001a	increases with time		
Reid et al. 2002	sharp increase, slower decline		0.1 - 0.3
Sigalotti et al. 2002	sharp increase, slower decline		0.1 - 5
Wuchterl & Tscharnuter 2003	time-varying		$\gtrsim 0.1$
Motoyama & Yoshida 2003	sharp increase, exponential decline		$\gtrsim 10$
Hennebelle et al. 2003	increase, slower decline		0.65 - 2.6
Shu et al. 2004	steady decline	1.1	
this work	sharp peak, exponential decline	3 - 50	0.5 - 10

Table 5.3: Protostellar mass accretion rates from observations

Object	Class	Method	$\dot{M}$ [$M_\odot yr^{-1}$]	M_* [$M_\odot$]	Reference
IRc2		IR spectrum	$6 - 15 \times 10^{-3}$	10 - 25	Morino et al. 1998
VLA 1623	0		$\gtrsim 10^{-4}$		Jayawardhana et al. 2001
NGC 1333 IRAS 4A	0	H_2CO line profiles	1.1×10^{-4}	0.71	Di Francesco et al. 2001
NGC 1333 IRAS 4	0	FIR water emission lines	5×10^{-5}	0.5	Maret et al. 2002
NGC 1333 IRAS 4B	0	H_2CO line profiles	3.7×10^{-5}	0.23	Di Francesco et al. 2001
IRAS 16293-2422		mm Cont., (J=5-4), (J=2-1) trans.	5×10^{-6}	0.24	Walker et al. 1986
IRAS 16293-2422		CS (J=7-6), (J=5-4), HCO^+ (J=4-3)	2.9×10^{-5}	0.27	Narayanan et al. 1998
IRAS 16293-2422		OI, H_2O, SiO emission	3.5×10^{-5}	0.8	Ceccarelli et al. 2000
IRAM 04191+1522	0	CO outflow	$4 - 10 \times 10^{-6}$	0.05	André et al. 1999
IRAM 04191+1522	0	mm spectroscopy	3×10^{-6}	0.05	Belloche et al. 2002
B1-bN, B1-bS	0?		$0.4 - 5 \times 10^{-5}$	1.6 - 1.8	Hirano et al. 1999
var. YSOs in Tau, Oph	0	$C^{18}O$ emission	$1 - 5 \times 10^{-6}$		Hirano et al. 2003
var. YSOs in Tau, Oph	I	$C^{18}O$ emission	$1 - 5 \times 10^{-6}$		Hirano et al. 2003
YLW 15	I	NIR SED	1.6×10^{-6}	0.5	Greene & Lada 2002
L1489 IRS	I	IR spectrum	10^{-6}		Boogert et al. 2002
TMC1	I	^{13}CO, $C^{18}O$ emission	$\lesssim 2 - 4 \times 10^{-7}$	0.2 - 0.4	Brown & Chandler 1999
TMC1A	I	^{13}CO, $C^{18}O$ emission	$\lesssim 2 - 4 \times 10^{-7}$	0.35 - 0.7	Brown & Chandler 1999
Haro 6-5B	I	$^{13}CO(J=1–0)$ emission	$0.93 - 6.2 \times 10^{-7}$	0.22	Yokogawa et al. 2003
IRAS 00338+6312	FU Ori	$H^{13}CO^+$ (J=1-0), $C^{18}O$ (J=1-0)	5.6×10^{-5}	2	Umemoto et al. 1999
var. CTTSs in Taurus	II	var. (compiled from the literature)	$0.04 - 6.8 \times 10^{-8}$		Furlan et al. 2005

Chapter 6

Evolutionary Tracks of Class 0 Protostars*

As discussed in the previous chapter, observational protostellar mass accretion rates are usually not measured directly, but have to be inferred by indirect methods, resulting in large uncertainties. So a direct comparison of the mass accretion rates obtained from the simulations to those from observations is not reasonable. Hence, it is desirable to convert the mass accretion rates from the simulations to easier observable quantities. The main three are the bolometric temperature[1] and luminosity, $T_{\rm bol}$ and $L_{\rm bol}$, and the envelope mass, $M_{\rm env}$.

Several such conversion schemes have been developed. Evolutionary models were first discussed by Bontemps et al. (1996) and Saraceno et al. (1996). Along these lines, André et al. (2000) took an exponential decline in both envelope mass and accretion rate to predict $L_{\rm bol}$-$M_{\rm env}$ tracks. An analytical scheme was presented by Myers et al. (1998). They assumed a mass infall rate matching the Shu (1977) solution at early times and then displaying an exponential fall off with time. The core which supplies the mass also provides the obscuration, thus fixing evolutionary tracks on a $T_{\rm bol}$-$L_{\rm bol}$ diagram. Based on this work, Smith (1998, 2000, 2002) presented an evolutionary scheme but adopted alternative analytical forms for the mass accretion (exponential increase and power law decrease) which resemble the results obtained by Whitworth & Ward-Thompson (2001) or this work. This evolutionary model, founded on mass transfer between the envelope, disc, protostar and jets, has provided successful interpretations for various sets of observational data ($T_{\rm bol}$, $L_{\rm bol}$, $M_{\rm env}$, outflow luminosity) of Class 0 and Class 1 objects (e.g. Davis et al. 1998; Yu et al. 2000; Stanke 2000; Froebrich et al. 2003). Here, we adopt the Smith (1998, 2000, 2002) scheme but replace the analytical accretion rates with those derived numerically.

*This chapter is based on a collaboration led by Dirk Froebrich, published as Froebrich, D., Schmeja, S., Smith, M. D., & Klessen, R. S., 2006, MNRAS, 368, 435

[1]The bolometric temperature, introduced by Myers & Ladd (1993), is the temperature of a blackbody having the same mean frequency as the observed continuum spectrum.

The 'recipe' how to achieve the comparison can be summarised as follows: (1) Define the parameters of the evolutionary scheme from observations and vary them within a reasonable range; (2) Feed the mass accretion rates from the numerical simulations into the evolutionary scheme; (3) calculate the evolutionary tracks; and (4) compare the resulting tracks with the distribution of the observational data by a three-dimensional Kolmogorov-Smirnov test.

6.1 Observations and Models

6.1.1 Observational Data

We require a statistically significant observational sample of protostars with accurate individual properties. The latter demands a uniform observational coverage of the entire SED from the NIR to the millimetre range. Several samples of Class 0 sources have been published (e.g. Chen et al. 1995; André et al. 2000; Shirley et al. 2000; Motte & André 2001). The latest study, which combines all previous ones and computes the object properties uniformly from all published data, is presented by Froebrich (2005). There, a list of 95 confirmed or candidate objects was compiled. Fifty of these sources possess sufficient observational data to be classified as Class 0 or Class 0/1 objects and allow us to determine the three source properties $T_{\rm bol}$, $L_{\rm bol}$, and $M_{\rm env}$ accurately. To ensure a reliable comparison of models and observations, we apply the following restrictions to this sample:

(1) We omit sources that have distances larger than 500 pc. This reduces the bias towards higher mass objects.

(2) All objects in Taurus are underluminous compared to the other sources, considering $T_{\rm bol}$ and $M_{\rm env}$. Note that this does not only mean a low luminosity of these objects, but rather a low luminosity combined with high envelope mass. The three very low luminosity objects in our sample (see Fig. 6.1) combine low luminosity ($1\,{\rm L}_\odot$) with low envelope mass ($0.2\,{\rm M}_\odot$) and might form (very) low-mass stars. In total, 25% of the Class 0 objects in the sample are underluminous. We exclude them for the comparison between the models and observations (but see the discussion in Sect. 6.2.6).

(3) A histogram of the number of sources in a certain $T_{\rm bol}$-bin shows that the observational sample is very incomplete at high bolometric temperatures. Hence the comparison of observations and models is restricted to $T_{\rm bol} < 80\,{\rm K}$.

These selections leave us with a sample of 27 Class 0 sources. This sample consists mostly of objects in Perseus, Orion and Serpens.

6.1.2 Adaptation of the Models

The mass accretion rates of the gravoturbulent models (hereafter gt-models) discussed in the previous chapter will be used as an input for the evolutionary scheme. Small number statistics will always be a major concern when comparing models

and observations of Class 0 objects. In order not to introduce further uncertainties from the model side, we restricted our analysis to those gt-models that possess more than 37 stars and have a numerical resolution of at least 2×10^5 particles. This leaves 16 out of the 24 sets of accretion rates listed in Table 5.1 for further analysis.

The timescale over which accretion is smoothed by the disc can be approximated by the viscous timescale

$$t_\mathrm{v} \approx \alpha_\mathrm{v}^{-1}(R/H)^2 t_\Phi \tag{6.1}$$

(Pringle 1981), including the viscosity parameter α_v, the disc radius R, the disc scale height H, and the rotational period $t_\Phi = \Omega^{-1}$. Using typical values of $\alpha_\mathrm{v} = 0.01$, $R/H = 10$ and $t_\Phi = 1\,\mathrm{yr}$, this yields a rough estimate of $t_\mathrm{v} \approx 10^4$ yrs for the viscous timescale at a radius of 1 AU. A large fraction of mass will lie external to this radius, leading to a larger t_v, but this will be compensated for by stronger gravitational torques, which can lead to significantly larger values of the effective viscosity in the disc (see e.g. Laughlin & Różyczka 1996). Since we cannot model the detailed behaviour inside the disc, we take 10^4 yrs as a rough measure for the smoothing timescale. This value is used to smooth the individual mass accretion rates from the gt-models. Our results do not significantly depend on the smoothing scale that we apply. Adopting viscous timescales of 5000 or 15 000 yrs yields very similar results.

There are further smoothing effects and time-shifts, e.g. the luminosity generated in the centre typically escapes a Class 0 envelope in about 300 yrs (as determined by a random walk model). Hence, this time lag is neglected in comparison to the disc viscosity timescale. The viscosity of the disc has additionally the effect that material transported from the envelope onto the disc needs some time before it gets accreted onto the star and the accretion luminosity is generated. Hence, the observed envelope masses and luminosities do not represent the same time in the evolution. The observed luminosity corresponds to that of an envelope mass which was present about a viscosity timescale earlier. However, since this effect does not become significant until the disc is formed, it can be neglected in the very early stages of the evolution. In later stages, the evolution along the T_bol-L_bol track is slower and the luminosity only slightly changes within one viscosity timescale. In particular the change is smaller than typical errors of the measurements. Hence, we also neglect this effect in our calculations.

A small fraction of model protostars become highly accelerated (e.g. by ejection from a multiple system). Due to the adopted periodic boundary conditions in our calculations, these objects cross the computational domain many times while continuing to accrete. In reality, however, these protostars would have quickly left the high-density gas of the star-forming region and would not be able to gain more mass. We therefore consider accretion to stop after the object has crossed the computational box more than ten times.

The radius of a sink particle is fixed at 280 AU, the physics (e.g. exact accretion,

radiation) inside this volume cannot be resolved. Therefore, an evolutionary model describing the processes inside the sink particle is required.

6.1.3 Evolutionary Scheme

The evolutionary model (hereafter e-model) is used to transform the mass accretion rates from the gt-models into observable quantities such as $T_{\rm bol}$, $L_{\rm bol}$, and $M_{\rm env}$. It is based on mass and energy transfer between the different components of the forming star (protostar, disc, envelope, jet). Mass conservation is the main principle in this analytical model. Each simulated accretion rate from the gt-models is taken as the mass inflow rate from a spherical envelope onto the inner disc/protostar/jet system. All the mass flows through the disc but only a fraction accretes onto the protostar. The rest is ejected within two jets. The ejected mass fraction is small but not negligible in the Class 0 stage.

Many parameters and constants are needed to fully describe the envelope and predict the radiative properties (Myers et al. 1998; Smith 1998, 2000, 2002; Froebrich et al. 2006). See Smith (2000) and Appendix B of Froebrich et al. (2006) for a detailed description of the parameters and equations of the evolutionary model used in this work. We carefully chose a subset of parameters which we kept variable: (1) $T_{\rm env}$; The temperature of the outer envelope, out to which the envelope mass is determined. (2) $frac_{\rm env}$; The total mass that will be accreted onto the protostar is distributed in the envelope and the disc. A constant ratio of these two masses is assumed and $frac_{\rm env}$ represents the fraction of the total mass that is in the envelope. (3) $M_{\rm extra}$; This is the supplementary mass fraction in the immediate surroundings which does not actually fall towards the star, to be accreted or jetted away, but is removed directly from the core probably through a feedback process. (4/5) t_0, α; These two parameters describe the dispersion of the extra mass in the envelope. (6) $R_{\rm in}$; The inner radius of the envelope. (7) $M_{\rm eff}$; The maximum percentage of the infalling envelope mass which is ejected into the outflow. (8) p; The power-law index of the density distribution in the envelope, assumed constant in time. (9) κ; The opacity of the envelope material at 12 μm. In Table 6.1 we list the parameter ranges which were tested.

We now only need to impose a mass accretion rate from the gt-models for the evolution of a model protostar to be fully determined. Using all individual accretion rates in a gt-model allows us to build up a $T_{\rm bol}$-$L_{\rm bol}$-$M_{\rm env}$ distribution which can be compared to the observational dataset.

Some of our free parameters can be, and have been, observed for individual objects. This includes for example the power-law index of the density distribution in the envelope (e.g. Chandler & Richer 2000; Motte & André 2001) or $frac_{\rm env}$ (e.g. Looney et al. 2003). We chose to keep those parameters variable in order to test our method, since we expected to obtain values within the observational constraints.

Table 6.1: Variable parameters from the e-model of Smith (1998, 2000, 2002), together with the range they were varied in and the original value. The last two columns provide the overall range found to lead to the best agreement.

Parameter	varied		org. value	best	
	from	to		from	to
$T_{\rm env}$ [K]	10	30	24	15	19
$frac_{\rm env}$ [%]	75	100	87	86	96
$M_{\rm extra}$	0	5	2	1.0	2.4
t_0 [10^3 yrs]	1	100	30	30	80
α	0.5	4.0	1.75	1.4	3.2
$R_{\rm in}$ [AU]	5	100	30	35	80
$M_{\rm eff}$ [%]	0	50	30	36	44
p	1.4	2.0	1.5	1.55	1.80
κ [cm^{2}g^{-1}]	2	6	4	3.0	5.0

6.1.4 3D KS-Test and Probabilities

The best way to compare two distributions of data points is through a Kolmogorov-Smirnov (KS) test. This test yields the probability of two distributions being drawn from the same basic population. In one dimension, the KS-test compares the cumulative probability functions of a sample and a model and for large sample sizes the probability can be determined analytically. Since our distributions are three dimensional ($T_{\rm bol}$-$L_{\rm bol}$-$M_{\rm env}$), there are no analytical means to perform such a test. We therefore generalised the method of a two dimensional KS-test (e.g. Singh et al. 2004) for our purpose. The basic result of this test is the value $D_{\rm 3D}$ that ranges from zero to one. The lower this value, the better the two distributions match. Using a Monte Carlo method $D_{\rm 3D}$ can be converted to the agreement ($P_{\rm 3D}$), which gives the probability that the two distributions are drawn from the same population.

The task of finding the parameter set for the e-models that results in the highest agreement is a multi-dimensional, non-linear, minimisation problem. We solved this using a Monte Carlo approach. The details of this method, which allows to constrain the range for the e-model parameters and to determine the best agreement, are outlined in Froebrich et al. (2006).

6.2 Analysis and Discussion

6.2.1 Evolutionary Tracks

One of our goals is to investigate the accuracy to which the final mass of a protostar ($M_{\rm final}$) can be estimated from its present location in the $T_{\rm bol}$-$L_{\rm bol}$ diagram. To achieve this, we sort for each gt-model the individual model stars into final mass bins with a width of 0.3 in logarithmic units (equivalent to a factor two in mass).

The following ranges for the mass bins were chosen: < 0.2, 0.2...0.4, 0.4...0.8, 0.8...1.6, 1.6...3.2, $\geq 3.2\,M_\odot$. The particular size of the mass bins was adopted in order to ensure a reasonably large number of stars in each bin for the gt-models. Depending on the mass function and the total number of objects in the gt-model, there are up to 20 objects per bin for the lower masses ($M_{\rm end} \leq 1.6\,M_\odot$). The higher mass bins naturally suffer from a paucity of objects.

We determined for every gt-model the average accretion rate in each mass bin. These mean accretion rates are then used to determine evolutionary tracks in the $T_{\rm bol}$-$L_{\rm bol}$ diagram. The left column of Fig. 6.1 shows the tracks for the six mass bins of the models M05k8, M2k2, and M6k2a as an example. The lowest final masses correspond to the thinnest line, and so forth. Note that the average evolutionary tracks show higher $L_{\rm bol}$ at a given $T_{\rm bol}$ for higher final star masses. This represents the fact that stars with higher final masses on average have higher accretion rates (§ 5.3) and hence bolometric luminosities.

Further we analysed the individual evolutionary tracks. As an example, we plot all individual tracks for the same three models with final stellar masses in the range 0.8 to $1.6\,M_\odot$ (mass bin 4, solar mass stars) in the middle column of Fig. 6.1. These tracks are determined assuming the e-model parameters which best fit the observations (see below). We find that all tracks show a similar general behaviour. The tracks start off at $T_{\rm bol} \approx 15\,$K for solar mass stars. Lower mass Class 0 sources start off at higher temperatures. Then they show a gradual increase in luminosity until the end of the Class 0 phase. Some notable exceptions are evident in Fig. 6.1, which imply that $T_{\rm bol}$ is not always a reliable guide as to the envelope-protostar mass ratio.

Are we able to estimate the final mass of a Class 0 source from its position in the $T_{\rm bol}$-$L_{\rm bol}$ diagram? To address this question, we determined the 1σ scatter of the individual tracks at each time step in all mass bins. In the right column of Fig. 6.1 this scatter is shown for mass bin 4 as thin lines. Almost independent of the gt-model, we find that the scatter has about the size of the separation between tracks for two adjacent mass bins. Hence, we conclude that from a certain position in the $T_{\rm bol}$-$L_{\rm bol}$ diagram, *we are only able to estimate the final mass of the protostar to within a factor of two.* Note that this estimate does not take into account possible errors in the measurement of $T_{\rm bol}$ and $L_{\rm bol}$, as well as possible different accretion histories. This supports the notion that other observables might be more adequate for dating Class 0 protostars, e.g. the $L_{\rm smm}/L_{\rm bol}$ ratio (Young & Evans 2005), in agreement with the original observational definition of Class 0 sources (André et al. 1993).

We further find that tracks determined from averaged accretion rates noticeably differ from the averaged evolutionary tracks of the individual stars. This is evident in the right column of Fig. 6.1 which shows as a thick line the track from the averaged accretion rate. At some points, it approaches or even lies outside the $\pm 1\sigma$ range of the individual evolutionary tracks. This clearly shows, together with the findings in the above paragraph, that the individual accretion history significantly influences the position in the $T_{\rm bol}$-$L_{\rm bol}$ diagram, in addition to the final stellar mass.

The general behaviour of the $T_{\rm bol}$-$L_{\rm bol}$ tracks (characteristics of the individual tracks, the average tracks, and the scatter around the average) is independent of the considered mass bin and gt-model.

6.2.2 Distribution in $T_{\rm bol}$-$L_{\rm bol}$-$M_{\rm env}$

In Fig. 6.2 we show how the model tracks (M05k8, M2k2, M6k2a, from left to right) are distributed in the full $T_{\rm bol}$-$L_{\rm bol}$-$M_{\rm env}$ parameter space. The grey-scale background of the individual panels gives the probability to find one of the model stars at this particular position. Darker regions indicate higher probabilities. We used typical e-model parameters (see Table 6.2) to determine these diagrams. For comparison the observational datapoints are overplotted. Note that we plotted only model points with $T_{\rm bol} < 80\,{\rm K}$, as this is the limit of the observational data and only these are used in the comparison with the observations.

As evident in Fig. 6.2, the model distributions cover roughly the same area as the observations. Especially in the $T_{\rm bol}$-$L_{\rm bol}$ and $T_{\rm bol}$-$M_{\rm env}$ plane the models are able to explain the peak in the observed distribution. In the $L_{\rm bol}$-$M_{\rm env}$ plane, however, the models fail to explain this peak (see right column in Fig. 6.2). Our models predict smaller envelope masses compared to the majority of the observations. Considering, however, the cluster of observational points at about $M_{\rm env} = 1\,{\rm M}_\odot$, the discrepancy could well be a selection effect in the observations. See also the discussion in § 6.2.7.

6.2.3 Initial Mass Function

We analyse the mass function of the final masses of model stars (IMF) in the gt-models in order to compare it to that of the observational sample. The protostellar mass functions of the gt-models show a decline for masses larger than about $0.3\,{\rm M}_\odot$. The mean value of the slope of all considered models is $\langle\Gamma\rangle = -0.84$ in the mass range $-0.5 < \log {\rm M/M}_\odot < 1$. This is less steep than the Salpeter slope of -1.35 (Salpeter 1955) but our results are biased by the fact that binaries or multiple systems cannot be resolved. At the low-mass end, the mass function is constrained by the SPH resolution limit of $\sim 0.05\,{\rm M}_\odot$. Nevertheless, the mean value is in good agreement with the estimated final stellar mass spectrum in the corresponding observational sample (Γ = -0.9±0.2; Froebrich 2005). Recall that for this sample also no binary correction has been made.

We test if the slope of the IMF in the gt-models is related to the best agreement ($P_{\rm 3D}$). However, no systematic dependence of $P_{\rm 3D}$ on Γ is present. In particular, a good agreement of Γ between the gt-model and the observations does not necessarily lead to a high $P_{\rm 3D}$-value. As discussed in the last paragraph (see also the middle panel of Fig. 6.1), the differences in the position in the $T_{\rm bol}$-$L_{\rm bol}$ diagram are partly due to the accretion history and not due to the final mass. Hence, the test performed here is much more sensitive to the distribution of individual accretion histories than to the slope of the IMF.

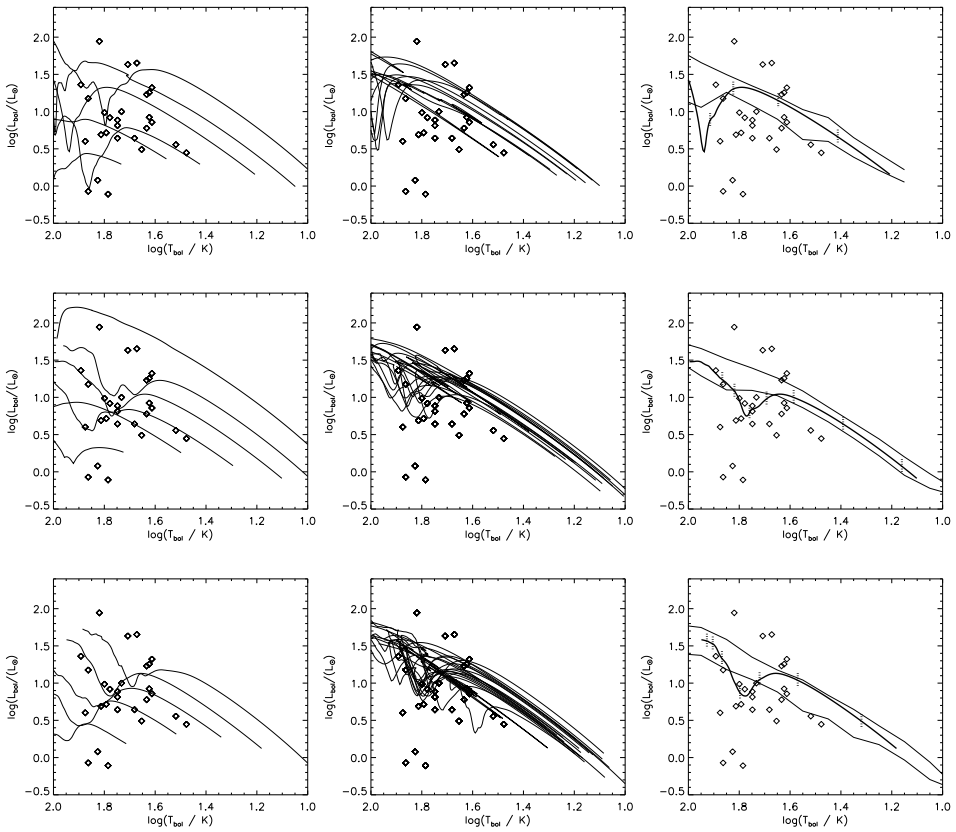

Figure 6.1: Evolutionary tracks in the $T_{\rm bol}$-$L_{\rm bol}$ parameter space of the model Class 0 sources in the models M05k8 (top row), M2k2 (middle row), and M6k2a (bottom row). The tracks are determined using typical e-model parameters from the range best fitting the observations (see Table 6.2). Left column: Tracks for the average accretion rates in the six mass bins. Thicker lines correspond to higher final masses. Note that there are no stars in mass bin 6 in the M6k2a model. Middle column: All individual tracks in mass bin 4. Right column: Track for average accretion rate of stars in mass bin 4 (solar mass stars; thick line) and the $\pm 1\sigma$ scatter of the individual tracks (thin lines). The vertical lines mark ages of the sources starting from 5×10^3 yrs in steps of 5×10^3 yrs. The open diamonds in each panel mark the positions of the observational sample (taken from Froebrich 2005). See Sect. 6.2.1 for more details.

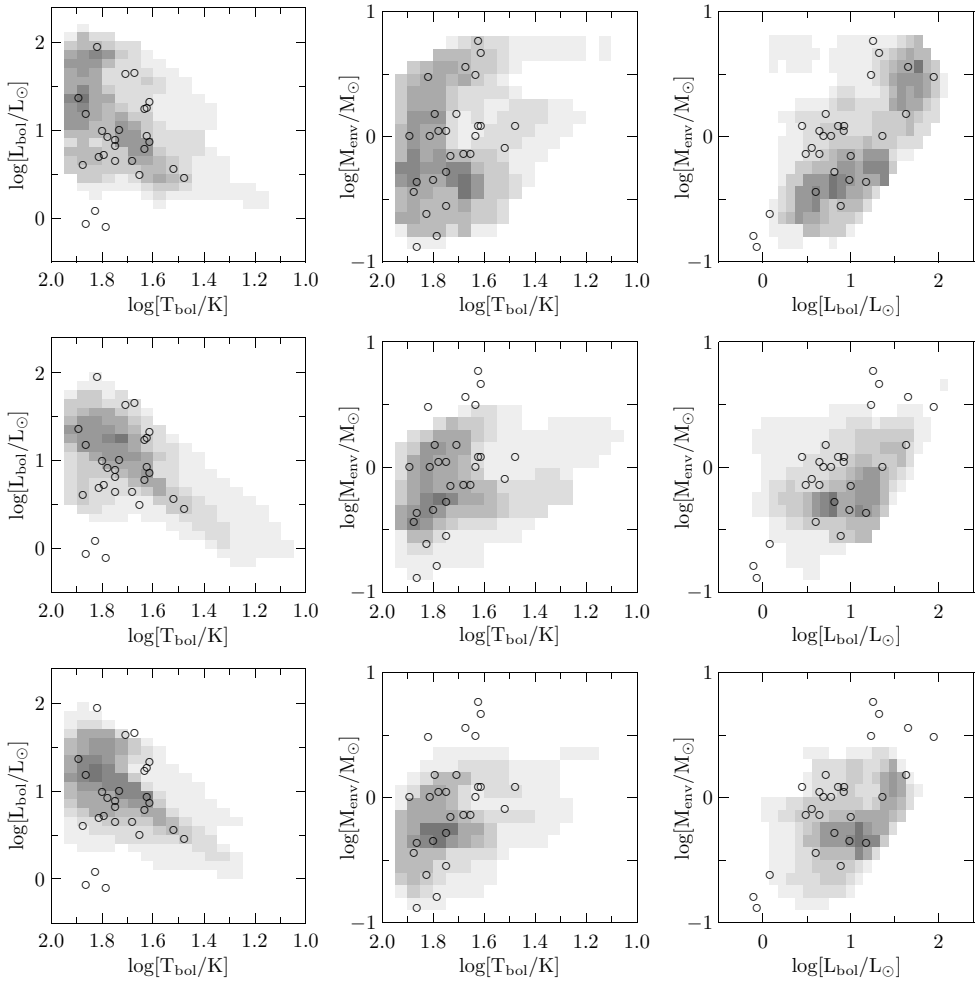

Figure 6.2: Distribution of Class 0 observations (circles) and models (grey-scale) in the $T_{\rm bol}$-$L_{\rm bol}$ (left column), $T_{\rm bol}$-$M_{\rm env}$ (middle column), and $L_{\rm bol}$-$M_{\rm env}$ (right column) plane of the parameter space. The plots are shown for the models M05k8 (top row), M2k2 (middle row), and M6k2a (bottom row). Darker grey-values in the model distribution correspond to higher density of model points. As in Fig. 6.1 typical e-model parameters are used for the model distributions (see Table 6.2). Only model points with $T_{\rm bol} < 80\,{\rm K}$ are shown in the plots since this is the limit of the observational data.

Table 6.2: Parameter ranges needed in the e-model to best match the observational data (see Appendix B of Froebrich et al. 2006 for details on the parameters). We list the values for the best fitting 5% of the parameter combinations. The last two columns list the median and average duration of the Class 0 phase of the individual stars in the models.

Model	T_{env}	$frac_{\rm env}$	$M_{\rm extra}$	t_0	α	$R_{\rm in}$	$M_{\rm eff}$	p	κ	$D_{\rm 3D}$	$P_{\rm 3D}$	$t^{\rm med}_{\rm Cl\,0}$	$t^{\rm ave}_{\rm Cl\,0}$
	[K]	[%]		[10^3 yrs]		[AU]	[%]		[cm^{2}g^{-1}]		[%]	[10^3 yrs]	[10^3 yrs]
G2	15-19	81-89	0.6-2.4	35-75	1.4-3.2	30-80	44-47	1.6-1.9	3.0-5.2	0.30-0.35	37.2 - 9.99	41	44
M01k2	14-18	87-95	1.0-2.8	20-85	1.4-3.4	40-75	28-44	1.6-1.8	3.0-4.6	0.37-0.42	10.8 - 1.70	39	41
M05k4	17-20	89-94	1.2-2.0	35-75	1.6-3.2	45-85	41-44	1.5-1.7	3.0-4.4	0.32-0.37	22.6 - 6.23	31	36
M05k8	16-19	90-95	0.9-2.0	25-80	1.9-3.0	40-85	40-46	1.5-1.7	3.0-4.6	0.38-0.44	30.7 - 5.75	31	34
M2k2	15-20	86-92	1.0-2.4	35-85	1.6-3.2	35-80	35-43	1.5-1.7	3.4-5.2	0.31-0.38	53.6 - 12.2	32	39
M2k4	15-18	86-92	1.0-2.4	35-75	1.4-3.2	40-75	39-43	1.5-1.7	3.2-5.2	0.48-0.52	30.5 - 4.85	15	23
M2k8	13-18	80-90	1.0-2.2	30-75	1.2-3.6	35-75	32-41	1.5-1.7	3.4-5.4	0.27-0.36	65.2 - 10.3	45	56
M3k2	15-18	82-94	0.6-2.6	20-90	1.4-3.6	35-85	37-44	1.5-1.8	2.8-4.6	0.31-0.38	35.4 - 4.24	44	43
M3k4	12-14	80-92	0.6-1.6	25-80	1.4-3.4	30-70	32-44	1.5-1.8	3.2-5.2	0.34-0.39	5.71 - 0.86	87	105
M6k2a	16-20	85-95	1.0-2.4	20-85	1.4-3.4	45-85	35-43	1.6-1.8	2.8-4.6	0.32-0.37	41.5 - 16.0	26	32
M6k4a	15-20	93-97	0.8-3.2	40-80	1.4-3.2	30-70	12-34	1.6-1.8	3.2-5.2	0.47-0.50	0.04 - 0.01	38	120
M6k2b	15-20	82-94	1.2-3.0	35-80	1.6-3.2	35-75	36-40	1.6-1.8	3.2-5.4	0.37-0.41	9.50 - 1.97	26	35
M6k2c	15-20	86-96	1.0-3.0	35-75	1.4-3.2	35-75	36-42	1.6-1.9	3.4-4.8	0.38-0.44	4.26 - 0.56	29	51
M6k4c	13-18	82-85	0.6-2.6	20-85	1.2-3.2	30-80	28-44	1.5-1.8	3.0-5.2	0.45-0.51	22.2 - 2.17	14	54
M10k2	16-22	92-96	1.0-3.6	25-70	1.2-3.0	35-80	10-42	1.6-1.9	3.2-5.4	0.60-0.62	0.003- 0.00	19	24
M10k8	14-17	93-98	0.8-3.2	30-85	0.8-3.8	35-80	16-38	1.5-1.7	3.4-5.2	0.45-0.50	1.47 - 0.13	44	124

6.2.4 Evolutionary Model

To constrain the free parameters in the e-model, we investigate here how the chosen values influence the agreement P_{3D}. Table 6.2 contains the range of values which provide the highest agreement for each gt-model. In particular we show the values for the best fitting 5% of the e-models. It is more meaningful to provide these ranges instead of the particular parameters for the single best fitting model. These are statistically less significant, since not the whole parameter space is tested by our method. We obtain the following results for all gt-models:

- The temperature at the outer envelope boundary is lower than the standard value of 24 K. Typically temperatures between 15 and 19 K lead to a good agreement.

- A wide range for inner envelope radii (R_{in}) leads to high P_{3D}. Values from 35 to 80 AU are typical. This wide range is in agreement with the fact that a change in R_{in}, while fixing all other parameters, usually results in very small changes of P_{3D}. However, the range for the best fitting models does not include the hitherto standard value of 30 AU.

- In most cases small amounts of extra mass in the envelope ($1.0 < M_{extra} < 2.4$) lead to high agreement.

- The parameter α shows a wide range of possible values for a good agreement ($1.4 < \alpha < 3.2$). A similar wide range is found for t_0 which ranges from 30 to 80×10^3 yrs. The larger values found for t_0 suggest that the additional mass stays longer in the envelope to sustain low bolometric temperatures.

- A range of values of p is found to be able to best explain the data. However, in the majority of the cases $1.55 < p < 1.80$ leads to the best results. These values are in between the theoretical solutions for a free falling envelope (1.5) and a singular isothermal sphere (2.0). The range found here seems to be a compromise between younger and older objects. Since there are probably more older sources in the sample, the best values are closer to $p = 1.5$. In principle an evolution from $p = 2.0$ to $p = 1.5$ would be expected. Our findings do not contradict this. Our obtained values are in good agreement with (sub)-mm observations of envelopes (Chandler & Richer 2000; Motte & André 2001).

- We found the mass fraction in the envelope to be in the range from 86 to 96%. This would imply a disc mass of 4 to 14% of the envelope mass, mostly smaller than the standard value of 13% used so far, but in agreement with millimetre interferometric observations (e.g. Looney et al. 2003).

- The amount of mass ejected into the jets is found to range from 36 to 44%. This is a narrow range and somewhat contradictory to the observations and

jet launching models which predict that at maximum 30% of the material is ejected into the jets. We interpret the high amount of ejected material here as a combination of two things. (1) Material really ejected into the jets. (2) Material accreted onto the star, but the resulting luminosity escapes directly through the cavity generated by the jets and is not observed. If the accretion luminosity is radiated uniformly away, then the additional ejected material would imply opening angles between 30 and 60° for the cavities, not an untypical value for many of the older Class 0 sources (e.g. Padman et al. 1997). To conclusively prove this hypothesis one needs to include the outflow luminosity for all objects into the comparison of models and observations.

- The best-fitting opacity range (3.0 to 5.0 $\mathrm{cm^2 g^{-1}}$) agrees very well with the standard value of 4 $\mathrm{cm^2 g^{-1}}$.

6.2.5 Gravoturbulent Models

We now investigate if the initial conditions of the gt-models influence the agreement with the observations. The first point to note is that we find no significant correlations of P_{3D} or any of the obtained parameter values of the e-models with the Mach number or wavelength that characterise the turbulence in the gt-model. This is understandable since protostellar collapse is, in essence, a rather localised process, connected to the turbulent cloud environment only via the available mass and angular momentum inflow rate.

There are, however, large differences in the quality of agreement between the various gt-models and the observations. In the following we investigate the cause of these differences. We determined for each set of accretion rates the median and the mean duration of the Class 0 phase of the model stars. The median for all gt-models ranges from 14 to 87×10^3 yrs, while the mean duration spans from 23 to 124×10^3 yrs. The much wider range for the average duration is due to some model stars (outliers) that go through an extremely long Class 0 phase. These objects have a large, secondary accretion peak, which in many cases might not be physical, but caused by the lack of feedback mechanisms. Due to the mass criterion used, such peaks shift the transition from Class 0 to 1 to later times. In Table 6.2 we list the median and mean duration of the Class 0 phase of all stars in the models in the last two columns.

All gt-models with P_{3D}-values larger than 20% are associated with a mean duration of the Class 0 phase between 20 and 60×10^3 yrs. Most of them possess a ratio of median to mean duration of the Class 0 phase of larger than 0.7. This indicates that no or only a few outliers are present in the set of accretion rates. When applying these two conditions to all gt-models, we select nine of them (see Fig. 6.3). This includes all models with P_{3D}-values larger than 20% and M01k2 (10.8%) and M6k2b (9.5%). Hence 80% of the gt-models with these properties lead to high agreement. There are seven models that do not fulfil one of the cri-

teria. Five of these posses P_{3D}-values smaller than 20%. Hence 70% of the gt-models that do not comply with both criteria lead to low agreement. This shows that high P_{3D}-values are only obtained for gt-models that generate few outliers and the 'right' duration of the Class 0 phase.

The duration of the Class 0 stage shows a linear correlation with the median of the fit parameter τ defined in § 5.4. This parameter indicates the time it takes until the peak accretion rate is reached. It is related to the local free-fall time and, thus, can be used as a rough estimate of the average density of the core at the onset of collapse (see § 5.4). Given our best fitting models and the corresponding Class 0 lifetimes, we infer a range of $(1 - 5) \times 10^5\,\mathrm{cm}^{-3}$ for the local density at the start of the collapse. This is in good agreement with measured central densities of pre-stellar cores (e.g. Bacmann et al. 2002). Our results thus suggest that stars may only form in pre-stellar cloud cores that reach a central density of order of $10^5\,\mathrm{cm}^{-3}$. Obviously, the duration of the Class 0 phase depends directly on the initial local density.

As can be seen in Table 6.2, gt-models with Mach numbers $0.5 \leq \mathcal{M} \leq 3$ best describe the observations (filled symbols in Fig. 6.3). Six out of seven such models possess a high P_{3D}-value, while only one out of eight models with $\mathcal{M} \geq 6$ has a high P_{3D}. The exceptions M3k4 ($\mathcal{M} < 6$, $P_{3D} = 5.99\%$) and M6k2a ($\mathcal{M} \geq 6$, $P_{3D} = 46.5\%$) as well as the fact that similar gt-models (e.g. M6k2a/b/c) result in very different P_{3D}-values are, however, understandable since protostellar collapse is, in essence, a rather localised process, connected to the turbulent cloud environment only via the available mass and angular momentum inflow rate. It indicates that star formation is a highly stochastic process, influenced more strongly by local properties than by the global initial conditions, a fact which is also found, for example, by Bate et al. (2003).

The range of Mach numbers found as best explanation for the data reflects the composition of the observational sample. It mainly contains sources from Perseus, Orion, and Serpens (Froebrich 2005). There typical Mach numbers are in the range $1 \leq \mathcal{M} \leq 6$ (e.g. Castets & Langer 1995; Schmeja et al. 2005). It is, however, interesting to note that the majority of gt-models with $\mathcal{M} \geq 6$ are not able to explain the observations, independent of the choice for the e-model parameters. This indicates that the initial conditions do influence the observational properties of Class 0 protostars.

6.2.6 Underluminous Sources

We recall that we excluded 25% of the observational data in our determination of P_{3D}. The excluded data exhibit a much lower bolometric luminosity than the other objects, given their bolometric temperature and envelope mass. They could be objects which experience either (a) quiescent states of low accretion or (b) a different time dependence of the accretion rate (Froebrich 2005).

A detailed investigation of the individual accretion rates from the gt-models rules out the existence of quiet accretion phases as the dominant cause for the low

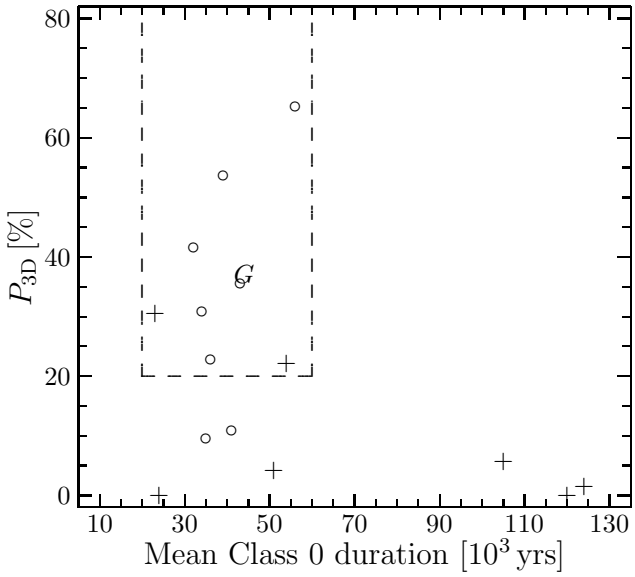

Figure 6.3: Mean duration of the Class 0 phase of the model stars vs. the P_{3D} value for the gravoturbulent models. Circles mark models that possess a median duration of the Class 0 phase between 2 and 6×10^4 yrs and a ratio of median to mean duration of the Class 0 phase of higher than 0.7. Triangles mark models were one of these conditions is not fulfilled. Gravoturbulent models with Mach numbers in the range $0.5 \leq \mathcal{M} \leq 3.0$ are shown as filled symbols, models outside this range as open symbols. The Gaussian collapse model is marked as '*G*'. The dashed lines enclose the region where a high agreement of the models with the observations was found.

luminosity of these sources. On average, the individual model stars spend less than 5% of their time in a phase of suppressed accretion which we define as being a factor of six lower than the average value. This implies that we should observe only about 5% of the sources in such a state, compared to 25%. Hence, these objects appear to follow a different accretion history.

We investigate this in more detail by performing the procedure of determining P_{3D} using not only the 'normal' sources, but also the Taurus-like objects. We find that this reveals worse agreement, with P_{3D} values typically halved. The agreement between models and observations is always lower when we try to explain the Taurus like sources. This strengthens the proposal that in the case of 'normal' sources, turbulence governs the accretion process, while other processes are responsible for the underluminous objects. Considering their lower luminosity and hence lower accretion rates, we speculate that ambipolar diffusion might be an important process governing accretion in these sources.

A more detailed analysis of a sub-sample of Taurus-like objects would be desirable since the time dependence of the mass accretion rate might vary from region

to region (Henriksen et al. 1997). Even though more and more such objects are discovered (e.g. Young et al. 2004), indicating that the known percentage of these objects is clearly a lower limit, the current sample still suffers from too small number statistics to perform a reliable statistical analysis.

6.2.7 Further Discussion

As evident from Table 6.2, the best agreement between observations and models is rather low ($\sim 70\%$). Here we will discuss three possible causes for this:

Our procedure: As can be seen in Table 6.1 there are many free parameters, which, in principle, could possess a large range of values. A straight forward test of all possible combinations to solve this highly non-linear minimisation problem of many variables is impossible. We thus used a Monte Carlo method to obtain the best fitting parameter combination. The obtained probability P_{3D} is a lower limit, since not all possible parameter combinations have been tested. Note that only slightly smaller values for D_{3D} can lead to probabilities much closer to 100%, especially for models that already possess a high agreement.

When converting D_{3D} to P_{3D} we restricted the random selection to model values with bolometric temperatures smaller than 80 K. This is the limit of our observational sample of Class 0 sources. There are further restrictions in the observational data. No objects are outside a given range in L_{bol} and M_{env}. This is most likely an observational bias. We refrain from applying the other observational limits for the random selection process for the P_{3D} determination because the observational limits are not well defined/understood. If we did so, however, we would increase the probabilities for the agreement in many cases significantly towards 100%.

Observational data: As stated above, the observations clearly cover only a limited range of the T_{bol}-L_{bol}-M_{env} parameter space. All limits, except $T_{bol} < 80$ K, are observational biases. Note that the observational sample consists of sources from several star forming regions. It is possible that e.g. the sensitivity limit for the bolometric luminosity is not the same in all regions, changing the observed statistics of low luminosity/mass sources compared to the real one.

As shown in Fig. 6.1, applying a fixed limit for T_{bol} as divide between Class 0 and Class 1 objects is not valid (see also Young & Evans 2005). Most of the solar mass stars undergo this transition at temperatures close to 80 K. However, depending on the individual accretion history of each star, partly significant deviations from this value are evident. Furthermore, lower mass Class 0/Class 1 transition objects tend to be warmer than the temperature limit applied here. Thus, the object sample might suffer from miss-classified objects. This also shows that there is a difference in the definition for Class 0 protostars based on observations and models. Further the observational definition describes a different physical state of the object depending on its accretion history and final mass. We overcome most of

these uncertainties, however, by applying the $T_{\rm bol} < 80\,{\rm K}$ restriction when determining $P_{\rm 3D}$.

The models: All our models are constructed on the most basic principles (e.g. the gt-models neglect feedback mechanisms, the disc mass is a constant fraction of the envelope mass, etc.). Further all model stars are treated with the same set of e-model parameters. It is not clear if some of the parameters might depend on the final mass of the star. Many parameters are also kept constant in time. This as well might be not a valid (e.g. the inner envelope radius, the fraction of mass in the disc, and the powerlaw index of the envelope density distribution might depend on the evolutionary state and final mass of the star). It is in many cases, however, uncertain how these dependencies can be parameterised. We thus kept these parameters constant, not to introduce even more free arbitrary parameters.

Given these three points, we conclude that a very good agreement between the models and observations should not be expected. It would rather be very worrying if our method would result in a 99% agreement between models and observations. We further have to consider the possibility that star formation, and in particular the mass accretion process, might take such a diversity of paths that no simple unifying model can expect to capture them all, leading to small agreements even for future much improved observational samples and models.

6.3 Conclusions

We extracted mass accretion rates within cores generated by gravoturbulent simulations and inserted them into a simple protostellar evolutionary scheme to calculate protostellar evolutionary tracks. A principle dependence of the position of these tracks in the $T_{\rm bol}$-$L_{\rm bol}$ diagram on the final mass is found. A detailed analysis, however, shows that we are not able to determine the final mass of a particular object from its measured bolometric temperature and luminosity more accurately than a factor of two. The particular shape of an evolutionary track is largely determined by the accretion history and by its final mass. Hence, in the context of the gravoturbulent model, unique evolutionary tracks do not exist in the Class 0 or Class 0/1 phase, as opposed to the ensuing pre-main sequence evolution. It also implies that $T_{\rm bol}$ is not always a reliable guide to the envelope-protostar mass ratio, as suggested also by Young & Evans (2005).

A 3D-KS-test was used to compare the distribution of our evolutionary tracks in the $T_{\rm bol}$-$L_{\rm bol}$-$M_{\rm env}$ parameter space with an observational sample of Class 0 objects. By varying free parameters associated with the evolutionary scheme, we are able to determine constraints for some of the parameters ($T_{\rm env}$, $frac_{\rm env}$, $M_{\rm extra}$, $M_{\rm eff}$, p). Other parameters were found to have no significant influence on the agreement between models and observations (t_0, α, $R_{\rm in}$, κ). A comparison of the parameter values obtained by our method with observational constraints from indi-

vidual objects (e.g. for $frac_{\rm env}$ or p) can be conducted. This proves the reliability of our method since similar parameter values are obtained.

Only gravoturbulent models generating model stars with a certain density at the start of the collapse and Class 0 lifetimes between 20 and 60×10^3 yrs lead to a good agreement with the observations. This Class 0 lifetime is in good agreement with estimates of a few 10^4 yrs based on number ratios or dynamical timescales of outflows (see e.g. André et al. 2000). It is shown that the Class 0 lifetime is correlated with the local density at the onset of the collapse. The determined density range agrees well with density measurements for pre-stellar cores. Limiting the accretion phase to ten crossings of the computational box in the gravoturbulent model always leads to better agreement with the observations. This is consistent with the notion that protostellar feedback processes (e.g. by outflows or winds) may be an important mechanism to terminate star formation within two to three dynamical timescales.

Apparently the environment (Mach number and scale of the driving turbulence) and the initial mass function do not influence the agreement systematically. The highest probability found, that our distributions of model tracks and observational data points are drawn from the same basic population, is 70%. This is understandable, given the uncertainties in the observations and the simple assumptions in the models. However, the method can be readily adapted to compare larger future source samples, different sets of accretion rates or other envelope models.

By applying the KS-test to both the 'normal' and underluminous, 'Taurus-like' objects in the source sample, we find that the determined probability $P_{\rm 3D}$ is about twice as large when testing only the 'normal' objects. This is consistent with the assumption that turbulence governs the accretion rates in the majority of the objects.

Chapter 7

Number Ratios of Young Stellar Objects*

Look up at the heavens and count the stars – if indeed you can count them.
– Genesis 15:5

Embedded clusters usually contain young stellar objects belonging to different classes. Since these classes form an evolutionary sequence, the numbers of objects in each individual class can tell us something about the evolutionary stage of the cluster, e.g. the more Class 3 and the less Class 0/1 objects a cluster has, the more evolved it presumably is. In this chapter, we investigate number ratios of objects in these classes in the star-forming regions ρ Ophiuchi, Serpens, Taurus, Chamaeleon I, NGC 7129, IC 1396A, and IC 348. For this purpose we compile an observational sample of absolute numbers of YSOs belonging to the different classes from the literature. The number rations can then be compared to the temporal evolution of young stars in the simulations in order to constrain the models and to possibly determine the evolutionary stage of the clusters.

7.1 Observational Data

The detection and classification of prestellar cores and Class 0/1/2/3 objects requires different observational techniques. Thus, we have to construct our samples from various sources. We consider corresponding areas on the sky, but the caveat remains that the combined samples may be far from complete and not homogeneous. Since it would hardly effect the relative numbers, the problem of unresolved binaries can be neglected. Besides, we cannot resolve close binaries in the SPH models either. The absolute and relative numbers of YSOs adopted from the observations for the subsequent analysis are listed in Table 7.1.[1] Prestellar cores

*This chapter is based on Schmeja, S., Klessen, R. S., & Froebrich, D. 2005, A&A, 437, 911

[1]Note that there are discrepancies to the numbers of YSOs given in Table 2.2, which may contain estimates or consider a larger area and has only illustrative purpose.

Table 7.1: Absolute *(upper panel)* and relative *(lower panel)* numbers of YSOs of different classes from observations (for references see text).

Region	prestellar	0	1	2	3
ρ Oph	98	2	15	111	77
Serpens	26	5	19	18	~20
Taurus	52	3	25	108	72
Cha I	<71	2	5	175	
IC 348		2	2	261	
NGC 7129		1	20	80	
IC 1396A		2	6	47	1
ρ Oph		0.01	0.07	0.92	
Serpens		0.08	0.31	0.61	
Taurus		0.01	0.12	0.87	
Cha I		0.01	0.03	0.96	
IC 348		0.01	0.01	0.98	
NGC 7129		0.01	0.20	0.79	
IC 1396A		0.03	0.11	0.86	

are hard to determine both from observations and in our models, and in particular they are hard to compare, since the status of the cores (Jeans-critical or subcritical) is often unknown. Some cores considered as "starless" might even in fact turn out to harbour embedded sources (Young et al. 2004). Therefore we do not use them for the actual comparison, but keep them as an additional test for consistency. Due to constraints from the models (see § 3.5), we consider Classes 2 and 3 combined. So in the lower panel of Table 7.1 only Class 0, Class 1, and the combined set of Class 2+3 objects are shown.

7.1.1 ρ Ophiuchi

The ρ Ophiuchi molecular cloud is the closest and probably best-studied star-forming region, offering the most complete sample of YSOs. Bontemps et al. (2001) find a total number of 16 Class 1 sources, 123 Class 2 sources, 38 Class 3 sources, and 39 Class 3 candidates. They did not detect the previously known two Class 0 objects lying within their area. Following the reasoning of Bontemps et al. (2001) and the findings of Grosso et al. (2000) that there might be almost as many Class 3 as Class 2 objects, we add the candidates to the Class 3 sample, yielding a total number of 77 Class 3 sources. Stanke et al. (2006) performed a 1.2 mm dust continuum survey of the ρ Oph cloud and detected 118 starless clumps and a couple of previously unknown protostars. About the same number of cores was detected by Johnstone et al. (2004) by a 850 μm survey. To obtain a reasonably homogeneous sample when combining the Bontemps et al. (2001) and Stanke et

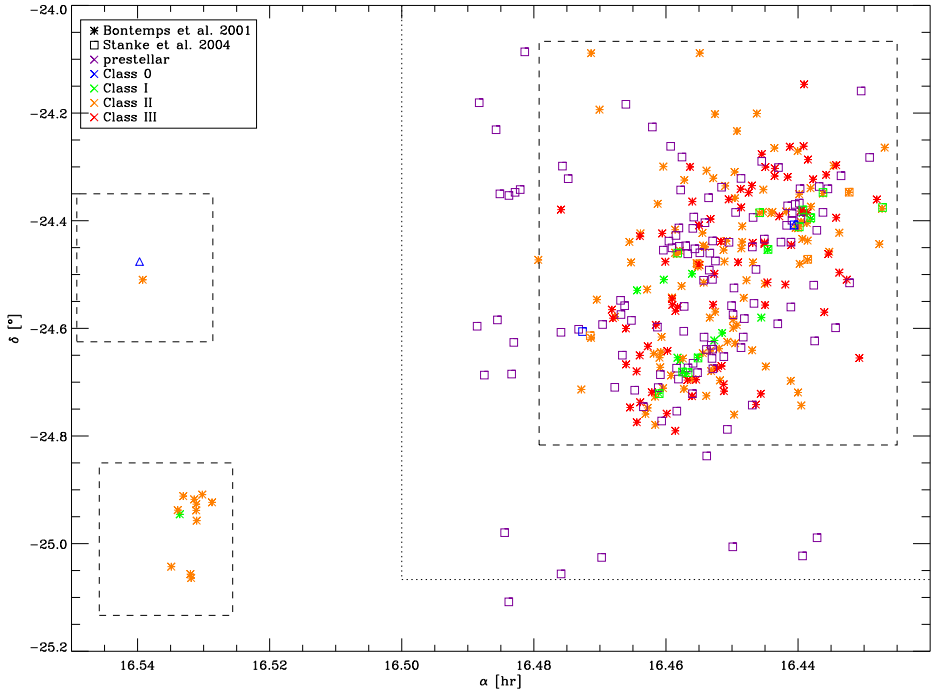

Figure 7.1: The positions of the YSOs and prestellar cores in ρ Oph from Bontemps et al. (2001) and Stanke et al. (2006). The dashed lines confine the areas investigated by Bontemps et al. (2001), the dotted line shows the field covered by Stanke et al. (2006). Only objects lying within the large dashed box are considered.

al. (2006) surveys we restrict ourselves to the range covered by both investigations, which is the $45' \times 45'$ region of the main ρ Oph cloud L1688 investigated by Bontemps et al. (2001) (see Fig. 7.1). This area contains two Class 0 sources (Froebrich 2005; Stanke et al. 2006). The global star formation efficiency (SFE) in L1688 is estimated at 6 – 14%, although the local SFE in the subclusters where active star formation takes place is significantly higher at $\sim$ 31% (Bontemps et al. 2001). The measured velocity dispersion is 2.6 km s^{-1} in ρ Oph A and 2.7 km s^{-1} in ρ Oph B (Kamegai et al. 2003). With the reported temperatures of 11 and 7.8 K (Kamegai et al. 2003) this corresponds to Mach numbers of $\mathcal{M} \approx 13.5$ and $\mathcal{M} \approx 15.5$, respectively.

7.1.2 Serpens

The Serpens Cloud Core, a very active, nearby star-forming region, contains 26 probable protostellar condensations (Testi & Sargent 1998) and five Class 0 sources (Hurt & Barsony 1996; Froebrich 2005). Kaas et al. (2004) detected 19 Class 1 and 18 Class 2 objects in the central region (covering the field investigated by Testi & Sargent 1998). This is an unusually high Class 1/2 ratio compared to other regions.

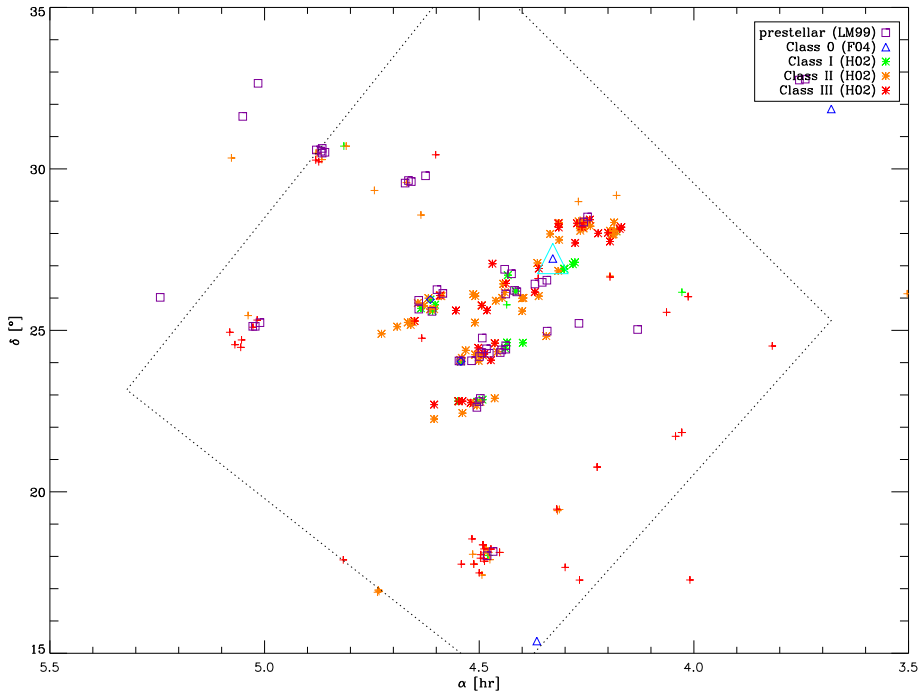

Figure 7.2: Positions of YSOs in Taurus: Class 1, 2, 3 objects from Hartmann (2002), Class 0 sources from Froebrich (2005), prestellar cores from Lee & Myers (1999). The dotted line shows the field covered by Hartmann (2002). Only objects lying within this area are considered.

Kaas et al. (2004) cannot distinguish between Class 3 sources and field stars and are therefore unable to give numbers for Class 3. Preibisch (2003) performed an *XMM-Newton* study of Serpens and detected 45 individual X-ray sources, most of them Class 2 or Class 3 objects. Considering this and the argumentation of Kaas et al. (2004) we can assume that there are at least as many Class 3 as Class 2 sources in the relevant area. The local SFE in sub-clumps is around 9%, the global SFE is estimated to be around $2-10\%$ (Kaas et al. 2004; Olmi & Testi 2002). The measured velocity dispersion is $0.3-0.6$ km s^{-1} (Olmi & Testi 2002), corresponding to $1 \lesssim \mathcal{M} \lesssim 2.5$ at $T = 20$ K.

7.1.3 Taurus

The Taurus molecular cloud shows a low spatial density of YSOs and represents a somewhat less clustered mode of low-mass star formation (Fig. 7.2). The numbers of Class 1, 2, and 3 sources in Taurus are reported as 24, 108, and 72, respectively (Hartmann 2002). In the same area there are 52 prestellar cores (Lee & Myers 1999), and one Class 0 and three Class 0/1 sources (Froebrich 2005). For our analysis we divide the Class 0/1 objects into two Class 0 and one Class 1 ob-

ject. Since the prestellar cores in the sample of Lee & Myers (1999) were selected by optical extinction, their number may be underestimated compared to other regions. Estimates for the star formation efficiency vary between 2% (Mizuno et al. 1995) and 25% in the dense filaments (Hartmann 2002). The velocity dispersion is 0.49 km s^{-1} (Onishi et al. 1996), corresponding to $\mathcal{M} \approx 2.5$, adopting a mean temperature of $\sim$ 11 K, i.e. a sound speed of 0.2 km s^{-1}.

7.1.4 Chamaeleon I

The Chamaeleon I molecular cloud harbours 126 confirmed and 54 new YSO candidates, most of them classical or weak-line T Tauri stars (Class 2/3). Furthermore, four probable Class 1 protostars are detected by the *DENIS* survey (Cambrésy et al. 1998). Persi et al. (2001) find two more Class 1 sources. One object is classified as Class 0, and one as Class 0/1 by Froebrich (2005). Counting the latter as Class 0 gives a total of two Class 0 and five Class 1 sources. Haikala et al. (2005) detected 71 clumps (some of them associated with embedded protostars) and a mean line width of 0.62 km s^{-1} in the clumps, corresponding to $\mathcal{M} \approx 3$ at $T \approx 11$ K. The SFE in Cha I is about 13% (Mizuno et al. 1999).

7.1.5 IC 348

The young nearby cluster IC 348 in the Perseus molecular cloud complex contains 288 identified cluster members (Luhman et al. 2003), including 23 brown dwarfs. The majority of the objects are believed to be in the T Tauri stage (Class 2/3) of pre-main sequence evolution (Preibisch & Zinnecker 2004). The active star formation phase seems to be finished in the central parts of the cluster, but southwest of the cluster centre a dense cloud core containing several embedded objects is found. There are two Class 1 objects (Preibisch & Zinnecker 2002), one confirmed Class 0 source and one Class 0 or 1 source (Froebrich 2005), which we count as Class 0 in our analysis. Subtracting the brown dwarfs, we adopt a number of 261 Class 2/3, two Class 1 and two Class 0 objects. The average velocity dispersion is 1.04 km s^{-1} (Ridge et al. 2003), corresponding to $\mathcal{M} \approx 5.2$ at $T \approx 11$ K.

7.1.6 NGC 7129 and IC 1396A

With NGC 7129 and IC 1396A we include two additional star-forming regions in our analysis. Although there is no information on prestellar cores in the literature, sufficient data about the population of young stellar objects can be found. The numbers of YSOs in these two clusters are based on data from the *Spitzer Space Telescope*, which are not available for the other regions. Since *Spitzer* is very sensitive to the earliest YSO classes, the obtained number ratios might be overestimated in favour of Class 0 and 1 compared to the other regions.

In NGC 7129 Muzerolle et al. (2004) detected one Class 0 object (classified as Class 0/1 by Froebrich 2005), 12 Class 1 objects and 18 Class 2 sources in

their *Spitzer* data. They miss the core cluster members and estimate a total of 20 Class 0/1 and 80 Class 2 objects, which is a similar ratio as in Taurus or ρ Oph. The average velocity dispersion is 1.58 km s^{-1} (Ridge et al. 2003), corresponding to $\mathcal{M} \approx 8$ at $T \approx 11$ K. This region has also been studied by Megeath et al. (2004), see also below.

The Elephant Trunk Nebula, IC 1396A, was investigated by Reach et al. (2004) using *Spitzer* data, revealing three Class 0/1, five Class 1, 47 Class 2, and one Class 3 object. These numbers are similar to the numbers of YSOs found by Froebrich et al. (2005), who however cannot distinguish between Class 1 and Class 2/3 sources. For our analysis we divide the Class 0/1 objects into two Class 0 and one Class 1 object. Reach et al. (2004) estimate a SFE of 4 – 15%.

7.1.7 Other Star-Forming Regions

Megeath et al. (2004) report *Spitzer* results on the four young stellar clusters Cepheus C, S171, S140, and NGC 7129. They find ratios of Class 1 to Class 2 objects between 0.37 and 0.57, which is significantly higher than in the other regions listed in Table 7.1 except Serpens. That indicates that these clusters are very young, although the same caveat for *Spitzer* data as above applies. Since no data of Class 3 objects are available we do not include these clusters in our analysis.

7.2 Restrictions to the Models

The YSO classes of the model stars are determined as described in § 3.5. In order to avoid problems with the described mass criteria for the determination of the classes for low-mass objects and to be consistent with the observations, we only consider protostars with a final mass $M_{\rm end} \geq 0.1$ M$_\odot$, which roughly corresponds to the detection limits of the observations reported in the literature. For the same reason we only consider models with a numerical resolution of at least 200 000 particles. Furthermore, in order to get reasonable numbers of protostars in the different classes we select only those models where more than 37 protostars with $M_{\rm end} \geq 0.1$ M$_\odot$ are formed. This corresponds to the definition of a star cluster by Lada & Lada (2003) as a group of 35 or more physically related stars. These restrictions reduces our set of models to 16.

7.3 The Evolutionary Sequence

Figure 7.3 shows the temporal evolution of the numbers and the fractions of the different YSO classes for three selected models. The formation of the entire cluster takes place on varying timescales between about two and 25 global free-fall times. In the Gaussian collapse models and the turbulent models with small Mach numbers the formation tends to be faster, because self-gravity dominates the large scales. The numbers of Class 0 protostars show only a narrow peak, followed by

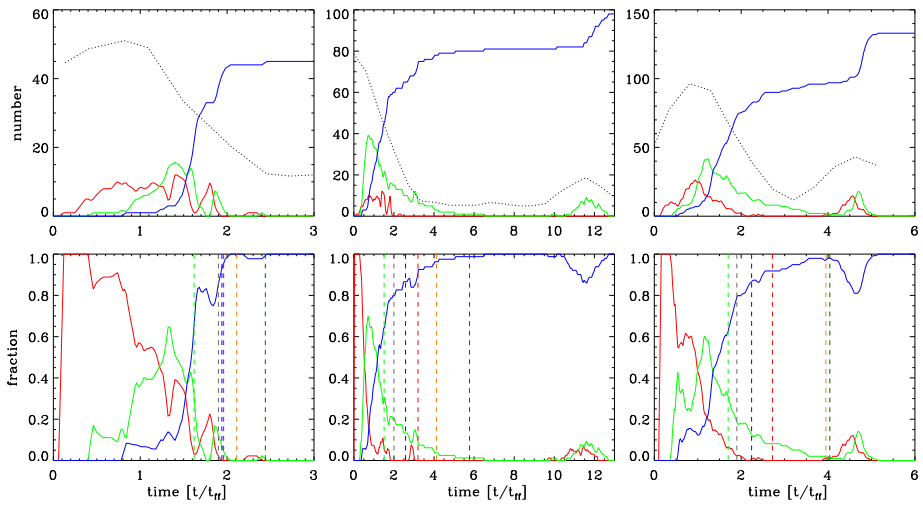

Figure 7.3: The temporal evolution of the fractions of YSO classes for three models: M2k4 (left), M6k2a (middle), and M10k2 (right), *upper panel:* absolute numbers, *lower panel:* relative numbers. Red line: Class 0, green line: Class 1, blue line: Class 2+3, dotted line: prestellar cores (only shown in the upper panel). The abscissa gives the time in units of the global free-fall time. The zero point of the timescale corresponds to the time when gravity is "switched on". Note the different intervals covered in the models. The vertical lines in the lower panel indicate the time τ, when the model shows the best agreement with the observations of Serpens (green), NGC 7129 (grey), Taurus and IC 1396A (blue), ρ Ophiuchi (red), Cha I (orange), and IC 348 (dark green). Note, because of similar relative YSO numbers the best-fit evolutionary times for Taurus and IC 1396A are essentially indistinguishable.

a similar, but shifted peak of Class 1 objects. In the models with higher turbulence, the kinetic energy exceeds the gravitational one and the system is formally supported on global scales. Collapse only occurs locally in the shock compressed cloud clumps. The formation of Class 0 objects extends over a longer period (a few free-fall times) and in some cases there is a second burst of star formation, following an increase of the number of prestellar cores, at a later time as in model M6k2a or M10k2. This second peak is not considered for the comparison with the observations, though.

We count the numbers of objects in the particular classes and compare the relative numbers to the observational values from Table 7.1. We consider the entire observed population including more dispersed objects. Due to the use of periodic boundary conditions those are also included in the models.

The time τ of the best correspondence between observations and models is

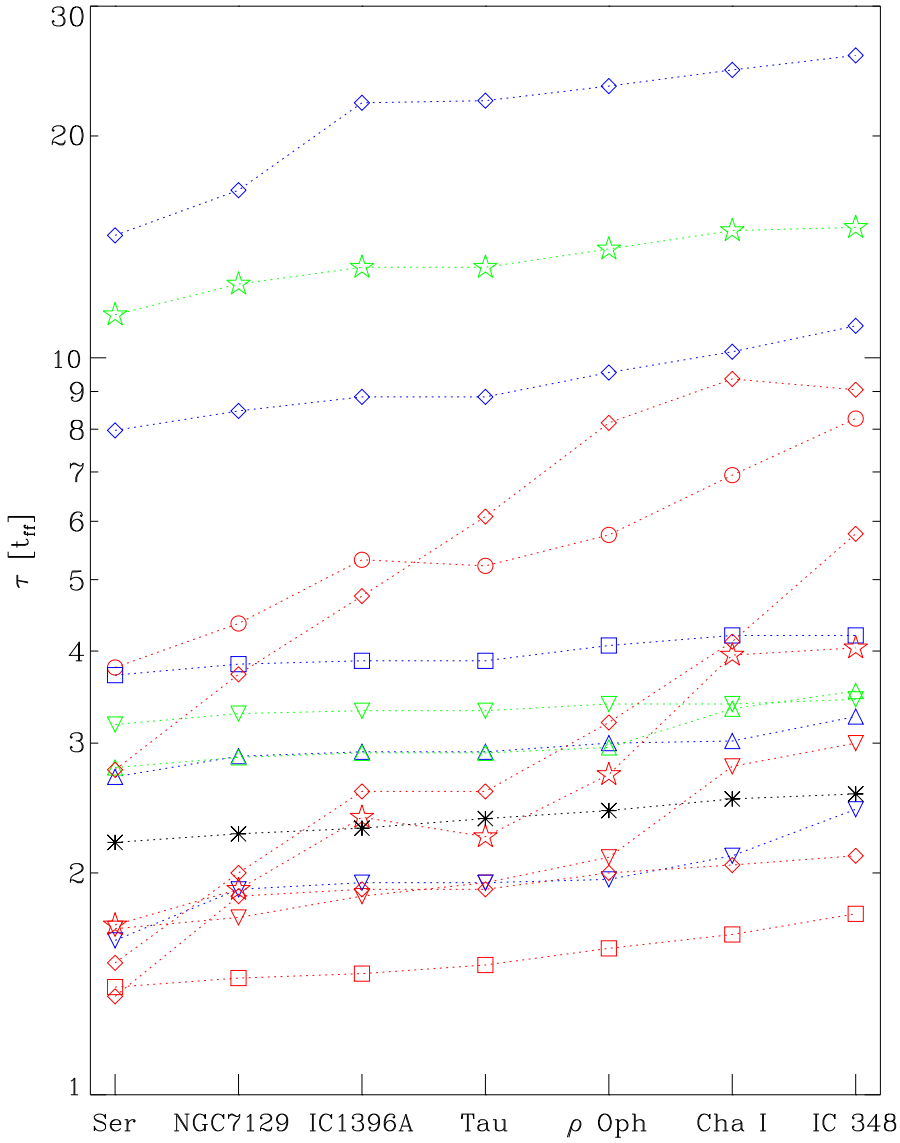

Figure 7.4: The time τ of the best correspondence between models and observations (in units of the global free-fall time $\tau_{\rm ff}$) for the seven investigated clusters. The symbols denote the parameters of the models: $\mathcal{M} = 0.1$ (circles), $\mathcal{M} = 0.5$ (triangles), $\mathcal{M} = 2$ (triangles down), $\mathcal{M} = 3.2$ (squares), $\mathcal{M} = 6$ (diamonds), $\mathcal{M} = 10$ (stars); $1 \leq k \leq 2$ (red), $3 \leq k \leq 4$ (blue), $7 \leq k \leq 8$ (green). The Gaussian collapse models are displayed as asterisks.

determined when the weighted root mean square of the differences

$$\sigma(t) = \sqrt{\frac{\frac{1}{2}\sum_{i=0}^{2} |n_i^{\mathrm{o}} - n_i^{\mathrm{m}}(t)|^2 \omega_i}{\sum_{i=0}^{2} \omega_i}} \tag{7.1}$$

becomes a minimum. The relative number of young stars in Class i (0, 1, 2) from observations is expressed as n_i^{o} and n_i^{m} denotes the relative number of YSOs in Class i from the models. The factor ω_i is a weighting factor, introduced to account for the possible scatter due to small number statistics in both, the observations and the models. The weighting factor is set to $\omega_i = \sqrt{n_i^{\mathrm{o}} \cdot n_i^{\mathrm{m}}}$.

The time τ is shown in the lower panel of Fig. 7.3 and displayed for all models in Fig. 7.4. In general, Serpens is fitted worse than the other clusters. The mean minimal deviation of all models is $\langle\sigma_{\mathrm{min}}\rangle = 0.005$ for ρ Oph and Cha I, $\langle\sigma_{\mathrm{min}}\rangle = 0.008$ for Taurus, $\langle\sigma_{\mathrm{min}}\rangle = 0.010$ for NGC 7129, IC 1396A, and IC 348, and $\langle\sigma_{\mathrm{min}}\rangle = 0.020$ for Serpens. In all cases $\sigma(t)$ has a clearly defined minimum. The scatter of τ is high. Its value varies from about 1.5 to 25 free-fall times for the different models, making it impossible to determine the actual ages of the clusters accurately. However, all models show the same sequence: τ(Ser) < τ(NGC 7129) < τ(IC 1396A) ≤ τ(Tau) < τ(ρ Oph) < τ(Cha I) < τ(IC 348). In four models the age of IC 1396A is slightly smaller than that of Taurus, in the other models the values are identical. Taking into account the second star-formation burst in the models M6k2a and M10k2 increases the ages of the older clusters, but it does not change the overall order. Thus, independent of the applied model, Serpens is the youngest cluster, NGC 7129 the second youngest cluster, Cha I the second oldest, and IC 348 the most evolved cluster, while Taurus and IC 1396A are at the same intermediate evolutionary stage. However, the relative numbers of Class 0 and 1 objects in NGC 7129 and IC 1396A may be overestimated due to possible observational biases introduced by the *Spitzer Space Telescope*, as discussed in § 7.1.6. These clusters may thus appear younger relative to the other ones. The fact that $\sigma(t)$ always has one well-defined minimum and that all models produce the same evolutionary sequence independent of the initial conditions, supports a scenario of a single "burst" of uninterrupted, rapid star formation. This is in agreement with other theoretical and observational findings of star formation timescales and molecular cloud lifetimes (see e.g. Hartmann et al. 2001; Ballesteros-Paredes & Hartmann 2006). Several successive "bursts" of star formation within the cloud region are likely to alter the picture and make a determination of the age from the observed number ratios difficult.

7.4 Star Formation Efficiency

Figure 7.5 shows the star formation efficiency (the ratio of the mass accreted by the young stars to the total mass of the gas) at the time τ versus the Mach number of

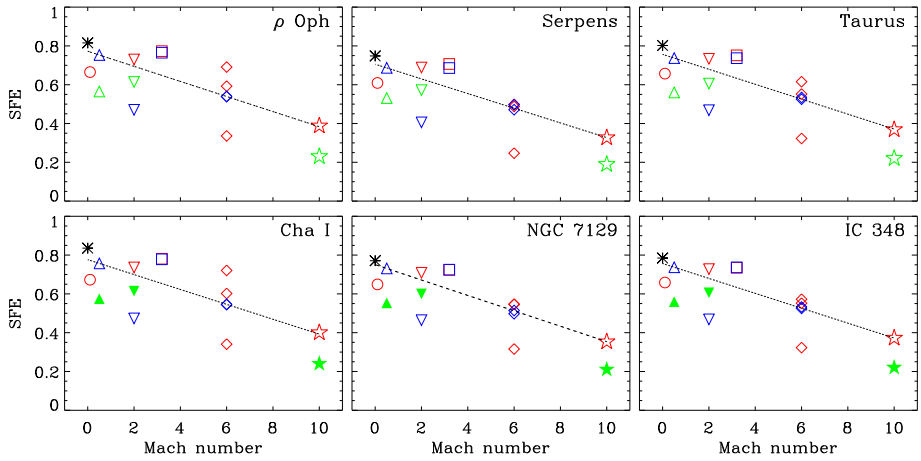

Figure 7.5: The star formation efficiency at time τ plotted versus the Mach number of the models. The symbols are the same as in Fig. 7.4. The dotted lines show a linear fit to the data.

the models for six of the seven clusters. We find an inverse correlation of the SFE with the Mach number (false alarm probability $\leq 0.5\%$). This is consistent with the theoretical findings by Klessen et al. (2000) and Heitsch et al. (2001a), and probably due to the fact that in high-Mach number turbulence less mass is available for collapse at the sonic scale (Vázquez-Semadeni et al. 2003). A linear fit is applied to the data and shown in Fig. 7.5. There is no correlation with the driving wave number. If we interpret the measured velocity dispersions in the clusters as the result of turbulence, we can estimate the SFEs at time τ for the particular Mach numbers from Fig. 7.5. In the case of ρ Oph this requires to extrapolate the fit line beyond $\mathcal{M} = 10$. The SFE is ~ 0.27 in ρ Oph, ~ 0.45 in NGC 7129, ~ 0.56 in IC 348, and between 0.60 and 0.65 in Serpens, Taurus, and Cha I. (Lacking information on the velocity dispersion in IC 1396A, the corresponding SFE cannot be calculated.) These values are significantly higher than the measured SFEs, which are only around 0.1. (No information is available on the SFEs of IC 348 and NGC 7129, but we expect them to be in the range of the other clusters.) Only in the case of ρ Oph the SFE of the models is in the range of the SFE measured. The main reasons for this discrepancy are probably the limitation of the gas reservoir and the neglect of outflows and feedback mechanisms as well as of magnetic fields in the simulations. Bipolar outflows limit the local SFE, because the protostellar jet will carry a certain fraction of the infalling material away, furthermore, its energy and momentum input will affect the the protostellar envelope and may partially prevent it from accreting onto the protostar (e.g. Adams & Fatuzzo 1996). The presence of magnetic fields would also retard the conversion of gas into stars (for current simulations see Heitsch et al. 2001a; Vázquez-Semadeni et al. 2005; Li & Nakamura 2004).

Table 7.2: The ratio of prestellar cores to the total number of YSOs at time τ for three models and the observations.

Region	M2k4	M6k2a	M10k2	Observations
ρ Oph	0.30	0.10	0.10	0.47
Serpens	0.79	0.06	0.74	0.39
Taurus	0.32	0.09	0.22	0.25
Cha I	0.18	0.11	0.82	< 0.39

7.5 Prestellar Cores

As an additional test, the numbers of prestellar cores are analysed as described in § 3.5 for the three models shown in Fig. 7.3 and compared to the four star-forming regions, where information on the number of prestellar cores is available. The ratios of the number of prestellar cores to the total number of YSOs ($n_{\rm psc}/n_*$) at time τ are listed in Table 7.2 together with those values from the observations (calculated from Table 7.1). The observed ratio in Taurus are roughly represented by models M2k4 and M10k2, but for the other regions the models produce either a much higher or much lower ratio. We intended to check if $n^{\rm o}_{\rm psc}/n^{\rm m}_{\rm psc}$ allows us to draw conclusions about the number of prestellar cores that actually collapse and form stars. This seems not to be possible on the basis of the current analysis. In addition, defining a prestellar core is rather difficult, both from an observational and a theoretical point of view. This adds another level of uncertainty to results based on prestellar core statistics.

7.6 Conclusions

We analysed the temporal evolution of the fractions of YSO classes in different gravoturbulent models of star formation and compared it to observations of star-forming clusters. The observed ratios of Class 0, 1, 2/3 objects in ρ Ophiuchi, Serpens, Taurus, Chamaeleon I, NGC 7129, IC 1396A, and IC 348 can be reproduced by the simulations, although the time when the observations are best represented varies depending on the model. Nevertheless, amongst the clusters with good observational sampling we always find the following evolutionary sequence of increasing age: Serpens, Taurus, ρ Oph, Cha I, and IC 348.

We find an inverse correlation of the star formation efficiency with the Mach number. However, our models fail to reproduce the observed SFEs for most of the clusters. This is probably due to the lack of a sufficiently large gas reservoir in the simulations and the neglect of energy and momentum input from bipolar outflows and/or radiation from young stars. Only the SFE in ρ Oph is reproduced. This region is characterised by very high turbulent Mach numbers. The fact that our simple gravoturbulent models without feedback are able to reproduce the right

number ratios of YSOs for $\mathcal{M} \simeq 10$ suggests that protostellar feedback processes may not be important in shaping the density and velocity structure in star-forming regions with very strong turbulence and argues for driving mechanisms external to the cloud itself (see also the discussion in Ossenkopf & Mac Low 2002 and Mac Low & Klessen 2004).

The relative numbers of YSOs can reveal the evolutionary status of a star-forming cluster only with respect to other clusters, as the absolute age is difficult to estimate. Better agreement between models and observations requires a better consideration of environmental conditions like protostellar outflows and magnetic fields in the simulations. A larger observational sample, achieved by complete censuses of more star-forming regions, is also desirable.

Chapter 8

The Structures of Young Star Clusters*

Understanding the formation and evolution of young stellar clusters requires quantitative statistical measures of their structure, which may give important clues to the formation process: A young cluster might still bear the imprint of the physical process(es) that created it and will likely reflect the underlying structure of the dense molecular gas. There are two basic types of clusters with regard to their structure (see e.g. Lada & Lada 2003): (1) Hierarchical clusters show a stellar surface density distribution with multiple peaks and possible fractal substructure; (2) centrally condensed clusters exhibit highly centrally concentrated stellar surface density distributions with relatively smooth radial profiles that can be described in good approximation by simple power-law functions (e.g. $\rho(r) \propto r^{-\alpha}$).

Different methods have been used to describe the clustering properties of star clusters, e.g. the mean surface density of companions (Larson 1995) or spanning trees. Cartwright & Whitworth (2004) presented a review of various statistical methods for analysing the structures of star clusters, and a detailed investigation of both observed and artificially created clusters. We apply their methods to clusters created by numerical simulations of gravoturbulent star formation and investigate the clustering behaviour with time. We extend the analysis of observed clusters by considering different evolutionary classes.

8.1 Statistical Methods

8.1.1 Mean Surface Density of Companions

A wide range of statistical methods has been developed to analyse the structure of star clusters (see Cartwright & Whitworth 2004 for a review). A simple approach is to study the distribution of source separations, as it has been done e.g. by Kaas et al. (2004) for the Serpens cloud core. Larson (1995), extending the analysis by Gomez

*This chapter is based on Schmeja, S., & Klessen, R. S. 2006, A&A, 449, 151

et al. (1993), introduced the mean surface density of companions (MSDC) $\Sigma(\theta)$, a tool that since then has often been used to study star-forming clusters (e.g. Bate et al. 1998; Gladwin et al. 1999; Klessen & Kroupa 2001). The mean surface density of companions specifies the average number of neighbours per square degree on the sky at an angular separation θ for each cluster star:

$$\Sigma(\theta) \equiv \frac{\delta N(\theta)}{2\pi N \theta \delta\theta}. \tag{8.1}$$

Knowing the distance to the cluster, θ can be converted to an absolute distance r to determine $\Sigma(r)$.

8.1.2 Normalised Correlation Length

The physical interpretation of the MSDC can be difficult, and Cartwright & Whitworth (2004) have shown that the normalised correlation length is a better indicator for the clustering behaviour. The normalised correlation length $\bar{s}$ is the mean separation s between stars in the cluster, normalised by dividing by the radius of the cluster, $R_{\rm cluster}$. This radius is defined as the radius of a circle with the same area as the normalised convex hull of the data points (see Appendix A.1). The $\bar{s}$ values are independent of the number of stars in the cluster (Cartwright & Whitworth 2004).

8.1.3 Minimum Spanning Trees

The minimum spanning tree (MST), a construct from graph theory, is the unique set of straight lines ("edges") connecting a given set of points ("vortices") without closed loops, such that the sum of the edge lengths is a minimum (Kruskal 1956; Prim 1957; Gower & Ross 1969; see Appendix B.1 for the mathematical definitions). In astrophysics, minimum spanning trees have been used so far mainly to analyse the structure of galaxy clusters (e.g. Barrow et al. 1985; Adami & Mazure 1999; Doroshkevich et al. 2004). From the MST the normalised mean edge length $\bar{m}$ is derived. Unlike the mean separation length s, the mean edge length m depends on the number of stars in the cluster, therefore it has to be normalised by the factor

$$(A/n)^{1/2} \tag{8.2}$$

(Marcelpoil 1993), where n is the total number of stars and A the two-dimensional area of the cluster. In the three-dimensional case the normalisation factor is

$$(V/n)^{1/3}, \tag{8.3}$$

where V is the volume of the cluster. Area and volume are defined using the normalised convex hull of the data points (see Appendix A.1 for the definition). The normalisation factors are discussed in detail in Appendix B.3.

An additional reducing operation, called *separating*, can be used to isolate subclusters (Barrow et al. 1985). Separating means removing all edges of the MST whose lengths exceed a certain limit. When removing edges from a MST, each remaining subgraph is again a MST of its vortices (Robins et al. 2000).

8.1.4 The combined measure Q

The values $\bar{s}$ and $\bar{m}$, on their own, can quantify, but cannot distinguish between, a smooth large-scale radial density gradient and multiscale fractal subclustering. Dussert et al. (1986) combine the mean edge length m of a MST and its standard deviation $\sigma_{\rm m}$ and use the $(m, \sigma_{\rm m})$-plane to distinguish between different degrees of order in various systems. However, Cartwright & Whitworth (2004) show that this is not sufficient to distinguish between a smooth large-scale radial density gradient and fractal subclustering. Therefore, Cartwright & Whitworth (2004) introduced the parameter

$$Q = \frac{\bar{m}}{\bar{s}}, \tag{8.4}$$

which can provide this distinction. Large Q values ($Q \geq 0.8$) indicate centrally concentrated clusters having a volume density $n(r) \propto r^{-\alpha}$, where Q increases with increasing α (i.e., with increasing degree of central concentration). Small Q values ($Q \leq 0.8$) describe clusters with fractal substructure, where Q decreases with increasing degree of subclustering.

8.1.5 The elongation of a cluster

We also investigate the elongation of the clusters. We define the elongation ξ of a cluster as the ratio of the cluster radius defined by an enclosing circle to the cluster radius derived from the normalised convex hull of the objects. A value of $\xi \approx 1$ describes a spherical cluster, while a value of $\xi \approx 3$ corresponds to an elongated elliptical cluster with an axis ratio of $a/b \approx 10$. See Appendix A.2 for details.

8.2 Observational Data

Our observational data are based on the sample of YSOs in embedded clusters compiled from various sources as discussed in detail in § 7.1. However, in the current analysis only the regions ρ Ophiuchi, Taurus and Serpens will be studied in detail. These are clusters, where sufficient information on the evolutionary classes as well as on the positions is given in the literature. IC 348 and Chamaeleon I are used for determining additional clustering parameters. For further details on the compilation of the original sample see § 7.1. The numbers of objects are given in Table 8.1, the positions of all YSOs are plotted in the upper panel of Fig. 8.1. The adopted distances used to determine the absolute values of $\bar{s}$ and $\bar{m}$ are 140 pc for ρ Oph (Bontemps et al. 2001), 260 pc for Serpens (Kaas et al. 2004), 140 pc for Taurus (Hartmann 2002), 315 pc for IC 348 (Luhman et al. 2003), and 150 pc for Cha I (Haikala et al. 2005).

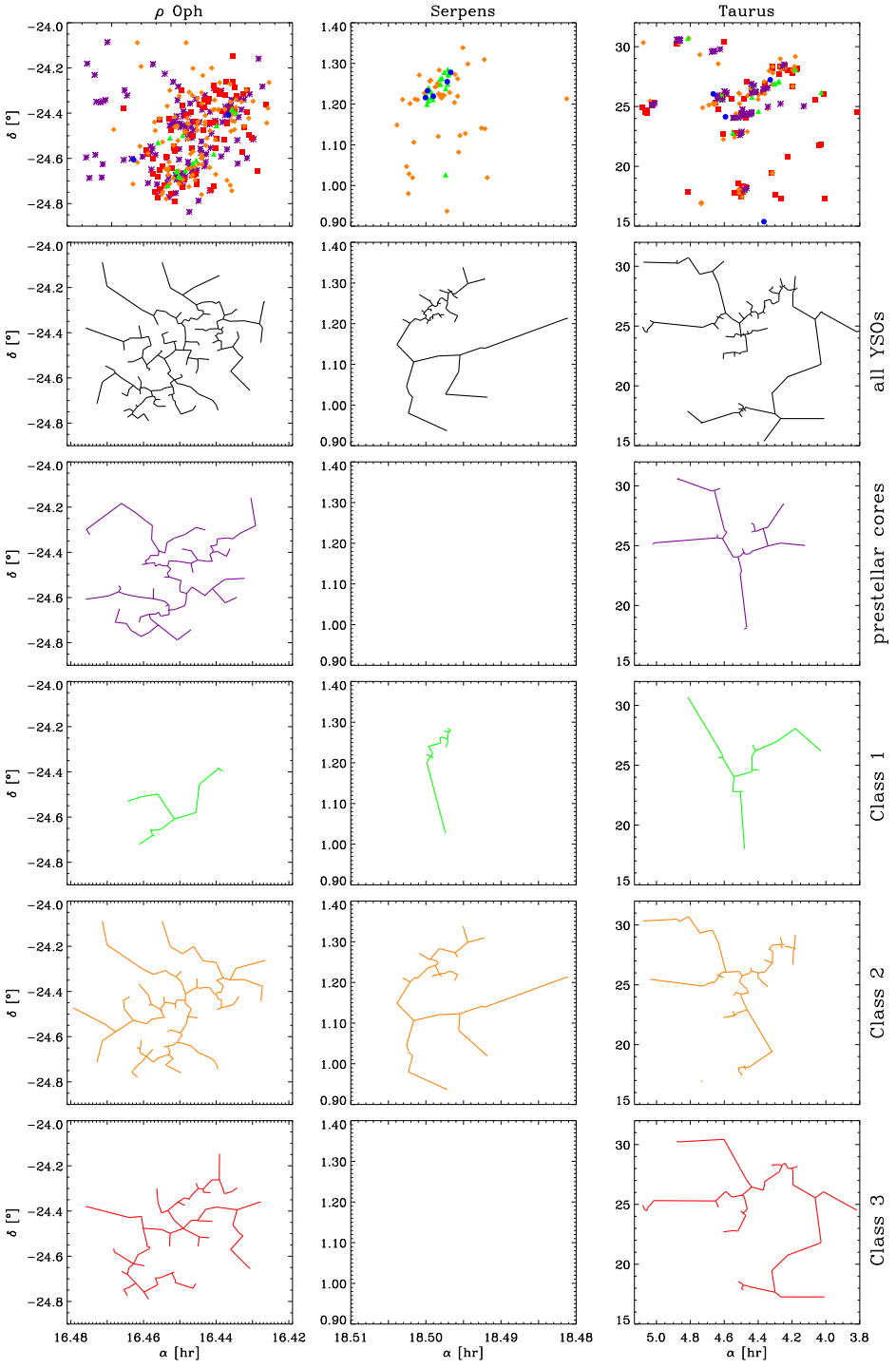

Figure 8.1: Upper panel: Observational data for the star-forming clusters ρ Ophiuchi, Serpens, and Taurus. Blue: Class 0, green: Class 1, orange: Class 2, red: Class 3, violet: prestellar cores. References see text. Other panels: The MSTs of the same regions of all YSOs (second row), prestellar cores (third row), and Class 1, 2, 3 objects (fourth, fifth and sixth row).

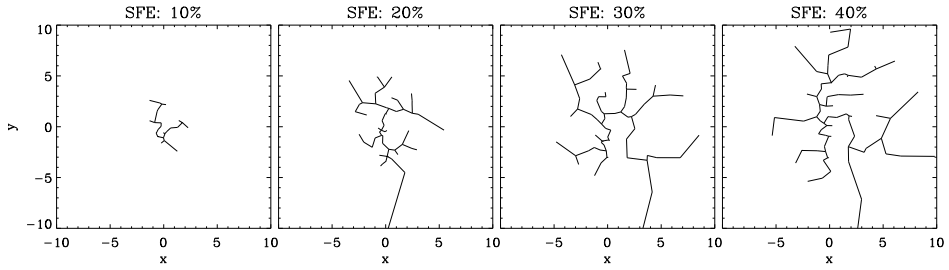

Figure 8.2: The 2D minimum spanning tree for the YSOs of model M6k4a projected into the xy-plane at a star formation efficiency of 10%, 20%, 30% and 40% (from left to right), demonstrating the expansion of the cluster.

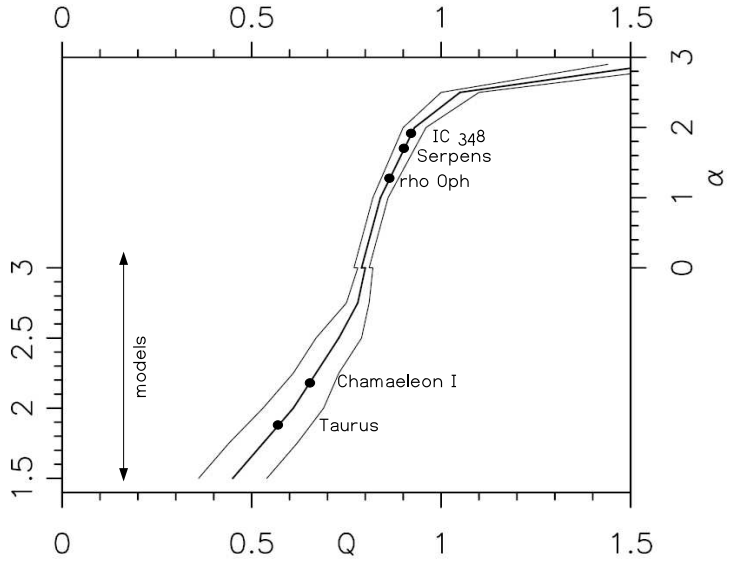

Figure 8.3: The relation between Q and the fractal dimension D (left-hand axis) and the radial density exponent α (right-hand axis), respectively (taken from Cartwright & Whitworth 2004). Overlayed are the Q values for the observed clusters and the range of the models, allowing the determination of the corresponding D or α value from the ordinate.

Table 8.1: Clustering measures and numbers for the observed star-forming regions for prestellar cores (p), Class 1, 2, 3 sources, and all YSOs. (Note that the total number of YSOs is larger than the sum of objects in the individual classes, because it contains Class 0 sources and objects with unclear classification not considered in the analysis of the individual classes.) For details see the discussion in § 8.4.1.

Region	Class	n	s [′]	s [pc]	m [′]	m [pc]	$\bar{s}$	$\bar{m}$	Q	$\bar{s}^*$	$\bar{m}^*$	Q^*	ξ
ρ Ophiuchi	p	98	20.45	0.83	2.71	0.11	0.67	0.55	0.82	0.49	0.40	0.81	1.36
	1	15	11.82	0.48	3.15	0.13	1.13	0.68	0.60	0.77	0.43	0.56	1.47
	2	111	15.86	0.65	2.25	0.09	0.69	0.58	0.83	0.54	0.63	1.15	1.27
	3	77	16.25	0.66	2.53	0.10	0.82	0.63	0.76	0.70	0.66	0.93	1.17
	all	205	15.63	0.64	1.67	0.07	0.67	0.57	0.85	0.53	0.45	0.85	1.28
Serpens	1	19	3.43	0.26	1.12	0.09	0.99	0.82	0.83	0.27	0.22	0.79	3.61
	2	18	7.85	0.59	1.74	0.13	0.74	0.61	0.82	0.52	0.42	0.80	1.42
	all	80	5.98	0.45	1.06	0.08	0.60	0.54	0.90	0.37	0.32	0.89	1.63
Taurus	p	52	281.0	11.47	45.88	1.87	0.77	0.48	0.62	0.59	0.36	0.61	1.29
	1	25	265.6	10.84	73.18	2.98	0.83	0.60	0.73	0.59	0.41	0.70	1.39
	2	108	333.5	13.62	34.30	1.40	0.69	0.41	0.59	0.43	0.54	1.26	1.61
	3	72	414.4	16.96	52.99	2.16	0.84	0.51	0.60	0.77	0.63	0.82	1.09
	all	197	356.8	14.58	25.98	1.06	0.67	0.39	0.58	0.46	0.27	0.58	1.45
IC 348	all	288	6.86	0.63	0.66	0.06	0.56	0.52	0.93	0.49	0.45	0.92	1.16
Chamaeleon I	all	180	41.51	1.81	3.74	0.16	0.55	0.37	0.68	0.50	0.34	0.68	1.32

8.3 Application to the Data

We construct the MST following Prim's (1957) algorithm (see Appendix B.2). For both the observations and the models, the parameters $\bar{s}$, $\bar{m}$ and Q are computed for the different evolutionary classes independently (provided, there is a sufficiently large number of YSOs of that class) as well as for the entire cluster. In no region is the number of Class 0 sources large enough to be included. In addition, these parameters are determined at frequent timesteps of the simulations to obtain the temporal evolution of the parameters. In the case of $\bar{m}$, this requires to construct the MST anew at every chosen timestep. As an example, Fig. 8.2 shows the MST of one model at different evolutionary stages. While the parameters $\bar{s}$, $\bar{m}$ and Q are calculated using the normalisation factor given above, $\bar{s}^*$, $\bar{m}^*$ and Q^* are determined with the normalisation factor and cluster radius of Cartwright & Whitworth (2004) (see also the discussion in the Appendix).

As shown by Cartwright & Whitworth (2004), the effect of binary stars on the clustering parameters is not negligible. Since binaries create very short edge lengths, a large fraction of binaries will significantly reduce the mean edge length $\bar{m}$ (and as a consequence also change Q). As the binaries are not part of the clustering regime, their influence on the clustering parameters has to be minimized. While for most of the clusters this is not relevant, Taurus is known to have a large binary population. Thus we removed the known binary companions from our sample of YSOs in Taurus.

We calculate the clustering parameters $\bar{s}$, $\bar{m}$, Q, and ξ for the model cluster in three dimensions, and, in order to compare them with the apparent two-dimensional observational data, projected into the xy-, xz-, and yz-plane. The positions of the stars are corrected for the periodic boundary conditions. Only objects inside a box of ten times the side length of the original computational box are considered, if there are any objects outside this volume, we assume that they have left the cluster and are not relevant for the clustering process.

In the initial stages of the cluster as a whole, and of the individual evolutionary classes, the number of objects is of course rather low. In such cases the statistical analysis may not be very meaningful and has to be taken with a grain of salt.

8.4 Discussion

8.4.1 Observations

Table 8.1 lists the clustering measures introduced in § 8.1 for the observations. Columns 4 to 7 list the (non-normalised) mean separation of objects and mean MST edge lengths in arcminutes and parsec. Columns 8 to 10 give the parameters $\bar{s}$, $\bar{m}$ and Q, while Columns 11 to 13 list the same values calculated using the normalisation of Cartwright & Whitworth (2004) ($\bar{s}^*$, $\bar{m}^*$, Q^*). The last column gives the elongation ξ. The values of $\bar{s}^*$, $\bar{m}^*$ and Q^* agree with the values given by Cartwright & Whitworth (2004), except for $\bar{s}^*$ and $\bar{m}^*$ of Taurus (interestingly,

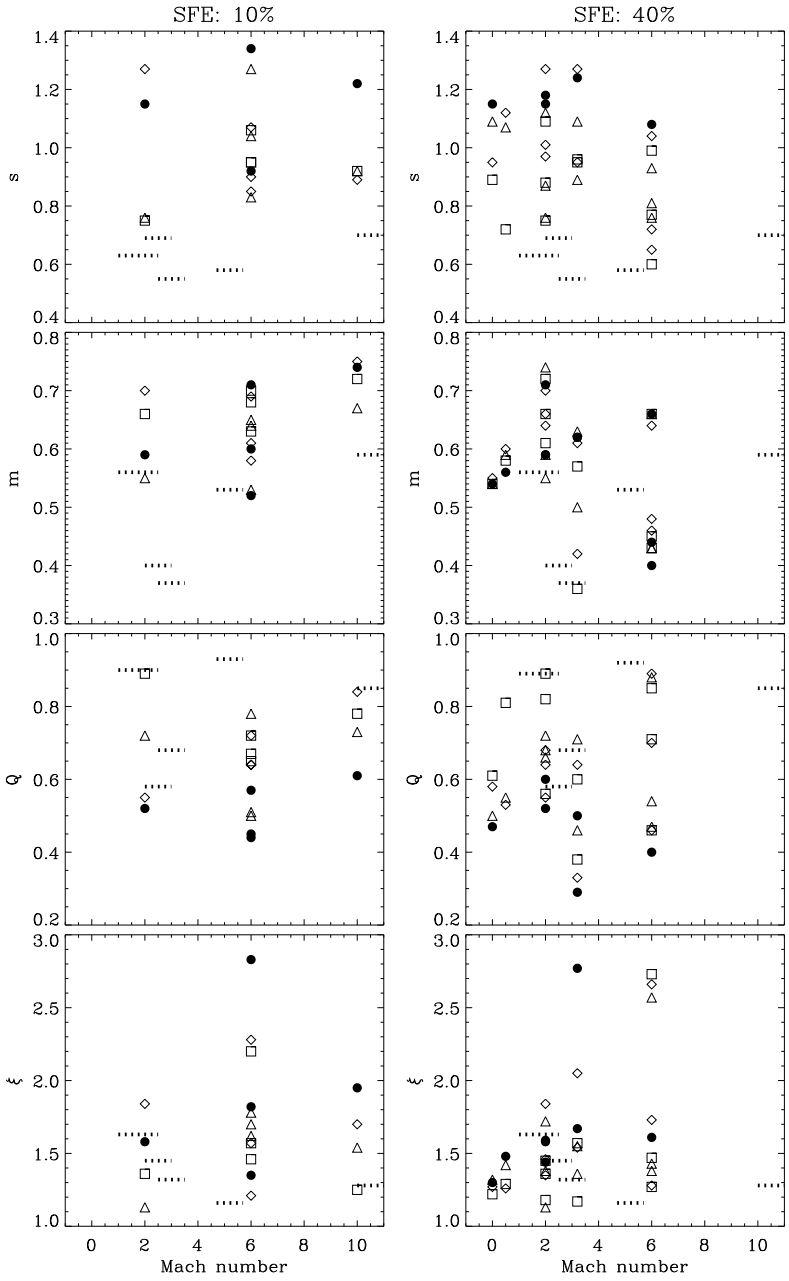

Figure 8.4: The clustering parameters $\bar{s}$, $\bar{m}$, Q, and ξ for all models at a SFE of 10% (left panel) and 40% (right panel), plotted versus the Mach number. Shown are the values for the projection into the xy-, xz-, and yz-plane (diamonds, triangles and squares, respectively), and for the 3D analysis (filled circles). The horizontal lines show the corresponding values from the observational data for Serpens, Taurus, Chamaeleon I, IC 348, and ρ Oph (from left to right).

however, our Q^* is the same as theirs). We attribute small differences to the slightly different underlying samples, and the discrepancy for Taurus to the different treatment of binaries. Due to the different definition of the radius/area of the cluster, $\bar{s}^*$ and $\bar{m}^*$ differ significantly from $\bar{s}$ and $\bar{m}$, while Q and Q^* are roughly the same, in particular for large samples (see the discussion in Appendix B.3). Taurus and Chamaeleon I have substructure, while ρ Oph and IC 348 are centrally concentrated clusters (see the discussion in Cartwright & Whitworth 2004). Serpens (not discussed by Cartwright & Whitworth 2004) has $Q = 0.90$, corresponding to a central concentration with a radial density exponent $\alpha \approx 1.9$, similar to IC 348.

The linear distances s and m are in the same range for ρ Oph, Serpens, and IC 348, significantly larger for Chamaeleon I, and about an order of magnitude larger in the case of Taurus, confirming the notion that Taurus represents a somewhat less clustered mode of star formation. However, when considering only the central part of the Taurus region, the values decrease significantly to $s = 3.05\,\mathrm{pc}$ and $m = 0.49\,\mathrm{pc}$. The latter is comparable to the 0.3 pc estimated as the average distance to the nearest stellar neighbour in the central region of Taurus by Gomez et al. (1993) and Hartmann (2002).

The mean separation s increases with the evolutionary class for all three clusters investigated in this regard, reflecting the expansion of the cluster, which can also be seen in Fig. 8.1. While Class 0 protostars are formed in the high-density central regions, more evolved YSOs already had time to move to more remote regions (see also Kaas et al. 2004). Note that the prestellar cores do not fit into this sequence, as they are distributed over an area roughly as large as the entire cluster. Thus we speculate that not all objects identified as prestellar cores will eventually form stars. Only in the central parts of the cluster may the density be high enough to make the cores collapse. This is consistent with the findings of Vázquez-Semadeni et al. (2005) that a significant number of "failed cores" should exist, which may redisperse and which may correspond to the observed starless cores.

The elongation of the clusters ranges from $\xi = 1.16$ for the almost perfectly spherical cluster IC 348 to $\xi = 1.63$ for Serpens. The ξ value can differ significantly for subclusters, e.g. the filamentary central part of the Taurus region has an elongation of $\xi = 1.83$.

8.4.2 Models

We compute the clustering parameters $\bar{s}$, $\bar{m}$, Q, and ξ for all models and compare them with each other as well as with those from the observations. Figure 8.4 shows the clustering parameters for all models, sorted by the Mach number at a star formation efficiency (SFE) of 10% and 40%. The clustering parameters of the observed clusters (from Table 8.1) are shown as horizontal lines at their Mach number (see § 7.1). The $\bar{s}$ and $\bar{m}$ values of the models are in general significantly larger than those from the observations. A particularly large discrepancy is noted when the model cluster is strongly elongated. A large ξ value reduces the normalisation factor and increases $\bar{s}$ and $\bar{m}$. While the observed clusters show rather

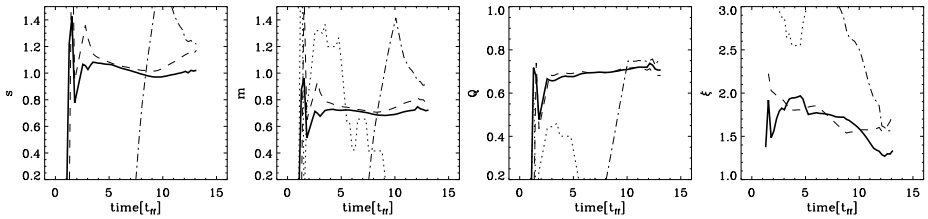

Figure 8.5: The temporal evolution of the 3D clustering parameters $\bar{s}$, $\bar{m}$, Q, and ξ for one model (M6k4a), dotted: Class 0, dashed: Class 1, dash-dotted: Class 2/3, solid line: entire cluster.

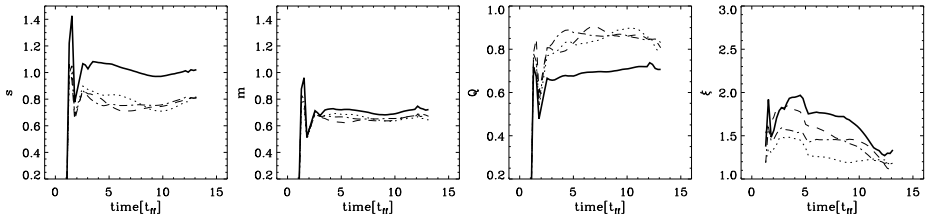

Figure 8.6: The temporal evolution of the clustering parameters $\bar{s}$, $\bar{m}$, Q, and ξ of the model M6k4a for the 3D analysis (solid line) and for the projection into the xy- (dotted), xz- (dashed), and yz-plane (dash-dotted).

moderate elongations in the range $1.1 < \xi < 1.6$, in some models the stars form in a single filament with an elongation $\xi > 3$. Model clusters with elongations in the range of the observations show also a good agreement in the other parameters. For example, the fairly spherical cluster of model M6k4a (shown in Fig. 8.2) has (at 40% SFE and projected into the xy-plane) an elongation of $\xi = 1.28$ and clustering parameters of $\bar{s} = 0.72$, $\bar{m} = 0.64$, and $Q = 0.89$. These values are almost identical to those of ρ Ophiuchi ($\xi = 1.28$, $\bar{s} = 0.70$, $\bar{m} = 0.59$, $Q = 0.85$). For the other projections the values differ by less than 8%. Most of the Q values, which are independent of the area, lie in the same range as those from the observations. We find no correlation of the clustering parameters with the properties of the turbulent driving (Mach number or wave number k) of the models. Neither do the values from the observations show any correlation with the Mach number. Thus we conclude that if there is any systematic influence of the turbulent environment on the clustering behaviour, it is only existent in the earliest phase of cluster formation, before it is smoothed out by the motions of the individual protostars (see also Bate et al. 1998).

Fig. 8.2 shows the MST of a model cluster (M6k4a) at different evolutionary stages and reveals the expansion of the cluster. We analyse the temporal evolution of the clustering parameters: $\bar{s}(t)$, $\bar{m}(t)$, $Q(t)$, $\xi(t)$ in all models. As an example, Fig. 8.5 shows this sequence for said model M6k4a. The general behaviour is the

same for all models: $\bar{s}$ and $\bar{m}$ decline with time, while Q increases slowly or stays at a roughly constant value. This evolution is shown by the entire cluster as well as by the individual classes, although in later stages the latter values might fall to zero as the number of objects in a particular class becomes zero. Decreasing $\bar{s}$ and $\bar{m}$ values indicate that star formation sets in in different, rather dispersed regions of the cloud. The cluster becomes denser as more and more gas is turned into protostars. New stars are formed faster than the cluster expands. According to the Q values, the cluster evolves slowly from fractal subclustering to a more centrally concentrated cluster, although in no model does Q rise significantly above the 'dividing value' of 0.8. This again shows that the cluster builds up from separate groups which will grow into a single, more centrally concentrated cluster, as it was also found by Bonnell et al. (2003) and Clark et al. (2005).

8.4.3 The Effect of Projection

Looking at the two-dimensional projections of the 3D model clusters does not significantly change the picture as a whole. The individual $\bar{s}$, $\bar{m}$ and Q values can indeed differ for the projection into the xy-, xz-, and yz-plane, but the qualitative behaviour of the evolution is more or less the same, independent of the projection (Fig. 8.6). While the $\bar{s}_{3D}$ and $\bar{m}_{3D}$ values usually are higher than the values of the projections, Q_{3D} tends to be lower than the values of the projections. The investigation of several hundred randomly created clusters shows that $\bar{s}_{3D}$ is always expected to be larger than the value for the projections ($\bar{s}_{3D}/\bar{s}_{2D} \approx 1.2$), while the $\bar{m}$ values can be in the range $0.95 \lesssim \bar{m}_{3D}/\bar{m}_{2D} \lesssim 1.4$ with a mean value of 1.1. In the extreme case, Q_{3D} can differ by up to 30% from the 2D value. Note that the physical interpretation of Q as given by Cartwright & Whitworth (2004) is based on the two-dimensional analysis. Therefore, for an interpretation of the numerical values (and not only the trend) of Q, the projected values have to be used.

The elongation measure ξ, on the other hand, depends strongly on the projection. Obviously, an elongated, filament-like structure seen from the side will look spherical when observed along its major axis. In the case of the models the three-dimensional value of ξ can be used to describe the true shape of the cluster. A large scatter in the ξ_{2D} values means a high ξ_{3D} value and vice versa.

8.4.4 The Effect of Separating

We separate the observed clusters by successively removing all MST edges with lengths l larger than $l + 3\sigma_m$, $l + 2\sigma_m$, $l + \sigma_m$, and $l + 0.5\sigma_m$, where σ_m denotes the standard deviation of the mean edge length of the MST. This process is demonstrated for the Taurus star-forming region in Fig. 8.7. When we compare all three regions with sufficient data, we see that for Serpens and Taurus only solitary stars in the outskirts of the cluster are removed, while the central part of the cluster stays connected. However, the more homogeneous ρ Oph cluster breaks down in two roughly equally large clusters at the last step. In Fig. 8.8 we show the clustering

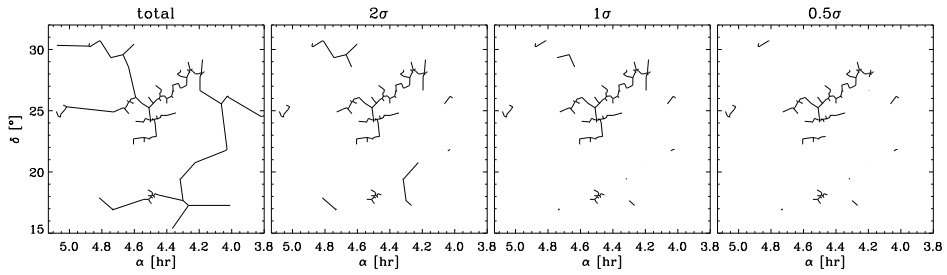

Figure 8.7: The MST of the Taurus cluster as a whole (left panel) and separated at $l + 2\sigma_{\rm m}$, $l + \sigma_{\rm m}$, and $l + 0.5\sigma_{\rm m}$ (from left to right).

parameters of the largest remaining subcluster (i.e., the one containing the largest number of stars after each level of separation). The parameter Q is less affected by the separating procedure than $\bar{s}$ and $\bar{m}$. Significant changes are only seen when large parts of the cluster are excluded (as in the step from 1 to 0.5σ for ρ Oph, when the cluster breaks up into two large subclusters). The elongation measure ξ varies significantly with the level of separation. For example, the remaining subcluster in Taurus shows a filamentary structure and thus a larger ξ ($\xi = 1.83$) than the cluster as a whole.

8.5 Conclusions

We show that the normalised mean correlation length $\bar{s}$ and the mean edge length of the minimum spanning tree $\bar{m}$, and in particular the combination of both parameters, Q, as proposed by Cartwright & Whitworth (2004), are very useful tools to study the structures of star clusters, both observed ones and those from numerical simulations. We refine the definition of the cluster area by using the normalised convex hull rather than a circular or rectangular area around the objects. Unlike $\bar{s}$ and $\bar{m}$, the parameter Q is independent of the definition of the area of the cluster. In addition, it is less affected when removing stars from the cluster by separating the MST.

We introduce a new measure ξ for the elongation of a cluster. It is defined as the ratio of the cluster radius determined by an enclosing circle to the cluster radius derived from the normalised convex hull. This is a stable statistical measure not influenced by fractal substructure, which could also be applied to the filamentary structure of molecular clouds.

The mean separation s increases with the evolutionary class, reflecting the expansion of the cluster. The prestellar cores do not follow that sequence, leading us to the speculation that not all objects classified as prestellar cores will eventually form stars. The clustering values of the models lie roughly in the same range as those from observed clusters. A particularly good agreement is reached when the model clusters have similar elongation values ξ to the observed ones. No corre-

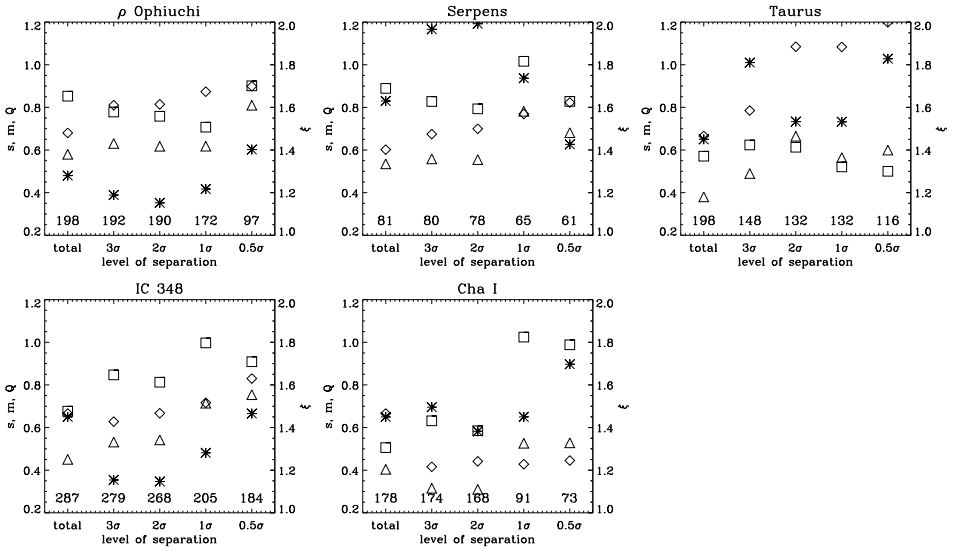

Figure 8.8: The clustering parameters $\bar{s}$ (diamonds), $\bar{m}$ (triangles), Q (squares), and ξ (asterisks; scale on the right-hand axis) of the largest remaining subcluster at different levels of separation. The numbers along the abscissa give the number of YSOs contained in the particular subcluster.

lation with the Mach number or the wave number of the turbulence is found. We conclude that possible influences of the turbulent environment on the clustering behaviour are quickly smoothed out by the velocity dispersion of the young stars.

The temporal evolution of the clustering parameters shows that the star cluster builds up from several subclusters and evolves to a more centrally concentrated state. New stars are formed faster than the cluster expands. The projection of the 3D models into a 2D plane changes the clustering parameters, but not the general behaviour with time.

Chapter 9

Summary and Perspectives

'The Ultimate Question?'
'Yes!'
'Of Life, the Universe, and Everything?'
'Yes!'
Deep Thought pondered for a moment.
'Tricky,' he said.

– Douglas Adams, The Hitchhiker's Guide to the Galaxy

In this thesis, a large set of numerical simulations of gravoturbulent star formation have been analysed in detail and compared to observational data. Twenty-four models covering a wide range of environmental conditions from low to high turbulent velocities and different driving scales with a total number of 1325 protostars have been investigated in many respects. The models cover the entire spectrum of observed star-forming regions, ranging from inefficient and isolated star formation to the fast and efficient build-up of stellar clusters. We investigated the properties of individual protostars (mass accretion rates, $T_{\rm bol}/L_{\rm bol}/M_{\rm env}$) as well as those of entire clusters (number ratios, structure). Despite their indubitable limitations, the simulations are able to reproduce those properties without contradictions. Considering the fact that the observations contain (partly large) uncertainties and biases as well, we can speak of a fairly good agreement. It is safe to state that gravoturbulent fragmentation is an adequate approach to explain the formation of stars, which is clearly superior to the so-called "standard theory of star formation", in which star formation is regulated by magnetic fields and slow ambipolar diffusion processes.

In the picture of gravoturbulent fragmentation, star formation is a highly chaotic and localised process. Only a few parameters show a correlation with the properties of the turbulent driving, e.g. the mean mass accretion rate or the star formation efficiency of a cluster.

As demonstrated in § 5, protostellar mass accretion is a highly dynamical and time-variant process. The peak accretion rate, reached during the Class 0 stage shortly after the formation of the protostellar core, can reach values of $\gtrsim 10^4\,{\rm M}_\odot\,{\rm yr}^{-1}$. The maximum accretion rate is approximately one order of magnitude higher than

the constant rate predicted by the collapse of a classical singular isothermal sphere, in agreement with the observations.

A better possibility to compare the model mass accretion rates to observations is converting them to the observables $T_{\rm bol}$, $L_{\rm bol}$, and $M_{\rm env}$. Our newly developed method uses the accretion rates during the Class 0 stage from the simulations as input for an evolutionary scheme. The resulting distribution in the $T_{\rm bol}$-$L_{\rm bol}$-$M_{\rm env}$ parameter space is then compared to observational data of by means of a 3D Kolmogorov-Smirnov test. The highest probability found that the distributions of model tracks and observational data points are drawn from the same distribution is 70%. The method can be easily applied to future larger source samples, different sets of accretion rates or other evolutionary models. An extension of the analysis to Class 1 objects might be worth considering, however, this requires a more sophisticated envelope model or, ideally, radiative transfer modelling.

In the second part of this thesis, the properties of clusters as a whole are investigated. The ratios of Class 0, 1, and 2/3 objects in observed star-forming clusters are compared to the temporal evolution of the gravoturbulent models in order to estimate the evolutionary stage of a cluster. While it is difficult to estimate the absolute age of the clusters, the relative numbers of YSOs reveal the evolutionary status of a cluster with respect to other clusters. We find an evolutionary sequence with Serpens as the youngest and IC 348 as the most evolved of the seven investigated clusters. Again, this method can be easily applied to other observed clusters as well as to different simulations.

The statistical methods presented in § 8.1 turn out to be very powerful tools to analyse the structure of star clusters. In this work, only a handful of observed star-forming regions with a maximum of a few hundred YSOs have been discussed, but the methods can be easily applied to data of other clusters as soon as they become available. The *Spitzer Space Telescope* recently revealed clusters with several hundred up to thousands of YSOs (e.g. Megeath et al. 2005). Such large samples make the use of sophisticated methods to analyse their structure worthwhile. Of particular interest would be the identification of subclusters or the determination and possibly quantification of filaments. Kushnir et al. (2006) recently developed a powerful algorithm to study multi-scale clustering. It permits to detect clusters at different scales, as well as to estimate structural and geometrical properties of the clusters. The application of this method to new observational data as well as to more advanced simulations is a promising next step. Another possible extension is the inclusion of brown dwarves in the analysis in order to address the question of whether they follow the same clustering behaviour as stars. Finally, it would be interesting to compare the structure of a stellar cluster to the structure of the underlying molecular cloud, which requires an adequate method to compare a point source distribution to the continuous distribution of the gas.

Several possible improvements of the simulations have been discussed or already been implemented, e.g. replacing the isothermal equation of state by a polytropic one (Jappsen et al. 2005), increasing the numerical resolution by increasing the number of particles (e.g. Jappsen et al. 2005 with up to 10^7 particles) or by

particle splitting (Kitsionas 2000; Kitsionas & Whitworth 2002), or including outflows and feedback mechanisms (Dale et al. 2005). On the other hand, a better observational sample is needed as well. This requires both, surveys of star formation regions that are as complete as possible and larger, unbiased samples of individual objects, in particular of Class 0 sources. So far, only about 30 objects are unambiguously classified as Class 0 protostars (Froebrich 2005). A recently implemented data base[1] (Froebrich 2005) is supposed to help collecting data of newly identified Class 0 (and eventually Class 1) sources.

[1] http://www.dias.ie/protostars

Appendix A

The Shape of a Cluster

A.1 Radius and Area

For the normalisation of the parameters $\bar{s}$ and $\bar{m}$ the radius and the area (or volume) of the cluster are needed (see Appendix B). Since there is no clearly defined natural boundary of a star cluster, several approaches to determine the cluster area have been used. Cartwright & Whitworth (2004) define the cluster radius as the distance between the mean position of all cluster members and the most distant star, and the area apparently as a circle with the cluster radius: $A = \pi R^2_{\rm cluster}$. Adami & Mazure (1999) define the area used for the normalisation of the MST edge lengths as the maximum rectangle of the point set. However, both methods tend to overestimate the area of the cluster, in particular if the cluster is elongated or irregularly shaped rather than spherical. Therefore, we estimate the area A of the cluster by the convex hull of the data points, normalised by an additional geometrical factor taking into account the ratio of the number of objects inside and on the convex hull:

$$A = m(H)/[1 - (v_{\rm H}/n)] \tag{A.1}$$

(Ripley & Rasson 1977; Hoffman & Jain 1983), where H is the convex hull, $m(H)$ its area, $v_{\rm H}$ the number of vertices of H and n the number of objects. This factor is used since the convex hull by itself tends to be smaller than the true sampling window. To be consistent, we define the cluster radius as the radius of a circle with the area A as defined above. In the three-dimensional case the volume V is defined by the normalised convex hull in the same way as above. The convex hull is computed using the programme *Qhull* (Barber et al. 1996).

Figure A.1 demonstrates that the definition of the cluster area is crucial, since it can differ by a factor of two or more. In the given example of randomly distributed data points, the area of the circle is 46.33, that of the rectangle is 30.40, the area of the convex hull is 24.19, and the normalised area (Eq. A.1) is 24.83. However, for the calculation of the crucial parameter $Q = \bar{m}/\bar{s}$ the size of the radius/area is irrelevant (as long as the area used for the normalisation of $\bar{m}$ depends on the radius used for the normalisation of $\bar{s}$ or vice versa). The radius is cancelled since it is

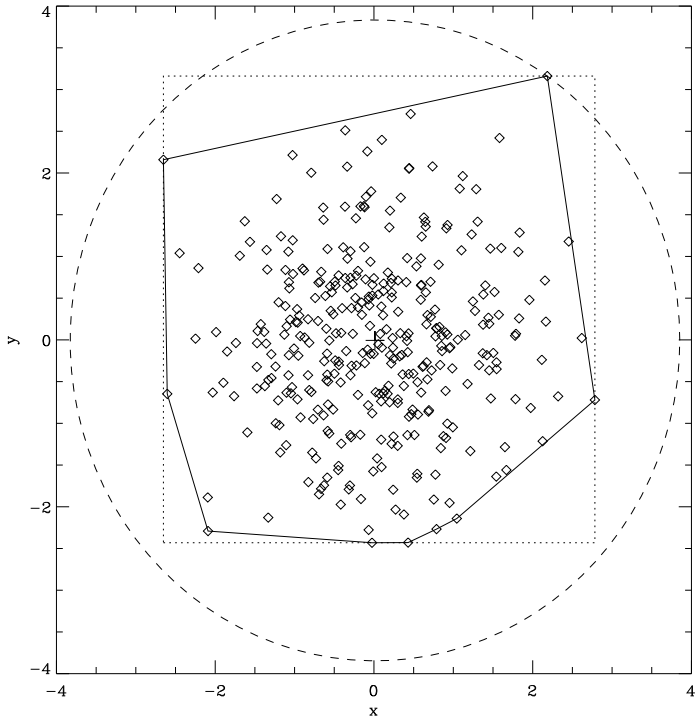

Figure A.1: Randomly distributed data points and the area they span according to different definitions (circle, rectangle, convex hull).

used to normalise both, $\bar{m}$ and $\bar{s}$.

A.2 Elongation

We notice that some of the model clusters are strongly elongated, causing a large difference in the cluster area depending on whether it is defined by the inclosing circle or by the normalised convex hull. We use this fact to propose a new statistically stable characterisation of the elongation of a cluster. We define the elongation measure ξ as the ratio

$$\xi = \frac{R_{\text{cluster}}^{\text{circle}}}{R_{\text{cluster}}^{\text{conv. hull}}} \tag{A.2}$$

This is an approach similar to the "filament index" $\mathscr{F}$ introduced by Adams & Wiseman (1994). However, while Adams & Wiseman (1994) use the actual area of a cloud obtained from column density maps, we have to estimate the area of the cluster of point sources by the convex hull. This makes ξ a reliable measure for the elongation, since it excludes the possibility that fractal substructure in an otherwise spherical cluster leads to a large ratio of the two radii. The measure ξ could also be

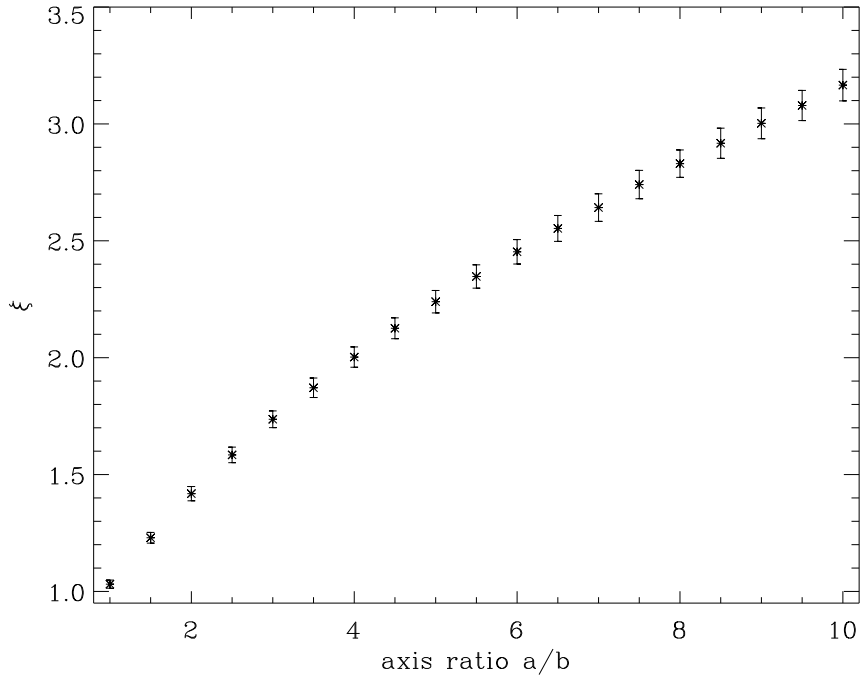

Figure A.2: The relation between the axis ratio a/b of an elliptical area and the elongation ξ, with the 1σ errors also indicated.

used to quantify the filamentary structure in molecular clouds.

In order to test if ξ is indeed a good measure for the elongation we place 350 points randomly on an elliptical area with increasing axis ratio ($1 \leq a/b \leq 10$). To minimise the statistical scatter we perform 500 different realisations for each a/b and determine the mean ξ and its standard deviation for each step. Figure A.2 shows that ξ increases with the axis ratio a/b. For $a/b = 1$ (i.e., a circle), $\xi \approx 1$, as expected.

Appendix B

Minimum Spanning Trees

Minimum spanning trees are a construct of graph theory, related to the well-known travelling salesman problem. They have been discussed e.g. by Kruskal (1956), Prim (1957), Gower & Ross (1969), or Robins et al. (2000). Astrophysical applications have been discussed mostly for the analysis of galaxy clusters, e.g. by Barrow et al. (1985), Adami & Mazure (1999), or Doroshkevich et al. (2004). Some details are given below.

B.1 Definitions

A *graph* $G = (X, E)$ is a structure consisting of a finite set of points $X = \{x_1, x_2, ...\}$ called *vertices* or *nodes* and a list of pairs of vertices $E = \{(x_i, x_j)\}$ called *edges*. A *weighted graph* has a weight or cost assigned to each edge. A graph is *connected* if there is a sequence of edges (a path) joining any point to any other point. A *tree* is a connected graph without closed loops. A tree that contains all the vertices from the original graph is called a *spanning tree*. The *minimum spanning tree* (MST), finally, is the spanning tree with the minimum total weight. The MST is unique. If some edges have exactly the same weight, the network may not be unique, as the vertices may be connected in different ways, but the total edge length and the distribution of edge lengths are always the same.

In our case, the vertices are the positions of the YSOs, and the weight of an edge is the Euclidean distance between the two points connected by that edge.

B.2 Algorithm

There are several ways to construct a MST. The two most popular algorithms both work iteratively. At any stage every edge of the MST belongs to one of two sets: Set A contains the edges assigned to the MST, set B those not assigned. *Kruskal's algorithm* (Kruskal 1956; named Algorithm I in Gower & Ross 1969) assigns iteratively to A the shortest edge in B which does not form a closed loop with any of the edges already in A. Initially A is empty, iteration stops when A contains $(n - 1)$

edges. *Prim's algorithm* (Prim 1957; named Algorithm II in Gower & Ross 1969) starts with any of the given points and assigns to A the shortest edge starting from this point. In the following steps to *A* the shortest edge from *B* is added which connects to at least one edge in *A* without forming a closed loop. Again, iteration stops when $(n-1)$ edges have been assigned to *A*. We implemented Prim's algorithm as described by Gower & Ross (1969) and Ross (1969).

B.3 Normalisation

The edge lengths of a minimum spanning tree depend on the number of points and the area, therefore the mean edge length *m* has to be normalised, in order to compare the results from samples with different numbers of objects and/or different areas. Beardwood et al. (1959) show that for the length of the shortest closed path through *n* points $l(\mathbf{P}^n)$ in *k* dimensions:

$$\lim_{n\to\infty} n^{-(k-1)/k} l(\mathbf{P}^n) = \beta_k k^{1/2} [v(\mathfrak{E})]^{1/k}, \tag{B.1}$$

where β_k is an absolute constant (independent of $\mathbf{P}$ and of $\mathfrak{E}$) and $v(\mathfrak{E})$ is the Lebesgue measure of the Lebesgue set $\mathfrak{E}$. In two-dimensional Euclidean space, this can be written as

$$l(\mathbf{P}^n) \propto \sqrt{nA}, \tag{B.2}$$

for large *n*. *A* is the area and will be defined below. Since the number of edges in a MST is $(n-1)$, Hoffman & Jain (1983) and Cartwright & Whitworth (2004) claim that the expected length of a randomly selected edge of a MST is asymptotically proportional to

$$\frac{\sqrt{nA}}{n-1}. \tag{B.3}$$

They use this factor to normalise the mean edge lengths of different data sets. Beardwood et al. (1959), however, deal with the *closed path* through *n* points (i.e., the travelling salesman problem), not a MST, as cited incorrectly by Hoffman & Jain (1983) and Cartwright & Whitworth (2004). Marcelpoil (1993), on the other hand, deduces the normalisation factor

$$\sqrt{A/n} \tag{B.4}$$

for comparing the mean edge lengths of different samples. Since

$$\lim_{n\to\infty} \frac{\sqrt{nA}/(n-1)}{\sqrt{A/n}} = \lim_{n\to\infty} \frac{n}{n-1} = 1, \tag{B.5}$$

both methods lead to the same result for large *n*; e.g. for $n > 100$ the difference is $\lesssim 1\%$ (see Fig. B.1). In this work we use the normalisation factor of Marcelpoil (1993), which seems more plausible to us. The area *A* is defined as the normalised convex hull of the data points (Equation A.1).

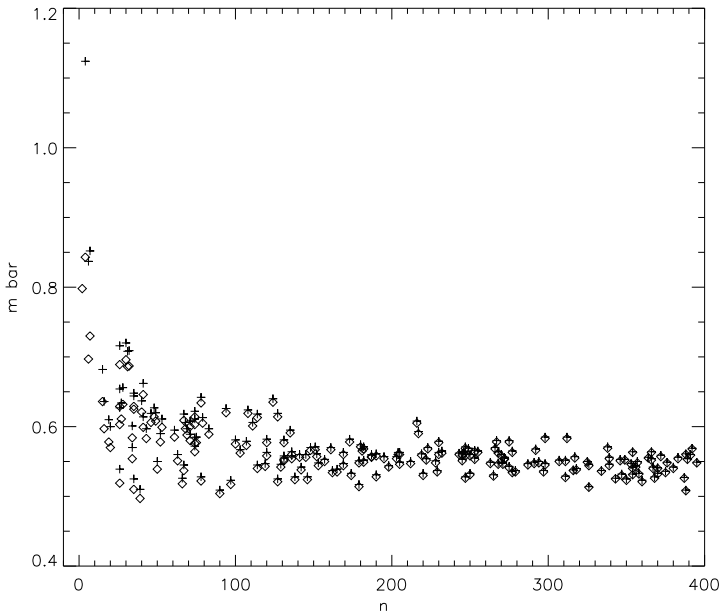

Figure B.1: Mean edge lengths $\bar{m}$ for 200 randomly created 2D sets of points ($3 \leq n \leq 400$), normalised with the factor B.4 (crosses) and B.3 (diamonds), respectively, plotted versus the number of points.

In the three-dimensional case Eq. (B.1) can be written as

$$l(\mathbf{P}^n) \propto \sqrt[3]{Vn^2}. \tag{B.6}$$

leading to the normalisation factor

$$\frac{\sqrt[3]{Vn^2}}{n-1} \tag{B.7}$$

to normalise the mean edge lengths of the 3D MST. However, we follow the reasoning of Marcelpoil (1993) and use the normalisation factor

$$\sqrt[3]{V/n} \tag{B.8}$$

in the 3D case. The volume V is defined by the normalised convex hull (Equation A.1). Again, the ratio of both normalisation factors asymptotically approaches 1, making them interchangeable for large n.

Note that we use different definitions of the radius and the area from Cartwright & Whitworth (2004) (Appendix A.1), resulting in an additional difference between our and their parameters $\bar{m}$ and $\bar{s}$. However, in the calculation of Q the radius contained in the normalisation factor is cancelled out, so the difference in the Q parameters boils down to Equation B.5. Unlike $\bar{m}$ and $\bar{s}$, the more relevant parameter Q is the same for a large number of objects, independent of the normalisation

method. To allow comparison, we list the parameters computed using the normalisation factor and the cluster radius according to Cartwright & Whitworth (2004) in Table 8.1 as well.

Appendix C

Physical Units and Constants

Many of the physical values used throughout this thesis are given in typical astrophysical units not complying with SI units. Those units and their equivalent in the SI are given below, together with the physical constants relevant for this work.

$1\ M_\odot = 1.989 \times 10^{30}$ kg	solar mass
$1\ M_\odot\ yr^{-1} = 6.3029 \times 10^{-22}$ kg s^{-1}	mass accretion rate
$1\ L_\odot = 3.85 \times 10^{26}$ W	solar luminosity
1 pc $= 3.0857 \times 10^{16}$ m	parsec
1 AU $= 1.4959787 \times 10^{11}$ m	astronomical unit
1 Å $= 10^{-10}$ m	Ångström
$G = 6.673 \times 10^{-11} m^3 kg^{-1} s^{-1}$	gravitational constant
$\mathcal{R} = 8.3145$ J K^{-1} mol^{-1}	gas constant

Bibliography

Adami, C., & Mazure, A. 1999, A&AS, 134, 393

Adams, F. C., & Fatuzzo, M. 1996, ApJ, 464, 256

Adams, F. C., & Myers, P. C. 2001, ApJ, 553, 744

Adams, F. C., & Wiseman, J. J. 1994, ApJ, 435, 693

Adams, F. C., Lada, C. J., & Shu, F. H. 1987, ApJ, 312, 788

André, P., Ward-Thompson, D., & Barsony, M. 1993, ApJ, 406, 122

André, P., Motte, F., & Bacmann, A. 1999, ApJ, 513, L57

André, P., Ward-Thompson, D., & Barsony, M. 2000, in Protostars and Planets IV, eds. V. Mannings, A. P. Boss, & S. S. Russell (Tucson: Univ. Arizona Press), 59

Bacmann, A., André, P., Puget, J.-L., et al. 2000, A&A, 361, 555

Bacmann, A., Lefloch, B., Ceccarelli, C., et al. 2002, A&A, 389, L6

Ballesteros-Paredes, J. 2004, Ap&SS, 289, 243

Ballesteros-Paredes, J., & Mac Low, M.-M. 2002, ApJ, 570, 734

Ballesteros-Paredes, J., & Hartmann, L. 2006, Rev. Mex. Astron. Astrofís., submitted (astro-ph/0605268)

Ballesteros-Paredes, J., Vázquez-Semadeni, E., & Scalo, J. 1999a, ApJ, 515, 286

Ballesteros-Paredes, J., Hartmann, L., & Vázquez-Semadeni, E. 1999b, ApJ, 527, 285

Ballesteros-Paredes, J., Klessen, R. S., & Vázquez-Semadeni, E. 2003, ApJ, 592, 188

Barber, C. B., Dobkin, D. P., & Huhdanpaa, H. T. 1996, ACM Transactions on Mathematical Software, 22, 469, `http://www.qhull.org`

Barrow, J. D., Bhavsar, S. P., & Sonoda, D. H. 1985, MNRAS, 216, 17

Basu, S. 1997, ApJ, 485, 240

Bate, M. R., & Bonnell, I. A. 2005, MNRAS, 356, 1201

Bate, M. R., & Burkert, A. 1997, MNRAS, 288, 1060

Bate, M. R., Bonnell, I. A., & Price, N. M. 1995, MNRAS, 277, 362

Bate, M. R., Clarke, C. J., & McCaughrean, M. J. 1998, MNRAS, 297, 1163

Bate, M. R., Bonnell, I. A., & Bromm, V. 2002, MNRAS, 332, L65

Bate, M. R., Bonnell, I. A., & Bromm, V. 2003, MNRAS, 339, 577

Beardwood, J., Halton, J. H., & Hammersley, J. M. 1959, Proc. Cambridge Philosophical Society, 55, 299

Behrend, R., & Maeder, A. 2001, A&A, 373, 190

Belloche, A., André, P., Despois, D., & Blinder, S. 2002, A&A, 393, 927

Benz, W. 1990, in The Numerical Modelling of Nonlinear Stellar Pulsations, ed. J. R. Buchler (Dordrecht: Kluwer), 269

Beuther, H., Schilke, P., Sridharan, T. K., et al. 2002a, A&A, 383, 892

Beuther, H., Schilke, P., Gueth, F., et al. 2002b, A&A, 387, 931

Bica, E., Dutra, C. M., & Barbuy, B. 2003, A&A, 397, 177

Blitz, L. 1993, in Protostars and Planets III, eds. E. H. Levy, & J. I. Lunine (Tucson: Univ. Arizona Press), 125

Blitz, L. 2001, Interstellar Molecular Clouds, in Encyclopedia of Astronomy and Astrophysics, `http://www.ency-astro.com` (London: Institute of Physics Publishing and Nature Publishing Group)

Blitz, L., & Williams, J. P. 1999, in The Origin of Stars and Planetary Systems, eds. C. J. Lada & N. D. Kylafis (Dordrecht: Kluwer Academic Publishers), 3

Bodenheimer, P., & Sweigart, A. 1968, ApJ, 152, 515

Bonnell, I. A., Bate, M. R., Clarke, C. J., & Pringle, J. E. 1997, MNRAS, 285, 201

Bonnell, I. A., Bate, M. R., Clarke, C. J., & Pringle, J. E. 2001a, MNRAS, 323, 785

Bonnell, I. A., Clarke, C. J., Bate, M. R., & Pringle, J. E. 2001b, MNRAS, 324, 573

Bonnell, I. A., Bate, M. R., & Vine, S. G. 2003, MNRAS, 343, 413

Bonnell, I. A., Vine, S. G., & Bate, M. R. 2004, MNRAS, 349, 735

Bonnell, I. A., Dobbs, C. L., Robitaille, T. P., & Pringle, J. E. 2006, MNRAS, 365, 37

Bontemps, S., André, P., Terebey, S., & Cabrit, S. 1996, A&A, 311, 858

Bontemps, S., André, P., Kaas, A. A., et al. 2001, A&A, 372, 173

Boogert, A. C. A., Hogerheijde, M. R., & Blake, G. A. 2002, ApJ, 568, 761

Bourke, T. L., Myers, P. C., Robinson, G., & Hyland, A. R. 2001, ApJ, 554, 916

Brown, D. W., & Chandler, C. J. 1999, MNRAS, 303, 855

Calvet, N., Muzerolle, J., Briceño, C., et al. 2004, AJ, 128, 1294

Cambrésy, L., Copet, E., Epchtein, N., et al. 1998, A&A, 338, 977

Cartwright, A., & Whitworth, A. P. 2004, MNRAS, 348, 589

Castets, A., & Langer, W. D. 1995, A&A, 294, 835

Ceccarelli, C., Castets, A., Caux, E., et al. 2000, A&A, 355, 1129

Chandler, C. J., & Richer, J. S. 2000, ApJ, 530, 851

Chen, H., Myers, P. C., Ladd, E. F., & Wood, D. O. S. 1995, ApJ, 445, 377

Clark, P. C., Bonnell, I. A., Zinnecker, H., & Bate, M. R. 2005, MNRAS, 359, 809

Clarke, C. J. 1999, MNRAS, 307, 328

Crutcher, R. M. 1999, ApJ, 520, 706

Dale, J. E., Bonnell, I. A., Clarke, C. J., & Bate, M. R. 2005, MNRAS, 358, 291

Davis, C. J., Smith, M. D., & Moriarty-Schieven, G. H. 1998, MNRAS, 299, 825

Delgado-Donate, E. J., Clarke, C. J., & Bate, M. R. 2003, MNRAS, 342, 928

Delgado-Donate, E. J., Clarke, C. J., Bate, M. R., & Hodgkin, S. T. 2004, MNRAS, 351, 617

Di Francesco, J., Myers, P. C., Wilner, D. J., Ohashi, N., & Mardones, D. 2001, ApJ, 562, 770

Dib, S., Bell, E., & Burkert, A. 2006, ApJ, 638, 797

Diehl, R., Halloin, H., Kretschmer, K., et al. 2006, Nature, 439, 45

Doroshkevich, A., Tucker, D. L., Allam, S., & Way, M. J. 2004, A&A, 418, 7

Dussert, C., Rasigni, G., Rasigni, M., Palmari, J., & Llebaria, A. 1986, Phys. Rev. B, 34, 3528

Dziourkevitch, N., Elstner, D., & Rüdiger, G. 2004, A&A, 423, L29

Elmegreen, B. G. 1993, ApJ, 419, L29

Elmegreen, B. G. 2000, ApJ, 530, 277

Elmegreen, B. G. 2002, ApJ, 577, 206

Elmegreen, B. G., & Scalo, J. 2004, ARA&A, 42, 211

Elmegreen, B. G., Efremov, Y., Pudritz, R. E., & Zinnecker, H. 2000, in Protostars and Planets IV, eds. V. Mannings, A. P. Boss, & S. S. Russell (Tucson: Univ. Arizona Press), 179

Falgarone, E., Phillips, T. G., & Walker, C. K. 1991, ApJ, 378, 186

Feigelson, E. D., & Montmerle, T. 1999, ARA&A, 37, 363

Figer, D. F. 2005, Nature, 434, 192

Foster, P. N., & Chevalier, R. A. 1993, ApJ, 416, 303

Franco, J., & Carramiñana, A., eds., 1999, Interstellar Turbulence (Cambridge: Cambridge University Press)

Froebrich, D. 2005, ApJS, 156, 169

Froebrich, D., Smith, M. D., Hodapp, K.-W., & Eislöffel, J. 2003, MNRAS, 346, 163

Froebrich, D., Scholz, A., Eislöffel, J., & Murphy, G. C. 2005, A&A, 432, 575

Froebrich, D., Schmeja, S., Smith, M. D., & Klessen, R. S. 2006, MNRAS, 368, 435

Furlan, E., Calvet, N., D'Alessio, P., et al. 2005, ApJ, 628, L65

Gawryszczak, A. J., Goodwin, S. P., Burkert, A., & Różyczka, M. 2005, in Protostars and Planets V, LPI Contribution No. 1286 (Houston: Lunar and Planetary Institute), Abstract #8102 (CD-ROM)

Gingold, R. A., & Monaghan, J. J. 1977, MNRAS, 181, 375

Gladwin, P. P., Kitsionas, S., Boffin, H. M. J., & Whitworth, A. P. 1999, MNRAS, 302, 305

Gomez, M., Hartmann, L., Kenyon, S. J., & Hewett, R. 1993, AJ, 105, 1927

Gómez de Castro, A. I. 1998, in Ultraviolet Astrophysics Beyond the IUE Final Archive, eds. W. Wamsteker and R. González Riestra, ESA SP-413, 59

Goodwin, S. P., Whitworth, A. P., & Ward-Thompson, D. 2004a, A&A, 414, 633

Goodwin, S. P., Whitworth, A. P., & Ward-Thompson, D. 2004b, A&A, 423, 169

Gower, J. C., & Ross, G. J. S. 1969, Applied Statistics, 18, 54

Gras-Velázquez, À., & Ray, T. P. 2005, A&A, 443, 541

Greene, T. P., & Lada, C. J. 2002, AJ, 124, 2185

Grosso, N., Montmerle, T., Bontemps, S., André, P., & Feigelson, E. D. 2000, A&A, 359, 113

Gutermuth, R. A., Megeath, S. T., Pipher, J. L., et al. 2005, ApJ, 632, 397

Haikala, L. K., Harju, J., Mattila, K., & Toriseva, M. 2005, A&A, 431, 149

Hartigan, P., Edwards, S., & Ghandour, L. 1995, ApJ, 452, 736

Hartmann, L. 1998, Accretion processes in star formation (Cambridge: Cambridge University Press)

Hartmann, L. 2002, ApJ, 578, 914

Hartmann, L. 2003, ApJ, 585, 398

Hartmann, L., Ballesteros-Paredes, J., & Bergin, E. A. 2001, ApJ, 562, 852

Heitsch, F., Mac Low, M.-M., & Klessen, R. S. 2001a, ApJ, 547, 280

Heitsch, F., Zweibel, E. G., Mac Low, M.-M., Li, P., & Norman, M. L. 2001b, ApJ, 561, 800

Hennebelle, P., Whitworth, A. P., Gladwin, P. P., & André, P. 2003, MNRAS, 340, 870

Henriksen, R., André, P., & Bontemps, S. 1997, A&A, 323, 549

Hillenbrand, L. A., & Hartmann, L. W. 1998, ApJ, 492, 540

Hirano, N., Kamazaki, T., Mikami, H., Ohashi, N., & Umemoto, T. 1999, in Star Formation 1999, ed. T. Nakamoto (Nobeyama: Nobeyama Radio Observatory), 181

Hirano, N., Ohashi, N., Dobashi, K., Shinnaga, H., & Hayashi, M. 2003, in Proc. of the IAU 8th Asian-Pacific Regional Meeting, Vol. II, eds. S. Ikeuchi, J. Hearnshaw, & T. Hanawa, ASP Conf. Ser., 289, 141

Hollenbach, D. J., Werner, M. W., & Salpeter, E. E. 1971, ApJ, 163, 165

Hoffman, R., & Jain, A. K. 1983, Pattern Recognition Letters, 1, 175

Hogerheijde, M. 1998, PhD thesis, Leiden University

Hubber, D. A., Goodwin, S. P., & Whitworth, A. P. 2006, A&A, 450, 881

Hunter, C. 1977, ApJ, 218, 834

Hunter, J. H., & Fleck, R. C. 1982, ApJ, 256, 505

Hurt, R. L., & Barsony, M. 1996, ApJ, 460, L45

Jappsen, A.-K., & Klessen, R. S. 2004, A&A, 423, 1

Jappsen, A.-K., Klessen, R. S., Larson, R. B., Li,Y., & Mac Low, M.-M. 2005, A&A, 435, 611

Jayawardhana, R., Hartmann, L., & Calvet, N. 2001, ApJ, 548, 310

Jeans, J. H. 1902, Phil. Trans. R. Soc. London, Ser. A, 199, 1

Johnstone, D., Wilson, C. D., Moriarty-Schieven, G. et al. 2000, ApJ, 545, 327

Johnstone, D., Di Francesco, J., & Kirk, H. 2004, ApJ, 611, L45

Kaas, A. A., & Bontemps, S. 2001, in From Darkness to Light: Origin and Evolution of Young Stellar Clusters, eds. T. Montmerle & P. André, ASP Conf. Ser. 243, 367

Kaas, A. A., Olofsson, G., Bontemps, S., et al. 2004, A&A, 421, 623

Kamegai, K., Ikeda, M., Maezawa, H., et al. 2003, ApJ, 589, 378

Kitsionas, S. 2000, PhD thesis, University of Wales

Kitsionas, S., & Whitworth, A. P. 2002, MNRAS, 330, 129

Klein, R. I., Fisher, R., & McKee, C. F. 2004, in Gravitational Collapse: From Massive Stars to Planets, eds. G. García-Segura, G. Tenorio-Tagle, J. Franco, & H. W. Yorke, Rev. Mex. Astron. Astrofís. (Ser. de Conf.), 22, 3

Klessen, R. S. 1997, MNRAS, 292, 11

Klessen, R. S. 2001a, ApJ, 550, L77

Klessen, R. S. 2001b, ApJ, 556, 837

Klessen, R. S. 2003, Rev. Mod. Astr., 16, 23

Klessen, R. S., & Burkert, A. 2000, ApJS, 128, 287

Klessen, R. S., & Burkert, A. 2001, ApJ, 549, 386

Klessen, R. S., & Kroupa, P. 2001, A&A, 372, 105

Klessen, R. S., Heitsch, F., & Mac Low, M.-M., 2000, ApJ, 535, 887

Klessen, R. S., Ballesteros-Paredes, J., Vázquez-Semadeni, E., & Durán-Rojas, C. 2005, ApJ, 620, 786

Kolmogorov, A. N. 1941, Doklady Akademii Nauk SSSR, 30, 301 (reprinted 1991, Royal Soc. London Proc. Ser. A, 434, 9)

Königl, A., & Pudritz, R. E. 2000, in Protostars and Planets IV, eds. V. Mannings, A. P. Boss, & S. S. Russell (Tucson: Univ. Arizona Press), 759

Kroupa, P. 2002, Science, 295, 82

Kruskal, J. B., Jr. 1956, Proc. Amer. Math. Soc., 7, 48

Kushnir, D., Galun, M., & Brandt, A. 2006, Pattern Recognition, in press

Lada, C. J. 1987, in Star Forming Regions, IAU Symp., 115, 1

Lada, C. J. 2001, Young Stellar Objects, in Encyclopedia of Astronomy and Astrophysics, `http://www.ency-astro.com` (London: Institute of Physics Publishing and Nature Publishing Group)

Lada, C. J., & Lada, E. A. 2003, ARA&A, 41, 57

Lada, C. J., & Wilking, B. A. 1984, ApJ, 287, 610

Langer, W. D., van Dishoeck, E. F., Bergin, E. A., et al. 2000, in Protostars and Planets IV, eds. V. Mannings, A. P. Boss, & S. S. Russell (Tucson: Univ. Arizona Press), 29

Larson, R. B. 1969, MNRAS, 145, 271

Larson, R. B. 1981, MNRAS, 194, 809

Larson, R. B. 1985, MNRAS, 214, 379

Larson, R. B. 1995, MNRAS, 272, 213

Larson, R. B. 1999, in Star Formation 1999, ed. T. Nakamoto (Nobeyama: Nobeyama Radio Observatory), 336

Larson, R. B. 2003, Rep. Prog. Phys., 66, 1651

Larson, R. B. 2005, MNRAS, 359, 211

Laughlin, G., & Różyczka, M. 1996, ApJ, 456, 279

Lee, C. W., & Myers, P. C. 1999, ApJS, 123, 233

Li, Z.-Y., & Nakamura, F. 2004, ApJ, 609, L83

Li, Y., Klessen, R. S., & Mac Low, M.-M. 2003, ApJ, 592, 975

Li, Y., Mac Low, M.-M., & Klessen, R. S. 2005, ApJ, 626, 823

Looney, L. W., Mundy, L. G., & Welch, W. J. 2003, ApJ, 592, 255

Lubow, S. H., & Pringle, J. E. 1993, MNRAS, 263, 701

Lucy, L. B. 1977, AJ, 82, 1013

Luhman, K. L., Stauffer, J. R., Muench, A. A., et al. 2003, ApJ, 593, 1093

Mac Low, M.-M. 1999, ApJ, 524, 169

Mac Low, M.-M. 2000, in Star Formation from the Small to the Large Scale, ESLAB symposium 33, eds. F. Favata, A. Kaas, & A. Wilson, ESA SP-445, 457

Mac Low, M.-M., & Klessen, R. S. 2004, Rev. Mod. Phys., 76, 125

Mac Low, M.-M., & Ossenkopf, V. 2000, A&A, 353, 339

Mac Low, M.-M., Klessen, R. S., Burkert, A., & Smith, M. D. 1998, Phys. Rev. Lett., 80, 2754

Mac Low, M.-M., de Avillez, M. A., & Korpi, M. J. 2004, in How Does the Galaxy Work?, eds. E. J. Alfaro, E. Pérez, & J. Franco, ASSL Vol. 315, 339

Marcelpoil, R. 1993, Analytical Cellular Pathology, 5, 177

Maret, S., Ceccarelli, C., Caux, E., Tielens, A. G. G. M., & Castets, A. 2002, A&A, 395, 573

Massey, P., & Meyer, M. R. 2001, Stellar Masses, in Encyclopedia of Astronomy and Astrophysics, `http://www.ency-astro.com` (London: Institute of Physics Publishing and Nature Publishing Group)

Masunaga, H., & Inutsuka, S. 2000, ApJ, 531, 350

McLaughlin, D. E., & Pudritz, R. E. 1997, ApJ, 476, 750

Megeath, S. T., Allen, L. E., Gutermuth, R. A., et al. 2004, ApJS, 154, 367

Megeath, S. T., Flaherty, K. M., Hora, J., et al. 2005, in Massive Star Birth: A Crossroads of Astrophysics, IAU Symp. 227, 383

Men'shchikov, A. B., & Henning, T. 1997, A&A, 318, 879

Mestel, L., & Spitzer, L., Jr. 1956, MNRAS, 116, 503

Meyer, M. R., Adams, F. C., Hillenbrand, L. A., Carpenter, J. M., & Larson, R. B. 2000, in Protostars and Planets IV, eds. V. Mannings, A. P. Boss, & S. S. Russell (Tucson: Univ. Arizona Press), 121

Mizuno, A., Onishi, T., Yonekura, Y., et al. 1995, ApJ, 445, L161

Mizuno, A., Hayakawa, T., Tachihara, K., et al. 1999, PASJ, 51, 859

Monaghan, J. J. 1985, Comp. Phys. Rep., 3, 71

Monaghan, J. J. 1992, ARA&A, 30, 543

Monaghan, J. J. 2001, J. Korean Astron. Soc., 34, 203

Morino, J.-I., Yamashita, T., Hasegawa, T., & Nakano, T. 1998, Nature, 393, 340

Motoyama, K., & Yoshida, T. 2003, MNRAS, 344, 461

Motte, F., & André, P. 2001, A&A, 365, 440

Motte, F., & André, P., & Neri, R. 1998, A&A, 336, 150

Muench, A. A., Lada, E. A., Lada, C. J., et al. 2003, AJ, 125, 2029

Muzerolle, J., Hillenbrand, L., Calvet, N., Briceño, C., & Hartmann, L. 2003, ApJ, 592, 266

Muzerolle, J., Megeath, S. T., Gutermuth, R. A., et al. 2004, ApJS, 154, 379

Myers, P. C., & Ladd, E. F. 1993, ApJ, 413, L47

Myers, P. C., Adams, F. C., Chen, H., & Schaff, E. 1998, ApJ, 492, 703

Myers, P. C., Evans, N. J., II, & Ohashi, N. 2000, in Protostars and Planets IV, eds. V. Mannings, A. P. Boss, & S. S. Russell (Tucson: Univ. Arizona Press), 217

Nakano, T. 1998, ApJ, 494, 587

Narayanan, G., Walker, C. K., & Buckley, H. D. 1998, ApJ, 496, 292

Neuhäuser, R., & Sterzik, M. 1997, Comm. Konkoly Obs., 100, 369

Ogino, S., Tomisaka, K., & Nakamura, F. 1999, PASJ, 51, 637

Olmi, L., & Testi, L. 2002, A&A, 392, 1053

Onishi, T., Mizuno, A., Kawamura, A., Ogawa, H., & Fukui, Y. 1996, ApJ, 465, 815

Ossenkopf, V., & Mac Low, M.-M. 2002, A&A, 390, 307

Padman, R., Bence, S., & Richer, J. 1997, in IAU Symp. 182: Herbig-Haro Flows and the Birth of Stars, eds. B. Reipurth, & C. Bertout (Dordrecht: Kluwer Academic Publishers), 123

Padoan, P. 1995, MNRAS, 277, 377

Padoan, P., & Nordlund, Å. 1999, ApJ, 526, 279

Padoan, P., & Nordlund, Å. 2002, ApJ, 576, 870

Palla, F., & Stahler, S. W. 2000, ApJ, 540, 255

Papaloizou, J. C. B., & Lin, D .N. C. 1995, ARA&A, 33, 505

Paul, J. 2001, in High Energy Gamma-Ray Astronomy, eds. F. A. Aharonian & H. J. Völk, American Institute of Physics Proc., 558, 183

Penston, M. V. 1969, MNRAS, 144, 425

Persi, P., Marenzi, A. R., Gómez, M., & Olofsson, G. 2001, A&A, 376, 907

Piontek, R. A., & Ostriker, E. C. 2004, ApJ, 601, 905

Piontek, R. A., & Ostriker, E. C. 2005, ApJ, 629, 849

Preibisch, T. 2003, A&A, 410, 951

Preibisch, T., & Zinnecker, H. 2002, AJ, 123, 1613

Preibisch, T., & Zinnecker, H. 2004, A&A, 422, 1001

Price, D. J. 2004, PhD thesis, University of Cambridge

Prim, R. C. 1957, Bell Systems Tech. J., 36, 1389

Pringle, J.E. 1981, ARA&A, 19, 137

Pudritz, R. E. 2002, Science, 295, 68

Quillen, A. C., Thorndike, S. L., Cunningham, A., et al. 2005, ApJ, 632, 941

Reach, W. T., Rho, J., Young, E., et al. 2004, ApJS, 154, 385

Reid, M. A., Pudritz, R. E., & Wadsley, J. 2002, ApJ, 570, 231

Reipurth, B., & Bally, J. 2001, ARA&A, 39, 403

Ridge, N. A., Wilson, T. L., Megeath, S. T., Allen, L. E., & Myers, P. C. 2003, AJ, 126, 286

Ripley, B. D., & Rasson, J.-P. 1977, J. Appl. Prob., 14, 483

Robins, V., Meiss, J. D., & Bradley, E. 2000, Physica D, 139, 276

Ross, G. J. S. 1969, Applied Statistics, 18, 103

Russell, H. N., Dugan, R. S., & Stewart, J. W. 1927, Astronomy: A revision of Young's Manual of Astronomy: II: Astrophysics and Stellar Astronomy (Boston: Ginn and Co.)

Salpeter, E. E. 1955, ApJ, 121, 161

Saraceno, P., André, P., Ceccarelli, C., Griffin, M., & Molinari, S. 1996, A&A, 309, 827

Sasao, T. 1973, PASJ, 25, 1

Scalo, J. 1990, in Physical Processes in Fragmentation and Star Formation, eds. R. Capuzzo-Dolcetta, C. Chiosi, & A. di Fazio, ASSL Vol. 162, 151

Scalo, J., & Elmegreen, B. G. 2004, ARA&A, 42, 275

Schmeja, S., & Klessen, R. S. 2004, A&A, 419, 405

Schmeja, S., & Klessen, R. S. 2006, A&A, 449, 151

Schmeja, S., Klessen, R. S., & Froebrich, D. 2005, A&A, 437, 911

Shirley, Y. L., Evans, N. J., II, Rawlings, J. M. C., & Gregersen, E. M. 2000, ApJS, 131, 249

Shu, F. H. 1977, ApJ, 214, 488

Shu, F. H. 1992, The Physics of Astrophysics, Volume II: Gas Dynamics (Sausalito: University Science Books)

Shu, F. H., Adams, F. C., & Lizano, S. 1987, ARA&A, 25, 23

Shu, F. H., Li, Z.-Y., & Allen, A. 2004, ApJ, 601, 930

Sigalotti, L. di G., de Felice, F., & Sira, E. 2002, A&A, 395, 321

Singh, S., Ma, C.-P., & Arons, J. 2004, Phys. Rev. D, 69, 3003

Smith, M. D. 1998, Ap&SS, 261, 169

Smith, M. D. 2000, Irish Astron. J., 27, 25

Smith, M. D. 2002, in The Origins of Stars and Planets: the VLT view, ESO Astrophysics Symposia, eds. J. Alves & M. McCaughrean, CD-ROM

Smith, M. D. 2004, The Origin of Stars (London: Imperial College Press)

Stahler, S. W., & Palla, F. 2004, The Formation of Stars (Weinheim: Wiley-VCH)

Stanke, T. 2000, PhD thesis, Universität Potsdam

Stanke, T., Smith, M. D., Gredel, R., & Khanzadyan, T. 2006, A&A, 447, 609

Stone, J. M., Ostriker, E. C., & Gammie, C. F. 1998, ApJ, 508, L99

Strong, A. W., Bignami, G. F., Caraveo, P. A., et al. 1982, A&A, 115, 404

Stutzki, J., Bensch, F., Heithausen, A., Ossenkopf, V., & Zielinsky, M. 1998, A&A, 336, 697

Tassis, K., & Mouschovias, T. C. 2004, ApJ, 616, 283

Taylor, S. D., Morata, O., & Williams, D. A. 1996, A&A, 313, 269

Testi, L., & Sargent, A. I. 1998, ApJ, 508, L91

Tomisaka, K. 1996, PASJ, 48, L97

Umemoto, T., Saito, M., Yang, J., & Hirano, N. 1999, in Star Formation 1999, ed. T. Nakamoto (Nobeyama: Nobeyama Radio Observatory), 227

van Dishoeck, E. F. 2004, ARA&A, 42, 119

van Dishoeck, E. F., & Blake, G. A. 1998, ARA&A, 36, 317

Vázquez-Semadeni, E., Ostriker, E. C., Passot, T., Gammie, C., & Stone, J. 2000, in Protostars and Planets IV, eds. V. Mannings, A. P. Boss, & S. S. Russell (Tucson: Univ. Arizona Press), 3

Vázquez-Semadeni, E., Ballesteros-Paredes, J., & Klessen, R. S. 2003, ApJ, 585, L131

Vázquez-Semadeni, E., Kim, J., Shadmehri, M., & Ballesteros-Paredes, J. 2005, ApJ, 618, 344

Visser, A. E., Richer, J. S., & Chandler, C. J. 2002, AJ, 124, 2756

Vogt, H. 1926, Astron. Nachr., 226, 301

Wada, K., Meurer, G., & Norman, C. A. 2002, ApJ, 577, 197

Walker, C. K., Lada, C. J., Young, E. T., Maloney, P. R., & Wilking, B. A. 1986, ApJ, 309, L47

Walter, F. M. 1986, ApJ, 306, 573

White, R. J., & Hillenbrand, L. A. 2004, ApJ, 616, 998

Whitworth, A. P., & Ward-Thompson, D. 2001, ApJ, 547, 317

Whitworth, A. P., Bhattal, A. S., Francis, N., & Watkins, S. J. 1996, MNRAS, 283, 1061

Williams, J. P. 1999, in Interstellar Turbulence, eds. J. Franco & A. Carramiñana (Cambridge: Cambridge University Press), 190

Williams, J. P., De Geus, E. J., & Blitz, L. 1994, ApJ, 428, 693

Williams, J. P., Blitz, L., & McKee, C. F. 2000, in Protostars and Planets IV, eds. V. Mannings, A. P. Boss, & S. S. Russell (Tucson: Univ. Arizona Press), 97

Wolf-Chase, G., Moriarty-Schieven, G., Fich, M., & Barsony, M. 2003, MNRAS, 344, 809

Wuchterl, G., & Klessen, R. S. 2001, ApJ, 560, L185

Wuchterl, G., & Tscharnuter, W. M. 2003, A&A, 398, 1081

Yokogawa, S., Kitamura, Y., Momose, M., & Kawabe, R. 2003, in Proc. of the IAU 8th Asian-Pacific Regional Meeting, Vol. II, eds. S. Ikeuchi, J. Hearnshaw, & T. Hanawa, ASP Conf. Ser., 289, 239

Young, C. H., & Evans, N. J. 2005, ApJ, 627, 293

Young, C. H., Shirley, Y. L., Evans, N. J., II, & Rawlings, J. M. C. 2003, ApJS, 145, 111

Young, C. H., Jørgensen, J. K., Shirley, Y. L., et al. 2004, ApJS, 154, 396

Yu, K. C., Billawala, Y., Smith, M. D., Bally, J., & Butner, H. M. 2000, AJ, 120, 1974

Additional References

Textbooks

Barlow, R. J. 1989, Statistics: A Guide to the Use of Statistical Methods in the Physical Sciences (Chichester: John Wiley & Sons)

Karttunen, H., Kröger, P., Oja, H., Poutanen, M., & Donner, K. J., eds., 2003, Fundamental Astronomy (Berlin: Springer), 4th ed.

Voigt, H. H. 1991, Abriss der Astronomie (Mannheim: BI Wissenschaftsverlag)

Data bases and websites

Smithsonian/NASA Astrophysics Data System Abstract Service
`http://adsabs.harvard.edu`

arXiv.org e-Print archive
`http://arxiv.org`

Protostars Database at the Dublin Institute for Advanced Studies
`http://www.dias.ie/protostars/`

SIMBAD Astronomical Database
`http://simbad.u-strasbg.fr`

MathWorld – A Wolfram Web Resource
`http://mathworld.wolfram.com`

Eric Weisstein's World of Physics
`http://scienceworld.wolfram.com/physics/`

LEO English-German dictionary
`http://dict.leo.org`

Merriam-Webster Online
`http://www.m-w.com/`

Publications Related to this Work

Refereed Publications

D. Froebrich, **S. Schmeja**, M. D. Smith, & R. S. Klessen: *Evolution of Class 0 protostars: Models vs. observations.* MNRAS, 368, 435 (2006)

S. Schmeja, & R. S. Klessen: *Evolving structures of star-forming clusters.* A&A, 449, 151 (2006)

S. Schmeja, R. S. Klessen, & D. Froebrich: *Number ratios of young stellar objects in embedded clusters.* A&A, 437, 911-918 (2005)

S. Schmeja, & R. S. Klessen: *Protostellar mass accretion rates from gravoturbulent fragmentation.* A&A, 419, 405-417 (2004)

Conference Proceedings and Abstracts

D. Froebrich, **S. Schmeja**, M. D. Smith, & R. S. Klessen: *Comparing Properties of Class 0 Protostars with Model Predictions.* In Protostars and Planets V, Abstract #8039, Lunar and Planetary Institute, Houston (CD-ROM) (2005)

S. Schmeja, & R. S. Klessen: *Analysing the Structures of Young Star Clusters.* In Protostars and Planets V, Abstract #8397, Lunar and Planetary Institute, Houston (CD-ROM) (2005)

S. Schmeja, & R. S. Klessen: *Mass Accretion of Protostars: A Highly Dynamical Process.* In Protostars and Planets V, Abstract #8402, Lunar and Planetary Institute, Houston (CD-ROM) (2005)

S. Schmeja, R. S. Klessen, D. Froebrich, & M. D. Smith: *Star Formation from Gravoturbulent Fragmentation: Mass Accretion and Evolution of Protostars.* In "Low-mass stars and brown dwarfs: IMF, accretion and activity", eds. L. Testi & A. Natta, Mem. Soc. Astron. Ital., 76, 193-198 (2005)

S. Schmeja, R. S. Klessen, D. Froebrich, & M. D. Smith: *Star Formation in Turbulent Molecular Clouds: Mass Accretion and Evolution of Protostars.* Astron. Nachr. 325, Suppl. Issue 1 (Short Contributions AG/CAS 2004 Prague), 26-27 (2004)

S. Schmeja, & R. S. Klessen: *Time-varying protostellar mass accretion rates.* In Proceedings of the JENAM 2003 Minisymposium "Early Phases of Star Formation", Baltic Astronomy 13, 381-385 (2004)

List of Acronyms

CTTS	classical T Tauri star
FIR	far infrared
GMC	giant molecular cloud
IMF	initial mass function
IR	infrared
ISM	interstellar medium
ISO	Infrared Space Observatory
KS	Kolmogorov-Smirnov (test)
MC	molecular cloud
MHD	magnetohydrodynamics
MIR	mid infrared
MSDC	mean surface density of companions
MST	minimum spanning tree
NIR	near infrared
PMS	pre-main sequence
SED	spectral energy distribution
SFE	star formation efficiency
SFR	star formation rate
SI	Système International d'Unités
SIS	singular isothermal sphere
SPH	smoothed particle hydrodynamics
UV	ultraviolet
WTTS	weak-line T Tauri star
XMM	X-ray Multi-Mirror
YSO	young stellar object

Acknowledgements/Danksagung

- First of all, I would like to thank my advisor Ralf Klessen. From him I learnt many things about star formation and hydrodynamics, he almost always had time for questions and discussions, and he provided the numerical simulations on which this work is based on.

- I always enjoyed being with the AIP people, especially the members of the star formation group and the other "inhabitants" of the Schwarzschildhaus. In particular I wish to thank Nicolas (for discussions on Brown Dwarves, IDL and Hertha BSC), Katharina (for coffee & cookies and giving me so many rides from the AIP to the University), Spyros (for coffee & cookies and in particular for proof-reading this thesis), and Andreas (for his LaTeX-help). Ein herzlicher Dank geht auch an die EDV-Abteilung, insbesondere Mario Dionies, für zuverlässige Abhilfe bei Computerproblemen, sowie an die Bibliothekarin, Regina von Berlepsch, für das rasche Beschaffen von Artikeln auch aus "exotischen" Zeitschriften.

- I wish to thank my collaborators Dirk Froebrich (Dublin Institute for Advanced Studies), Michael Smith (Armagh Observatory, now at the University of Kent), and Dan Kushnir (Weizmann Institute of Science). I am particularly grateful to Dirk and the staff at DIAS for their warm hospitality during my stay in Dublin.

- My position was funded by the Emmy Noether Programme of the *Deutsche Forschungsgemeinschaft* (grant no. KL1358/1). I acknowledge additional financial support for visits and to attend conferences from the *Astronomische Gesellschaft*, the organisers of the JENAM 2003 meeting in Budapest, the Dublin Institute for Advanced Studies, and the Insitute for Pure and Applied Mathematics, University of California at Los Angeles.

- Ich danke den Potsdamer Schmejas, die mir nicht nur in meinen ersten Wochen in Potsdam ein Dach über dem Kopf gegeben haben, sondern auch maßgeblich dafür verantwortlich sind, dass ich mich in Potsdam bzw. Babelsberg in kürzester Zeit heimisch gefühlt habe. Zu letzterem beigetragen haben u.a. auch Roland und Anja, die Besucher des Doktorandenstammtisches und die Drachenbootpaddler des Treibgut-Teams.

- Ein weiteres Dankeschön gilt meinen Eltern, die mich immer unterstützt haben. Besonders dankbar bin ich, dass mir auch in Potsdam viele Freunde aus Innsbruck und dem Rest der Welt nahe geblieben sind.
- Last not least: Danke Steffi. *Turn around, every now and then I get a little bit terrified but then I see the look in your eyes* ...